Toward an electron electric dipole moment measurement using Ytterbium Fluoride

Dhiren Manji Kara

Thesis submitted in partial fulfilment of the requirements for the degree of Doctor of Philosophy of the University of London and the Diploma of Membership of Imperial College.

Department of Physics

Imperial College London

University of London

September 2010

Declaration

I declare that this thesis is my own work. Where I have used the work of others the sources are appropriately referenced and acknowledged.

Abstract

This thesis reports the progress made on an experiment aiming to test if the electron has a permanent electric dipole moment (EDM). YbF is used in this experiment because the interaction between the EDM of its valence electron and an applied electric field is much greater than that of a free electron or one that is in an atom. By precisely detecting shifts in the molecular energy levels when electric and magnetic fields are applied the EDM can be inferred. These shifts are measured by carrying out interferometry on a beam of supersonically cooled YbF. We have acquired a null dataset that has a factor of two better precision than the most sensitive eEDM measurement made. The result, $6.1 \pm 4.7 \times 10^{-28}\, e$.cm (68% CI) and $6.4 \pm 9.1 \times 10^{-28}\, e$.cm (95% CI), is consistent with zero, demonstrating that we are insensitive to a large class of systematic effects. Along with other diagnostic experiments and systematic error investigations, we have shown that the experimental setup is now capable of making a world - beating measurement of the electron EDM.

Acknowledgements

First and foremost I thank Ed Hinds, Ben Sauer, Jony Hudson and Mike Tarbutt for making my PhD a very fulfilling experience. I thank my supervisors Ben and Jony for their support, encouragement, advice and for instigating the Friday group visits to the pub. I have learnt an incredible amount from them and for that I owe them a great deal. It is because of them that I have genuinely enjoyed working on the EDM experiment. I also thank some other EDMers past and present: Henry, for teaching me how to run the EDM machine, Suresh, for all those discussions of how to get locks to do what you want them to do, and Joe S, for taking over the reins in the lab as quickly as he did so that I could head off to write my thesis.

Malcolm Boshier, from the Los Alamos National Laboratory, visited the group on a couple of occasions. Without him the frequency doubling laser system would never have come into being. He has taught me many things about optics, the importance of careful planning and the value of triple checking things and then checking again.

Thanks to the rest of CCM and Ion Trapping, in particular Thom, Sean T, Jake, Sarah, Dan C and Sean D. I must thank Ed Hinds, especially, for bringing together such a great, friendly and interesting group of people. I would like to thank the Bay 3 gang for putting up with me when I demanded that they talk quietly and tiptoe around because I feared that my laser would unlock. It was fun sharing the lab with them, except when Sarah was in charge of music.

Thanks to Jon Dyne for all those target skims at short notice, technical advice and teaching me how to use the weird and wonderful tools in his workshop. I wish to thank Sanja Maricic for all her administrative support.

A big thank you to my parents and family for everything that they have done for me and for always supporting my decisions. Thanks to my friends for taking an interest in what I do and to Angelie for all her encouragement and understanding, especially whilst writing my thesis.

Contents

List of Figures

List of Tables

Chapter 1

Introduction

This thesis describes an experiment that aims to measure the electron's electric dipole moment (eEDM) to an unprecedented level by using the polar molecule, YbF.

The motivations for such an experiment are discussed in this chapter, along with an explanation of what an eEDM is and how it relates to time - reversal symmetry. This is followed by a brief historical overview of EDM experiments. The benefits of using polar molecules, such as YbF, in EDM experiments are then given. Finally, the interferometric technique implemented in this experiment to measure an energy shift due to an eEDM interaction is outlined.

Chapter 2 contains a description of the experimental apparatus. Our data acquisition and analysis methods are discussed in chapter 3. This chapter also describes the techniques we have developed and implemented to search for possible systematic effects (processes which can produce fake eEDMs). These effects are analysed and quantified in chapter 4. Chapter 5 has some concluding remarks and suggestions for improving the measurement of the eEDM.

1.1 Physics beyond the standard model

The standard model (SM) predicts the electron to have an electric dipole moment (eEDM) of $< 10^{-38}\, e$.cm. This is much too small to be detected with the sensitivity offered by current experimental techniques. However, more accessible values of $10^{-26} - 10^{-29}\, e$.cm [1] are anticipated by extensions to the model as shown in fig. 1.1. The contrast between these values means eEDM experiments provide a very clean way of searching for physics beyond the SM.[1] The most sensitive measurement of the eEDM, made in 2002, [4] is consistent with zero and indicates

[1] Large differences in EDM predictions are also seen for other particle such as neutrons and protons.

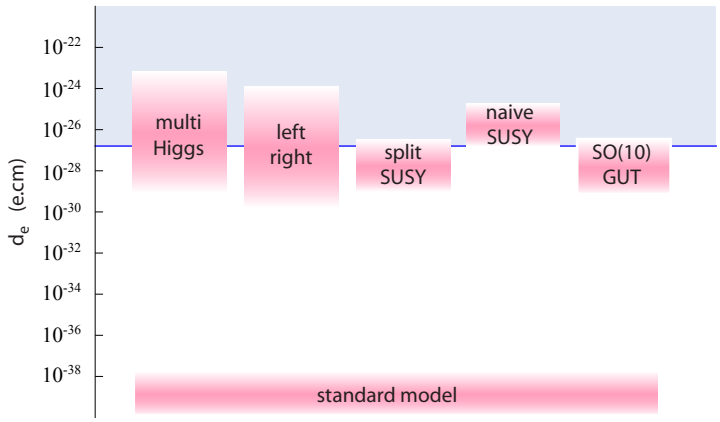

Figure 1.1: *Size of eEDMs predicted by various particle theories [2, 3]. The blue-grey shaded region contains values forbidden by the current experimental limit.*

$d_e < 1.6 \times 10^{-27}\, e.\text{cm}$.[2] Looking at fig 1.1 this is particularly interesting, since a relatively small improvement on the measurement would help further constrain or even refute new particle theories, while registering a non-zero value would indicate a failure of the SM.

There are numerous reasons why physicists are pursuing theories beyond the SM [5]. It has no reference to gravity, it does not explain the relative strengths of the other fundamental forces, or allow enough CP symmetry breaking needed to account for the abundance of matter over antimatter in the universe. Our experiment promises to provide information about the latter problem, because the existence of a finite eEDM violates T (see sec. 1.3), which via the widely accepted CPT theorem is equivalent to CP violation. The importance of this violation in explaining the matter dominated universe is discussed in the next section.

1.2 Baryogenesis

There is strong evidence that the visible universe contains much more matter than antimatter. For example, the cosmic rays we see at earth consist mainly of matter and we do not detect the radiation that would be expected from annihilation at boundaries between islands of matter and antimatter. Most of the matter we see is made up of baryons (particles such as neutrons and protons, made up of three quarks), leptons specifically neutrinos are in comparison difficult to detect. Therefore, the excess of matter is often referred to as a *baryon asymmetry*. This could be a direct result of asymmetric initial conditions. However, this concept does not sit well with the big bang theory, which predicts that there were equal amounts of

[2] d_e represents the size of the eEDM in units of e, the electron charge, times a distance in cm.

matter and antimatter in the very early universe. A preferred explanation is that the imbalance developed from an initially symmetric universe through some baryon producing process, generally termed *baryogenesis*.

In 1967 Sakharov identified three essential requirements for baryogenesis [6]: 1) baryon number (B_N) changing events, where B_N is +1/-1 for a baryon/antibaryon, 2) C and CP violation, and 3) for the baryon number changing events to have frozen out at a time when the universe was not in thermal equilibrium. It will be explained next how these could have resulted in an excess of matter.

Baryon number changing

Baryon number changing is the simplest of Sakharov's conditions to understand since without this there could not have been a deviation from the symmetric initial conditions where $B_N = 0$. Particle theories predict that B_N changing reactions would have taken place at the extremely high temperature of the early universe.

Let us assume a hypothetical baryon producing process occurred at temperatures greater than a critical "freeze - out" temperature T_B, where a massive boson, X , spontaneously decayed into a pair of light baryons, P and Q:

$$X_{(R,L)} \rightarrow P + Q \tag{1.1}$$

where the subscript R or L denotes the boson's handedness[3]. The importance of identifying the handedness will become apparent later. This reaction would have also occurred for the corresponding antiparticles,

$$\overline{X}_{(R,L)} \rightarrow \overline{P} + \overline{Q} \tag{1.2}$$

where the masses M_X, M_P and M_Q are equal to $M_{\overline{X}}$, $M_{\overline{P}}$ and $M_{\overline{Q}}$ respectively.

If after the big bang, X and $\overline{X}$ were present in equal quantities and the two decays proceeded with identical rates then the total baryon number would have always remained close to zero. To generate a baryon asymmetry the matter and antimatter decays would have had to differ in rate. This would have required C and CP violation.

[3] A photon whose motion points in the same direction as its spin is defined to be right - randed, R, conversely a photon with antiparallel alignment is defined to be left - handed, L.

C and CP violation

Before discussing C and CP violations the symmetry operators are summarised: the parity transformation (P) acts to reflect all the spatial co-ordinates of a system such that $(x, y, z) \rightarrow (-x, -y, -z)$, charge conjugation (C) changes matter to antimatter, and time reversal (T) changes the sign of the time co-ordinate so $t \rightarrow -t$. The effect of these operators is illustrated in fig. 1.2.

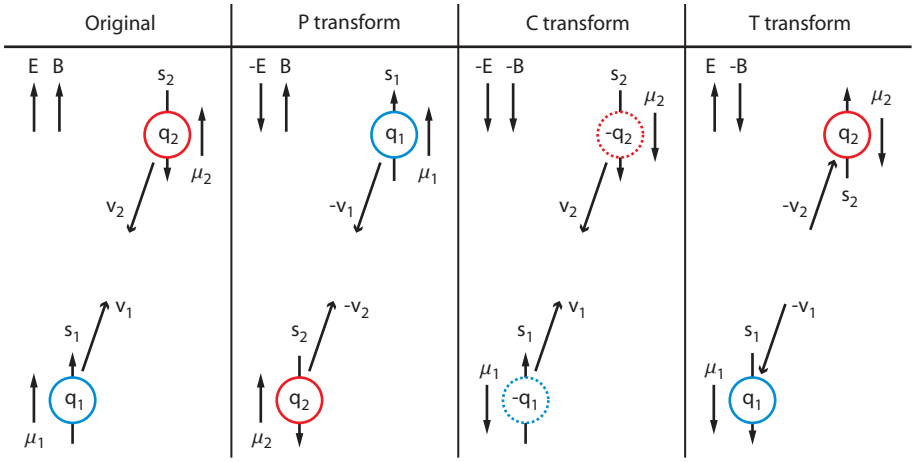

Figure 1.2: *P, C and T transforms applied to two particles which each have a charge q, spin s, magnetic moment μ and velocity v. The effect on applied E and B fields is also illustrated. If the probability of a process occurring changes after a given transform then it violates that symmetry.*

Since the C operator acts to change matter to antimatter it may seem at first that C violation alone should be enough to permit a particle to have a different decay rate from its antiparticle. However, this is not the case as will be demonstrated next.

It was generally thought that the laws of nature were symmetric, but in 1950 it was argued that this should not be taken as a matter of fact [7] and that the validity of the idea needed to depend on experiment [8]. Indeed, Wu et al [9] almost immediately provided evidence of P violation in the weak force mediated beta-decay of ^{60}Co into a ^{60}Ni atom, electron and antineutrino. Their experiment measured the rates, labelled as Γ_{Co} and $\Gamma_{\mathrm{P(Co)}}$ below, of two possible decay paths of opposing parity. The decays were identified by comparing the direction of the emitted electron's velocity, u_e, and the ^{60}Co's nuclear spin $\vec{I}$.

$$\Gamma_{\mathrm{Co}} \left[{}^{60}\mathrm{Co}(\vec{I} = \uparrow) \rightarrow e^{-}(u_e = \downarrow) + {}^{60}\mathrm{Ni} + \overline{\nu}_{e(R)} \right]$$

$$\Gamma_{\mathrm{P(Co)}} \left[{}^{60}\mathrm{Co}(\vec{I} = \uparrow) \rightarrow e^{-}(u_e = \uparrow) + {}^{60}\mathrm{Ni} + \overline{\nu}_{e(L)} \right].$$

They found that the decay violates parity since u_e preferentially points in the direc-

tion opposite to $\vec{I}$, i.e., that $\Gamma_{\mathrm{Co}} \gg \Gamma_{\mathrm{P(Co)}}$. This symmetry breaking measurement was supported by another in 1957 [10], which showed P violation in meson decays.[4] It was soon hypothesised that the weak force also violated C in such a way that CP symmetry is conserved overall. So, if we were to make the (rather unrealistic) decay rate measurement of $\overline{\mathrm{Co}}$ we would find $\Gamma_{\mathrm{Co}} = \Gamma_{\mathrm{P}(\overline{\mathrm{Co}})}$ and $\Gamma_{\mathrm{P(Co)}} = \Gamma_{\overline{\mathrm{Co}}}$ and consequently,

$$\Gamma_{\mathrm{Co}} + \Gamma_{\mathrm{P(Co)}} = \Gamma_{\overline{\mathrm{Co}}} + \Gamma_{\mathrm{P}(\overline{\mathrm{Co}})}. \tag{1.3}$$

Taking CP as a conserved symmetry, as in eq. 1.3, the decay rates of ^{60}Co and $^{60}\overline{\mathrm{Co}}$ are exactly the same even though they violate C.[5] This shows that C violation alone is not enough to get the baryon number changing matter and antimatter reactions given in eqs. 1.1 and 1.2 to proceed at different rates — CP violation is also required

Assuming that X and $\overline{X}$ were the by-product of some C violating, but CP symmetric effect, it is possible that only $X_{(R)}$ and $\overline{X}_{(L)}$ particles were created over their opposite handed partners.[6] In turn, if the decay of these then violated CP the lifetime of $X_{(R)}$ could be much shorter than that of $\overline{X}_{(L)}$, and baryons would be produced at a faster rate than antibaryons. To end up with a dominance of matter, however, this effect needed to be accompanied by a fast cooling of the universe to the threshold or freeze-out temperature, T_{B}, as discussed next.

Thermal equilibrium

In the following discussion I will use the previously defined situation, where because of C violation the early universe contained an abundance of $X_{(R)}$ and $\overline{X}_{(L)}$ particles, and because of CP violation the decay rate of $X_{(R)}$ was greater than that of $\overline{X}_{(L)}$.

Under thermal equilibrium the forward rate of a reaction equals that of the reverse rate. In this steady-state the relative populations of the reacting particles are exclusively determined by the Boltzmann distribution, which at high temperature favours populating the more energetic states and at reduced temperature the less energetic ones. Since the decays of $X_{(R)}$ and $\overline{X}_{(L)}$ are exothermic[7], the population ratios of $X_{(R)}$ and $\overline{X}_{(L)}$ to P, Q and $\overline{P}$, $\overline{Q}$ would have been larger (smaller) at higher (lower) temperatures. Therefore, as the hot early universe cooled towards T_{B} the

[4] The work was published in the same Physical Review issue as [9].

[5] In fact the hypothesis that the weak force conserves CP has been proven wrong by experiment see sec. 1.3.

[6] I could just as well have taken a universe where C asymmetry worked out to give a dominance of $X_{(L)}$ and $\overline{X}_{(R)}$ particles.

[7] The decay was earlier defined to be spontaneous, i.e., $M_X > M_P + M_Q$, and hence exothermic.

number of $X_{(R)}$ and $\overline{X}_{(L)}$ particles would have decreased whilst the number of P, Q, $\overline{P}$ and $\overline{Q}$ increased.

If the cooling was sufficiently slow the reactions would have maintained thermal equilibrium at all times and the number of baryons would always have remained equal to number of antibaryons, because $M_P = M_{\overline{P}}$ and $M_Q = M_{\overline{Q}}$. However, if the cooling was more rapid T_B would have been reached in a faster time. During this time $X_{(R)}$ would have been able to respond, due to its short lifetime, by decaying into P and Q. In contrast $X_{(R)}$ would not have had enough time to produce an appreciable amount of $\overline{P}$ and $\overline{Q}$ before the B_N changing decays were frozen - out and a baryon dominated universe would have been left.

Sakharov's three conditions are all physically possible. However, it is the elusiveness of CP violation in both experiment and particle theory that is the major stumbling block for models of baryogenesis. This is why, searches for the violation are very important.

1.3 T and CP violation in the electron's EDM

In 1964 J. H. Christensen et al [11] found that neutral kaons are CP asymmetric when recording the decay of K^0_S and its CP counterpart K^0_L. The violation was seen in another process more recently when differences between decays of B^0 and $\overline{B}^0$ mesons were detected at the Stanford Linear Accelerator Center [12]. Unfortunately for theories of baryogenesis, these are the only CP breaking effects that have been seen so far. However, extensions to the SM predict the possibility of the symmetry being broken in the form of finite EDMs of particles, such as electrons, neutrons and protons. As mentioned earlier an EDM violates T, but breaks CP via the CPT theorem.

The usual definition of a dipole is that of two charges, $+q$ and $-q$, separated by a vector, $\vec{r}$, producing a moment, $\vec{d} = q\ \vec{r}$, where $\vec{r}$ originates at the negative charge. For a single particle a more general description is used: that the dipole originates from a displacement between the particle's centre of charge and its centre of mass [13],

$$\vec{d} = \int_v \rho(\vec{r})\ \vec{r}\ \delta r^3 \tag{1.4}$$

where $\rho(\vec{r})$ is the charge density in units of electron charge $|e|$ per unit volume in cm^3 at position $\vec{r}$ from the centre of mass of the particle, δr^3 is a differential volume element and $\vec{d}$ has units e.cm. A positive EDM, d, is defined to point in the same direction as the particle spin, $\vec{s}$, so $\vec{d} = d\,\frac{\vec{s}}{|\vec{s}|}$.

The required structure implied by eq. 1.4 arises from CP violating interactions between the particle and the vacuum field. Because extensions to the SM allow the existence of exotic virtual particles in the vacuum field they naturally predict relatively large EDMs.

An electron EDM in combination with spin can, in principle, provide up to four distinct states for the electron: $|\uparrow_{\vec{s}}, \uparrow_{\vec{d}_e}\rangle$, $|\uparrow, \downarrow\rangle$, $|\downarrow, \downarrow\rangle$, and $|\downarrow, \uparrow\rangle$, where in accordance with the Wigner - Eckhart theorem $\vec{d}_e$ must lie along the same axis as $\vec{s}$. However, the periodic table shows that the electron has only two internal states or, in other words, a single spin - $\frac{1}{2}$ degree of freedom. This means that if an eEDM does exist, only one of the two possible arrangements of the eEDM and spin have been allowed by nature — either parallel or antiparallel. Assuming also rotational invariance, it is this constraint, not the existence of a non - zero eEDM alone, that breaks T (and CP) symmetry. To illustrate this let us apply a T transform to an electron as shown in fig. 1.3.

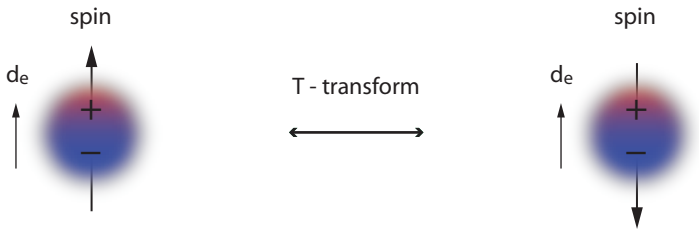

Figure 1.3: *Under a T reversal the spin flips and the eEDM is left unchanged.*

The figure shows that an electron with an eEDM pointing in the same direction as its spin is a T reversal[8] of one with an eEDM pointing in the direction opposite to its spin. If both were seen just as often as each other then T symmetry would be maintained. However, we know nature must allow just one of the orientations shown in fig. 1.3 to preside and therefore, observing a non-zero eEDM would provide direct evidence of T violation. A similar argument, but using a P operator on an electron, shows that an eEDM is also P violating.

Investigating T violation is not only important for improving our understanding of particle physics and baryogenesis, but also for addressing the more philosophical issue of the direction of time flow. Events during and after the big bang left a relatively ordered universe in thermodynamic non - equilibrium; time flow can be associated with it gradually becoming more disordered as it approaches thermal equilibrium. For example, in the case of a burning match it is the increasing entropy of the system as the match burns that provides us with an arrow of time.

[8] Reversal is used interchangeably with transform.

Consequently, it is obvious if a movie of such a process is being played forwards or backwards. However, under conditions of thermal equilibrium entropy is maximised and remains constant. *Does this mean the direction of time flow is obscured or even irrelevant for a system in thermal equilibrium?* Not if an entropy independent T violating process, such as a spinning particle with an EDM, exists.

Now that the motivations for searching for T violation have been covered some EDM experiments are described.

1.4 EDM experiments

The general principle behind an EDM experiment is to measure the energy shift induced by the application of an electric field[9],

$$\Delta U = -\vec{d} \cdot \vec{E}. \tag{1.5}$$

where ΔU is the energy shift due to the EDM interaction, $\vec{d}$ is the EDM of the system and $\vec{E}$ is the applied electric field. These are high precision experiments since the expected shifts are extremely small. For example if the electron EDM, d_e sits just below the current world limit at $1.6 \times 10^{-27}\, e$.cm and a reasonably large field of 100 kV/cm is applied, the shift in terms of frequency will be about 40 nHz. This is the same as the Zeeman shift of the electron caused by a stray magnetic field of only a few aT. Luckily for experimentalists, there are particular atoms and molecules where the EDM interaction is amplified so that the magnetic field *only* needs to be controlled to the fT level. Nevertheless, the major challenge of EDM experiments lies in the need to apply large electric fields while maintaining a high degree of control over the magnetic field. The three most successful experiments carried out to measure the EDM of a neutron, proton and electron all find EDMs consistent with zero, but impose tight constraints on extensions to the SM. These are summarised in the following sections.

Trapped ultracold neutron experiment

Early neutron EDM experiments in the 1950s were the first to probe for symmetry violation, see E. M. Purcell and N. F. Ramsey's experiment [15]. The fast moving neutron beams they used resulted in relatively small interaction times of fractions of a second. As experimental techniques and technologies have progressed these have increased to the extent where modern neutron experiments, using trapped ultracold

[9] It should be noted that new storage ring experiments are using the E - fields experienced in the rest frame of a relativistic particle under the application of a B - field to look for EDMs [14].

neutrons (UCNs), have interaction times of up to a few minutes. The current experimental limit, published in 2006 by C. A. Baker et al [16], of the neutron EDM at a 90% confidence level is $d_n < 2.9 \times 10^{-26}\, e$.cm. The experiment measured a precession of the neutron spin due to applied uniform E and magnetic, B, fields, which were non - zero only along a direction defined to be the z - axis. The precession occured at the Larmor frequency v_L given by:

$$\begin{aligned} hv_{L+} &= 2\mu_n B + 2d_n E \\ hv_{L-} &= 2\mu_n B - 2d_n E \end{aligned} \tag{1.6}$$

where μ_n is the neutron magnetic moment, and v_{L+} and v_{L-} correspond to parallel or antiparallel application of the E and B fields. A finite d_n would raise the degeneracy between v_{L+} and v_{L-}. The role of the applied B field was threefold: to define a quantization axis, centre v_L around a suitably sized frequency and provide a handle on any background magnetic fields. It should also be noted that in eq. 1.6 the factors of two arise because v_L has been defined as the difference between the precession rates of spin up and down neutrons.

To measure v_L the UCNs were spin polarised using a thin magnetised sheet of foil and then entered a magnetically shielded cylindrical trap with their spin aligned along the applied B ($1\,\mu$T) and E ($4.5\,$kV/cm) fields. Once the neutrons were inside, a pulse ($\sim$2 s in length) of oscillating magnetic field tuned close to v_L was applied rotating the spin into the xy - plane. The neutron spin was then allowed to precess around the B and E - fields for $\sim 120-150\,$s before the oscillating field was applied again. The method of applying two relatively short oscillating field pulses separated by a finite period of time to measure relative energies is known as the Ramsey separated - oscillatory - field resonance technique [17]. The number of neutrons returning to their original spin state would depend on how close the oscillating frequency was to v_L. Next the neutrons were released from the trap and sent through the magnetised foil for the second time; only neutrons in their original state successfully passed through. These neutrons were then counted. For half of the counting period the neutrons were exposed to an oscillating field just before they passed through the foil such that it flipped their spin orientation. This allowed the counting of neutrons in the opposing spin state for diagnostic purposes. If a detectable EDM did exist then any changes in the counts would be correlated to the relative orientation of the E and B - fields. However, effects masquerading as EDMs had to be considered. A few, which are common to nearly all EDM experiments, are outlined here:

- Stray magnetic fields which switch direction with the reversal of the E. An

example is a magnetic field arising from leakage currents between the electric field plates.

- Motional magnetic fields, where the motion of a particle with velocity $\vec{v}$ in a field $\vec{E}$ generates a magnetic field proportional to the cross product $\vec{E} \wedge \vec{v}$.
- Geometric or Berry phase, which is related to field inhomogeneities.

Since these systematics depend on the velocities and paths of individual particles, they are not trivial to model or control making them a fairly substantial topic of discussion in the literature, e.g. [18]. The effects mentioned here will be examined more rigorously in the context of our YbF eEDM measurement in chapter 4.

In recognition of the problems caused by stray magnetic fields mercury (Hg) atoms were also released into the trap in the neutron experiment to be used as a comagnetometer. Since, Hg is known to have a much smaller EDM than a neutron (see sec. 1.4.1) it was relatively insensitive to any EDM interactions. This method was preferred over the use of a fluxgate magnetometer for example, because it could sample the same region as the neutrons.

1.4.1 Atomic EDMs

To measure the proton and electron EDM an electrically neutral body such as an atom is usually used, because the applied E-field would accelerate a charged particle. However, being in an atom the interaction between the particle EDM and E is modified.

Schiff's theorem [19] states that an atom — if considered to be made up of non-relativistic, point-like particles — cannot be used to measure EDMs. The argument is that the nucleus and electrons rearrange themselves under an applied field in such a way that the constituents are shielded from external fields and hence, no EDM interactions are possible. Another way of looking at this is that since the atom or its constituents are not accelerated by the applied field the average field they see must be zero. But, as was acknowledged by Schiff himself the theorem overlooks many things: i) the finite size of the nucleus — relevant to nucleon EDMs, ii) the presence of relativistic effects — important for electron EDM measurements[10], and iii) particle spin contributions to the forces [20]. Once these are taken into account the atom can have a non-vanishing EDM interaction. In fact, if the atom has a large enough Z (the finite size and relativistic effects become more pronounced as Z increases) the EDMs of its constituents are enhanced, rather than suppressed.

Diamagnetic atoms are more suited to nucleon EDM measurements, whilst paramagnetic atoms, having an unpaired electron, are usually used for electron EDM

[10] This will be discussed in more detail in sec. 1.5.

searches [21]. The current limit on the proton EDM d_p was calculated from measurements made on a Mercury isotope EDM d(^{199}Hg). The limit on d_e was found using Tl atoms. These experiments are described next.

Mercury Experiment

The mercury isotope ^{199}Hg is a good candidate to search for nucleon EDMs, partly owing to the fact that it has a nuclear spin $I = 1/2$ but no overall electron spin. This isotope has been investigated since the 1980s at the University of Washington, Seattle. The current limit $d(^{199}\text{Hg}) < 3.1 \times 10^{-29}\, e.\text{cm}$ (95% confidence level) was published in March 2009 by W. C. Griffith et al. [22].

The Hg experiment was unique compared to others within the field, in that it solely used laser light to manipulate and probe the system of interest. The experiment consisted of two neighbouring glass cells containing a Hg vapour. Along the z - axis the same B - field was applied to both cells, with E applied so that it pointed in the opposite direction for each cell. Perpendicular to this axis a beam of laser light at a wavelength of 253.7 nm (the $6^1S_0 \rightarrow 6^3P_1$ transition) was shone through each cell. Two additional Hg cells outside of the E - field were used to cancel B - field noise.

During the pump period of the experiment, which lasted 30 s, the light had a relatively large intensity of 6 mW and was circularly polarised. Upon absorption of the light the atoms gained an angular momentum pointing in the beam direction, aligning the spins of the Hg nuclei. These spins would now begin to precess around the applied B - field. To ensure that all the atoms had the same phase, the amplitude of the laser light was chopped at the precession frequency.[11] The beam intensities were then attenuated to a few μW and the polarisation switched to linear for the probe part of the experiment which lasted around 100 s. A detuning of 20 GHz was also introduced; this meant that the electric field components of the linearly polarised light experienced different refractive indices, which rotated the polarisation of the probe beams as they travelled through the respective cells. The angles of rotation modulated at the precession frequency of the nuclei. The difference in the measured frequency for each cell was the atomic EDM,

$$h(v_1 - v_2) = 4d(^{199}Hg) \cdot E \tag{1.7}$$

where v_1 and v_2 are the precession frequencies measured in the cells with parallel and antiparallel E and B - fields respectively.

[11] This ensured the spins had a pure linear polarisation in a frame rotating at the precession frequency.

From the limit on the ^{199}Hg EDM found in the Romalis experiment an upper limit for the proton EDM $d_p < 7.9 \times 10^{-25}\, e$.cm was derived using Schiff Moment calculations made by V. F. Dmitriev and R. A. Senkov [23]. The experiment also provides a limit of $5.8 \times 10^{-26}\, e$.cm for d_n, which is in agreement with the neutron upper limit measured by C. A. Baker.

This experiment was susceptible to systematics similar to the neutron experiment and the methods used to study them are found in [24]. Suggested improvements are to use liquid Xenon to carry out the measurement since it can withstand higher electric fields [25].

Tl

The thallium isotope ^{205}Tl, which is paramagnetic, was used in the measurement of the electron EDM d_e by B. C. Regan et al [4] at the University of California, Berkeley. Their final upper limit published in February 2002 after 15 years of development was $d_e < 1.6 \times 10^{-27} e$.cm (90% confidence). Tl was adopted because it has, what is known as, an electron EDM enhancement factor, R, that is very large due to its high Z nucleus, where

$$R = \frac{d_{Tl}}{d_e} \tag{1.8}$$

and d_{Tl} is the atomic EDM to be measured. For the case of Tl the enhancement is calculated to be $R = -585$ accurate to $5-10\,\%$ [26]. Therefore, an energy shift caused by the eEDM in a Tl atom is 585 times as big as one for a free electron. It should be noted the uncertainty on the enhancement factor is accounted for as a systematic error on the final measurement and is typically negligible in comparison to other sources of error.

A continuous beam of Tl was used in the experiment. The velocity of the beam was a few hundreds of m/s. Therefore, a potentially large source of systematic error was the motional magnetic field proportional to $E \wedge v$. To avoid the problem, two pairs of counter propagating beams, two travelling up and two down, were implemented. One pair of counter propagating beams would have sufficed to cancel motional magnetic fields, but another pair allowed measurements with B and E parallel and antiparallel to be taken simultaneously. This gave the experimenters an advantage when hunting down systemic errors and provided common mode magnetic noise rejection. In addition, the beams contained Na atoms which were used as a comagnetometer.

Taking one direction of propagation, each Tl beam passed through laser light tuned to 378 nm, the $6P_{1/2}$ $(F = 1) \rightarrow 7S_{1/2}$ $(F = 1)$ transition, in the presence

of an applied B. Due to selection rules the valence electrons were pumped into the $6P_{1/2}$ ($F = 1,\ m_F = 0$) state. The atoms then travelled through a region of oscillating magnetic field on resonance with the Zeeman splitting between the $F = 1,\ m_F = 0, \pm 1$ levels. This field prepared the atoms in a superposition of the $m_F = \pm 1$ states. Next each of the two beams passed in-between a pair of 1m long high voltage (HV) plates; depending on the beam in question the atoms experienced either parallel or antiparallel E and B - fields. As the atoms traversed this region the $m_F = +1$ and -1 states picked up phase at rates of ω_{+1} and ω_{-1} respectively where,

$$\begin{aligned} \omega_{+1} &= \mu_{Tl}B \pm d_{Tl}E \\ \omega_{-1} &= -(\mu_{Tl}B \pm d_{Tl}E), \end{aligned} \tag{1.9}$$

where the $\pm$ represents parallel $(+)$ or antiparallel $(-)$ application of the E and B - fields. Upon exiting the plates a second oscillating magnetic field was applied to recombine the electron population back into the $m_F = 0$ state. Due to interference between transitions from the $m_F = +1$ and -1 states the efficiency of the process directly related to the phase difference, $\Delta\phi$, acquired,

$$\Delta\phi = (\omega_{+1} - \omega_{-1})\tau, \tag{1.10}$$

where τ was the length of time the atoms spent in the applied E and B region. A second pair of laser beams at 378 nm were then used to probe the population remaining in the $m_F = \pm 1$ states in each atomic beam. Discrepancies between florescence signals for E and B parallel and antiparallel were an indication of an EDM. The YbF experiment uses a very similar interferometric technique to the one that has been described here (see sec. 1.6).

The development of this state - of - the - art eEDM experiment can be found in [27, 28]. Ultimately, the experiment was limited by motional magnetic field systematic effects and the size of the enhancement factor. It is felt that to make advancements systems other than atoms should be used, and polar molecules appear to be a promising route, because they are less sensitive to motional magnetic fields (see [29] and sec. 4.2.5) and can have much larger enhancements. The first molecular EDM experiment, which measured d_p, was carried out on the diamagnetic TlF molecule by D. Cho and E. A. Hinds et al. in 1991 [30]. However, we will now focus on paramagnetic polar molecules, which are suited to eEDM measurements.

1.5 Polar molecules

It was previously mentioned that in the case of the eEDM it is relativistic effects that allow the shielding in Schiff's theorem to be overcome and that for atoms with a large Z, like Tl, the eEDM is in fact enhanced. Based on [31] and [32] I will explain this concept in the context of an atom and then show why for a polar molecule the amplification of d_e can be even bigger. Formulas and expressions will not be dealt with in detail, these can be found in the literature, for example, [31, 33].

Let us look at an alkali atom in applied B_{app} and E_{app} fields pointing along the z-axis, so that the valence electron spin $\vec{s}$ (and $\vec{d_e}$) have a well defined direction and the electron has a polarised probability distribution (described by state ψ_e) as shown in fig. 1.4. Because the electron does not accelerate when E_{app} is turned on, we can say

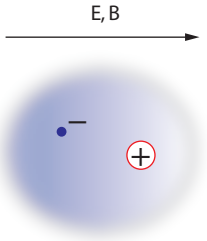

Figure 1.4: *Under an applied electric field the atomic electron cloud becomes polarised.*

that there is no net electrostatic force acting on it. Hence, the Coulomb field from the nucleus and core electrons, ϵ_c, combined with E_{app} must be zero on average, i.e., $\langle\psi_e|\,\epsilon_c + E_{\text{app}}\,|\psi_e\rangle = 0$. This fact holds in *both* the non-relativistic and relativistic cases.[12] So how can we beat Schiff's theorem? Well, in the non-relativistic limit we can not, since d_e is a constant and $U_{\text{edm}} = \langle\psi_e| - d_e(\epsilon_c + E_{\text{app}})\,|\psi_e\rangle = -d_e\,\langle\psi_e|\,\epsilon_c + E_{\text{app}}\,|\psi_e\rangle = 0$. However, in the relativistic case the eEDM in the lab frame, d_e^{lab} will be different to that in the electron's rest frame, d_e, as follows:

$$\begin{aligned} d_e^{lab}(\vec{r}) &= \frac{d_e}{\gamma(\vec{r})} \\ &= d_e\sqrt{1-\tfrac{v_z(\vec{r})^2}{c^2}} \end{aligned} \tag{1.11}$$

where $\vec{r}$ is the electron position with respect to the nucleus (assumed to be at rest in the lab), γ is the Lorentzian factor and v_z is the z-component of the electron

[12] The relativistic E-field given by $\frac{\vec{v}\wedge\vec{B}}{c^2}$ experienced by the electron is negligible.

velocity in the lab frame.[13] The interaction then becomes,

$$U_{\text{edm}} = \langle\psi_e| - d_e\sqrt{1 - \frac{v_z(\vec{r})^2}{c^2}}(\epsilon_c + E_{\text{app}})\,|\psi_e\rangle \tag{1.12}$$

where because the speed of the electron is not a constant U_{edm} does not necessarily vanish even though $\langle\psi_e|\,\epsilon_c + E_{\text{app}}\,|\psi_e\rangle$ does.

The greater the asymmetry (or polarisation) of the electron distribution the larger U_{edm} becomes. E_{app} induces this asymmetry by mixing the parity of ψ_e. For example, a ψ_e that begins as a pure s orbital state (even parity) gets mixed in with a bit of the p orbital (odd parity) when E_{app} is applied.[14] For an atom the mixing goes linearly with E_{app} so that the eEDM interaction takes the simple form:

$$U_{\text{edm}} = -d_e \cdot R \cdot E_{\text{app}} \tag{1.13}$$

where the enhancement constant, R, which was mentioned earlier in the context of the Tl eEDM experiment, depends on ϵ_c, the size of the relativistic effect in eq 1.11 and the polarisability of the electron cloud. For an electron in the ground s or p state $R \sim 10Z^3\alpha$ [31] and therefore, an atom with a heavy nucleus is suited to an eEDM measurement. One problem with atoms is that even in fields of $\sim$100 kV/cm they are only very weakly polarised.

However, if a highly electronegative atom (one that strongly attracts electrons) is bonded to the high Z atom to form a polar molecule, the electron's distribution becomes almost fully polarised — an equal mixture of s and p orbital states — even in the absence of an applied E-field. Effectively, it is as if a very large field of $\sim$ 10 GV/cm, typically not realisable in the lab, has been applied to the heavy nucleus. This is the key reason why polar molecules can provide much bigger enhancements than atoms. Nonetheless, for a molecular eEDM measurement an E_{app} is still needed to align the polarisation, which points along the direction of the internuclear axis $\hat{n}$, with d_e, which lies along the total angular moment vector of the molecule $\vec{F}$. The applied field's ability to align $\hat{n}$ and $\vec{F}$ is given by what is referred to as a polarisation factor defined as:

[13] Eq. 1.11 simply describes the impact of Lorentz contraction on the eEDM. An electric dipole moment is just a charge multiplied by a length.

[14] Take two state functions, of different parity, $\cos(x)$ and $\sin(x)$. Independently, they have symmetric (unpolarised) probability distributions about $x = 0$, $\cos(x)^2$ and $\sin(x)^2$. However, the mixed state does not; $(\cos(x) + \sin(x))^2$ is asymmetric about $x = 0$.

$$\eta(E_{\text{app}}) = \frac{\left\langle \hat{n} \cdot \vec{F} \right\rangle}{|\hat{n}| \left|\vec{F}\right|} \tag{1.14}$$

where $0 < \eta < 1$ and saturates to a value of 1 as E_{app} is increased. The relationship between the factor and E_{app} depends on the spacing of different rotational states of the molecule, where for closer spacing $\eta \to 1$ at a smaller E_{app}. Much in the same way that the mixing of different parity orbital states results in a polarisation of the electron cloud, it is the mixing of rotational states that corresponds to an alignment of the internuclear axis with the molecule's angular momentum.

It is then convenient to write the eEDM interaction for a molecule as,

$$\Delta U \quad = \quad -\eta \, d_e \, E_{\mathit{eff}} \tag{1.15}$$

where E_{eff} is a constant often referred to as the effective field. It depends on the Z of the heavy nucleus, the extent to which the electronegative atom polarises the molecule and the state the electron is in. In fig. 1.5 $\eta \cdot E_{\mathit{eff}}$ is plotted versus E_{app} for YbF, which has an E_{eff} of $-25\,\text{GV/cm}$ with a 10 % uncertainty [34]. The fact that E_{eff} is negative means that it points in the opposite direction to the applied field. When choosing a molecule for an EDM experiment not only is the size of E_{eff}

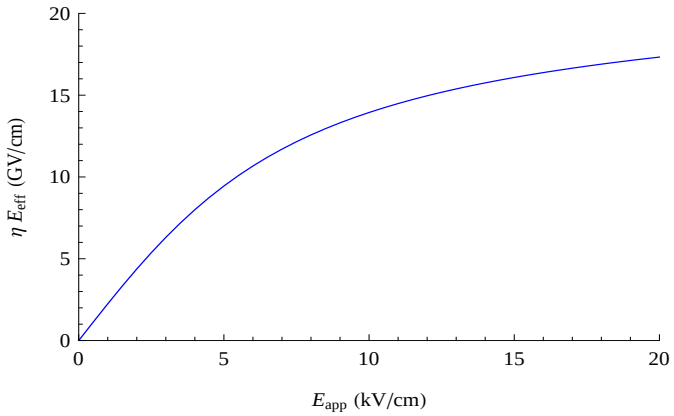

Figure 1.5: *The size of the electric field effectively seen by the electron in YbF when an external field E_{app} is applied. YbF has an E_{eff} of $-25\,GV/cm$ (with a 10 % uncertainty not shown above). Fields of up to $10\,kV/cm$ are straightforward to apply in the lab. When YbF is in its groundstate, which is used in this experiment, it has an electric dipole moment of $\mu_e = 3.91 \pm 0.04$) Debye [37].*

considered, but also the ease of saturating η, the lifetime of the state of interest, the practicality of using the molecule in a lab (it may be radioactive, extremely corrosive

or poisonous) and which laser frequencies would be required for state preparation and probing.

D. DeMille is using lead oxide (PbO) in an eEDM experiment being carried out at Yale University. Though it has a modest E_{eff}, $\eta \to 1$ in a field of only a few V/cm. The advantage is that the problems associated with applying and reversing large electric fields are reduced. Another benefit is that PbO contains two metastable states with opposite parity — in particular, states where the Zeeman shifts due to B fields are in the same direction, but eEDM shifts are in opposite directions — allowing certain systemic effects to be cancelled out [35, 36]. However, the fact that these are metastable states means the interaction times with the applied E are limited.[15] Currently, work is being done on the preparation and detection methods that will be implemented [38].

Preliminary work has also started on two other experiments using polar molecules. At Michigan University, a beam of Tungsten carbide (WC), which is easily polarisable and has a large E_{eff}, has recently been produced [39]. A collaboration between the groups of J. M. Doyle, G. Gabrielse and D. DeMille have been investigating the $H\,^3\Delta_1$ metastable state in Thorium monoxide (ThO). They have measured a lower bound on its lifetime of around 2 ms [40]. This gives them a practical limit on the interaction times that will be possible.

Though polar molecules are very promising systems for detecting eEDMs a world beating measurement has yet to be made with one. This is because, relative to atoms, they pose many additional experimental and technical challenges. They are difficult to produce in large numbers, are often highly reactive and due to their many internal degrees of freedom have complex energy level systems[16], which hinders state preparation and detection. Many of these issues were already addressed on the YbF experiment before I started working on it. The early part of my PhD was spent developing the apparatus such that the experiment could run in a fully automated fashion with minimal interruptions. This has resulted in an improved sensitivity per $\sqrt{\text{day}}$ — since a much larger fraction of the day is actually spent acquiring data.

By making the experiment more sensitive and easier to run we were then able to design and implement many diagnostic tools in an efficient and methodical manner. The upshot is that we have been able to understand, control and quantify systematic effects important to our YbF experiment. This is key if we want to make a robust eEDM measurement.

The next section provides a brief description of the YbF molecule and an overview

[15] Only states belonging to rotationally excited levels can have this particular type of opposite parity where the dependence on an eEDM is reversed [35, 36].

[16] It should be remembered that such molecules are often exotic and their spectra previously unexplored.

of the interferometric technique we employ in our experiment. Some of the terminology particular to this experiment is also introduced.

1.6 Fundamentals of the experiment

The YbF molecule can be thought of as a Yb^{2+} core and an F^- ion with an unpaired (valence) electron. This structure makes YbF's ground rotational, vibrational and electronic state[17], labelled X $^2\Sigma^+$ ($\nu = 0, \mathrm{N} = 0$)[18], similar to that of an alkali atom. Coupling between the electron spin and the $I = \frac{1}{2}$ spin of the F nucleus (we use the spinless ^{174}Yb isotope) results in a groundstate with two hyperfine levels, $F = 0$ (singlet) and $F = 1$ (triplet), that are separated by around 170 MHz. These are the levels on which we carry out our measurement. The $F = 1$ level contains three sublevels denoted $|F = 1, m_F = 0\rangle$, $|1, +1\rangle$, $|1, -1\rangle$ where the energy splitting, ΔU_{EDM}, between $|1, +1\rangle$ and $|1, -1\rangle$ is sensitive to the eEDM as follows:

$$\Delta U_{EDM} = -2\,\eta\,d_e\,E_{eff}. \tag{1.16}$$

A cold source of YbF molecules is used, because at room temperature the groundstate is sparsely populated. The supersonic expansion technique is implemented to cool our YbF to ∼4 K, sec. 2.3 contains more details. The source runs at a repetition rate of 25 Hz and produces collimated packets of molecules moving vertically upwards with heavily populated $F = 0$ and 1 levels. Each packet has a mean velocity of about 590 m/s, with a spread of 40 m/s and completes its journey through the apparatus before the next one is created. We will follow the progress of one molecular packet or what we often refer to as a *shot*.

The molecular packet first encounters a 552 nm (green) laser beam on resonance with the Q(0) ($F = 1$) transition shown in fig. 1.6, which drives electrons from the $F = 1$ state to the first excited electronic state, $A^2\Pi_{\frac{1}{2}}(\nu = 0, \mathrm{N} = 0)$. Electrons in this state then decay, either into $F = 0$ where they will remain, or $F = 1$ where they will be driven back to the $A^2\Pi_{\frac{1}{2}}$ state and decay again. A certain fraction ($\sim$ 60%) also decay into X $^2\Sigma^+$ ($\nu = 0, \mathrm{N} = 2$), which is a dark state, and no longer play a role in the experiment. Since the laser has the effect of pumping molecules into the $|0, 0\rangle$ state, this is called the *pump* phase of the experiment. To remove all the $F = 1$ population the laser beam must be intense enough to saturate the transition.

[17] In addition to the electronic levels found in an atom, a molecule has vibrational and rotational levels. In YbF the rotational spacing is the smallest and electronic the biggest.

[18] The reader does not have to be familiar with this type of spectroscopic notation to understand how the experiment works.

Here, saturate means that in the time taken for the molecules to traverse the laser beam all the electrons will have been pumped into either the $F = 0$ level or the dark state.

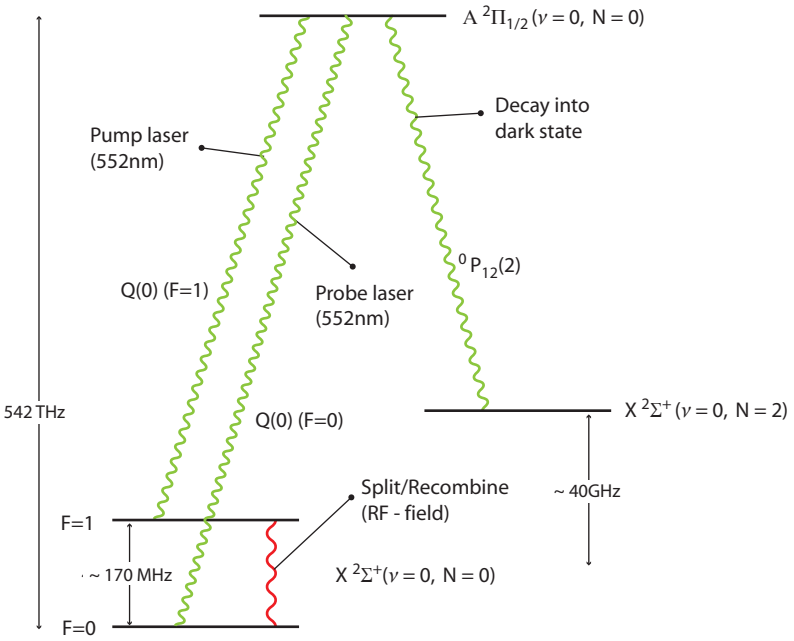

Figure 1.6: *The YbF energy levels important to this experiment. Of the molecules originally in the $F = 1$ state around 60 % are lost to the dark state after pumping.*

The YbF then approaches the interaction region, which has applied electric and magnetic fields, E_z and B_z. E_z (∼10 kV/cm) is supplied by two parallel, high voltage plates separated by 12 mm, and B_z (∼10 nT) with a pair of current carrying loops, which we often refer to as the magnetic field coils. Both of the fields are only intended to be non - zero in a direction defined as the z - axis (see fig. 1.8).[19]

When the molecular packet has entered the plates a radiofrequency (rf) pulse, with its magnetic field component polarised along the x - axis, is applied. The length (15 – 20 μs) and amplitude of the pulse are chosen such that what is known as a π-pulse [17] is administered. This ideally results in a full population transfer of electrons from $|0, 0\rangle$ into a coherent superposition of the $|1, \pm 1\rangle$ sublevel states as follows:

$$|0, 0\rangle \rightarrow \frac{-i}{\sqrt{2}}(|1, +1\rangle + |1, -1\rangle) \tag{1.17}$$

where the reader should not worry about the $-i$, it just represents an overall phase

[19] The z-axis is perpendicular to the motion of the molecular beam, defined to move in the positive y-direction.

for the superposition state. This transition is referred to as the *split* phase of the experiment. A frequency of a few MHz greater than the field - free hyperfine splitting of 170.25MHz is required because E_z causes a Stark shift of the $|1, \pm 1\rangle$ states. Details of how the pulse is applied and controlled are given in sec. 2.6 along with a theoretical description of the transition.

As the YbF beam travels through the plates the phases of the $|1, +1\rangle$ and $|1, -1\rangle$ states evolve at different rates ω_+ and ω_- respectively,

$$\begin{aligned} \omega_+ &= \tfrac{1}{\hbar}(g_F \mu_B \, B_z \, - \, \eta \, d_e \, E_{eff}) \\ \omega_- &= -\tfrac{1}{\hbar}(g_F \mu_B \, B_z \, - \, \eta \, d_e \, E_{eff}) \end{aligned} \tag{1.18}$$

where $g_F = 1$, the signs of E_{eff} and B_z depend on the direction of the applied fields with respect to the z-axis, and the Stark shift has been ignored because it is the same for both states.[20] A time, t, after the *split* rf pulse the two states will have a phase difference of 2ϕ consisting of a magnetic field induced phase, $\phi_B = \frac{\mu_B B_z}{\hbar} t$, and EDM induced, $\phi_{d_e} = \frac{-\eta \, d_e \, E_{eff}}{\hbar} t$,

$$\begin{aligned} \phi(t) &= \phi_B(t) + \phi_{d_e}(t) \\ &= \tfrac{1}{\hbar}(\mu_B \, B_z \, - \eta \, d_e \, E_{eff}) t. \end{aligned} \tag{1.19}$$

An expression for the state of the system, ψ, at t can then be written as:

$$\psi(t) = \frac{-i}{\sqrt{2}}(e^{+i\phi}|1, +1\rangle + e^{-i\phi}|1, -1\rangle). \tag{1.20}$$

Before the packet of molecules leaves the interaction region the *recombine* phase of the experiment is carried out. This involves applying another rf π - pulse at a time τ (typically 660 μs) after the first pulse to drive electrons back into $|0, 0\rangle$. Due to interference, the efficiency of this process depends on the phase difference accumulated between the $|1, \pm 1\rangle$ states as follows,

[20] There is a minus sign between the magnetic and electric dipole moment interactions because the molecule's angular moment points in the direction opposite to its magnetic moment.

$$\frac{-i}{\sqrt{2}}\left[e^{+i\phi}|1,+1\rangle + e^{-i\phi}|1,-1\rangle\right] \rightarrow$$

$$-\left[\frac{e^{+i\phi}}{2}\left(|0,0\rangle + \frac{i}{\sqrt{2}}(|1,+1\rangle - |1,-1\rangle)\right) + \frac{e^{-i\phi}}{2}\left(|0,0\rangle - \frac{i}{\sqrt{2}}(|1,+1\rangle - |1,-1\rangle)\right)\right]$$

$$= -\cos(\phi)|0,0\rangle + \sin(\phi)\frac{(|1,+1\rangle - |1,-1\rangle)}{\sqrt{2}} = \psi_{final} \tag{1.21}$$

where the right hand side is the final state. The probability of electrons being observed in the $F = 0$ level is given by:

$$\begin{aligned} \langle\psi_{final}|0,0\rangle^2 &= \cos^2(\phi) \\ &= \cos^2\left(\tfrac{1}{\hbar}(\mu_B B_z - \eta\, d_e\, E_{eff})\,\tau\right). \end{aligned} \tag{1.22}$$

Similarly the probability of being observed in the $F = 1$ level is:

$$\langle\psi_{final}|1,+1\rangle^2 + \langle\psi_{final}|1,-1\rangle^2 = \sin^2(\phi). \tag{1.23}$$

Measuring the population in $F = 0$ or $F = 1$ with respect to different orientations of E_z and B_z tells us what ϕ and therefore d_e is. This is done in the *probe* phase of the experiment, where we measure the molecules in the $F = 0$ state by passing them through a second beam of 552 nm laser light, which is blue shifted relative to the *pump* beam by ∼170 MHz (see fig. 1.6), and recording the resulting laser induced fluorescence (LIF) with a photomultiplier (PMT). The PMT signal with respect to B_z takes the form of a $\cos^2$ curve as shown in fig. 1.7. Also shown is the effect a large eEDM would have on the curve when E_z is reversed. If d_e lies just below the current world limit at $5 \times 10^{-28}\, e$.cm and a field of $E_{app} = 10\,\mathrm{kV/cm}$ is used we would expect the phase shift in the figure to be $7\,\mu$rad (for $\tau = 660\,\mu$s). In terms of a frequency difference this corresponds to just under $\sim 2\,$mHz, which is equivalent to the Zeeman shift produced by a tiny magnetic field of only a fraction of a pT. This is one reason why the experiment is particularly challenging.

Since, we are interested in phase shifts it is most efficient to take data near the steepest parts of the interference curve, i.e., at $\phi = \pm\pi/4$. In practice, we modulate B_z between shots to acquire points **A**, **B**, **C** and **D** as shown in fig. 1.7. Hence, B_z can be thought of as being made up of the four combinations possible from switching a relatively large magnetic field $\pm B_0$ ($\sim 12\,$nT), and a smaller one $\pm DB$ ($\sim 1.5\,$nT). The sign of E_z is then reversed/switched (every 10 – 20 s) and points **A'**, **B'**, **C'** and

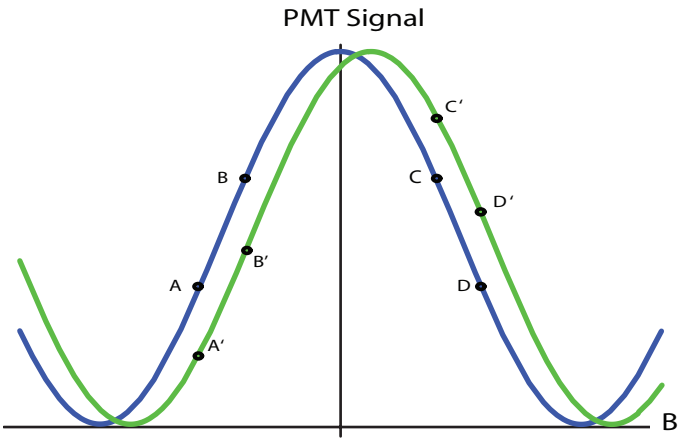

Figure 1.7: *The expected interference curve as B_z is incremented between shots. Taking a typical value of $\tau = 660\,\mu s$ the separation between two fringes on the same curve, i.e., a change in ϕ of π, corresponds to a magnetic field change of around 54 nT. The green curve represents the phase shifted signal after E_z is reversed; the shift is due to an EDM, which in this case is vastly exaggerated for clarity.*

D' are measured. If the signal depends on the relative directions of E_z and B_z we have a non-zero d_e[21], where the EDM signal is,

$$EDM\,\alpha\,(-\mathbf{A}-\mathbf{B}+\mathbf{C}+\mathbf{D}+\mathbf{A'}+\mathbf{B'}-\mathbf{C'}-\mathbf{D'}). \tag{1.24}$$

Each of the points here (**A**, **B**, **C**, etc.) correspond to what we term a *switch state* or *machine state*.

In principle only E_z needs to be switched to make an EDM measurement, but changing the polarity of B_z (by switching B_0) during data acquisition ensures a drifting background magnetic field is not interpreted as an EDM and by altering B_z's magnitude by a known magnetic field (DB) the slope of the interference curve can be evaluated for the purpose of calibrating the interferometer signal. We also modulate the rf, and laser parameters to provide us with other important diagnostic information. Full details of the data acquisition and analysis techniques will be provided in chap. 3.

[21] Assuming any systematic effects are absent/negligible.

1.7 Interferometer overview

A summary of the interferometer method and experimental setup is given below in fig. 1.8.

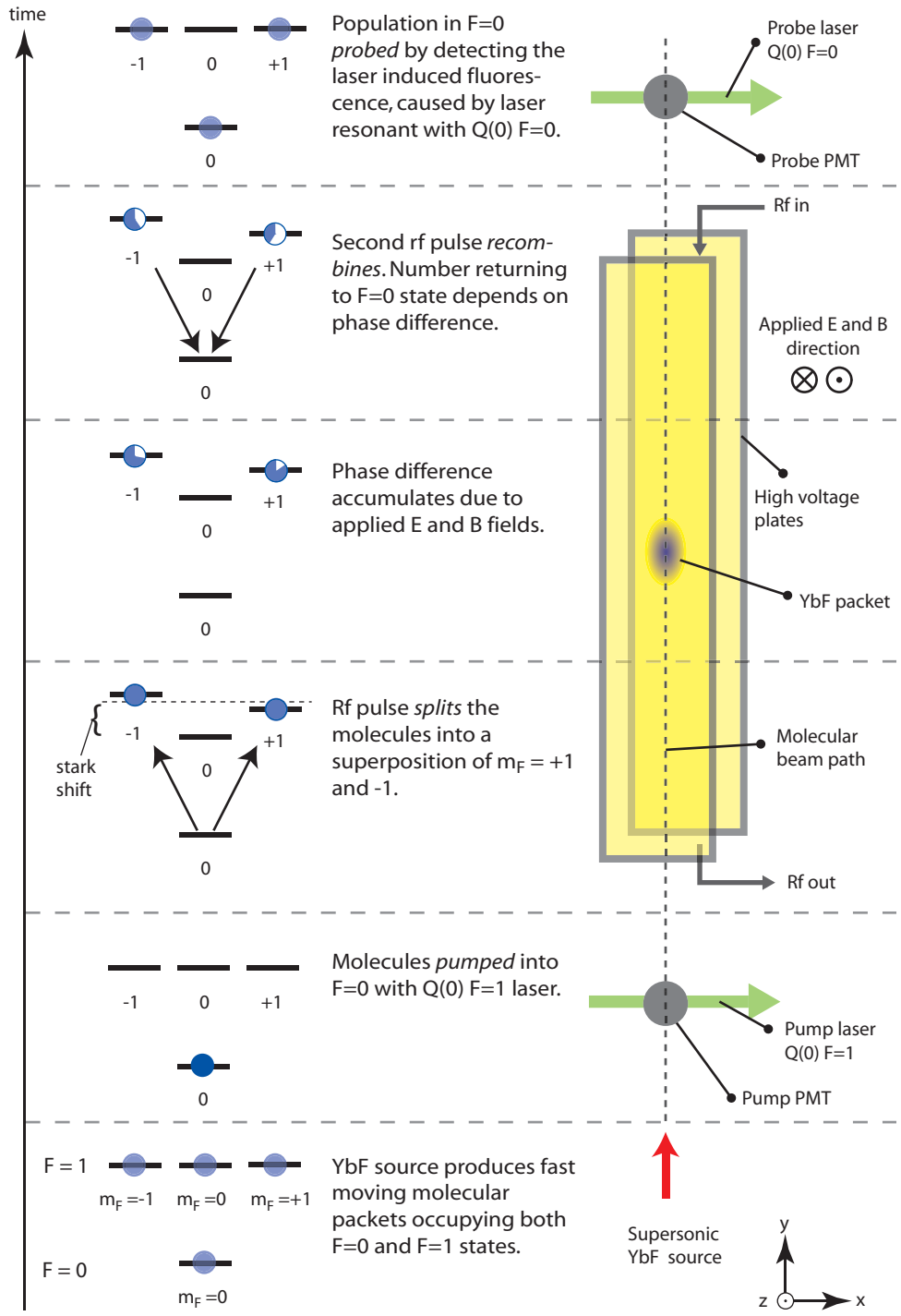

Figure 1.8: *An overview of the interferometer.*

Chapter 2

Experimental apparatus

An overview of the interferometric technique was given in the introduction and this chapter contains the details of the apparatus used to implement it. When I began my PhD the experiment was already capable of running as an interferometer. Much of my work has been to further automate the experiment and improve its reliability. Where possible, I focus on the changes and additions made to achieve this rather than repeat information in previous theses [41, 42, 29].

2.1 Apparatus overview

Fig. 2.1 is a simplified diagram of the experimental apparatus. Central to the experiment is the vacuum chamber, inside which the E - field plates and B - field coils sit. A YAG laser, which is used to ablate a solid Yb target in the supersonic YbF source, is affixed to the chamber. A 19″ rack holds the high voltage (HV) supplies, leakage current meters and a relay box for switching E. The B - field current supply electronics, rf system and breakout boards needed for computer control are mounted on a separate rack. Next to the chamber, on an optical table, is the dye laser system, which we derive the pump and probe beams from, and the I_2 lock used to frequency stabilise its output.

2.2 Vacuum chamber

The experiment must be carried out in vacuum so that the YbF quantum state is not scrambled through interactions with background gas. A low pressure is also conducive to supersonic expansion (see sec.2.3) and results in a large, stable flux of YbF. The chamber is cylindrical, made from stainless steel, about 2 m tall, 25 cm in diameter and consists of two sections: the main chamber and the source chamber. The main chamber contains the E - field plates, B coils and a magnetic shield which

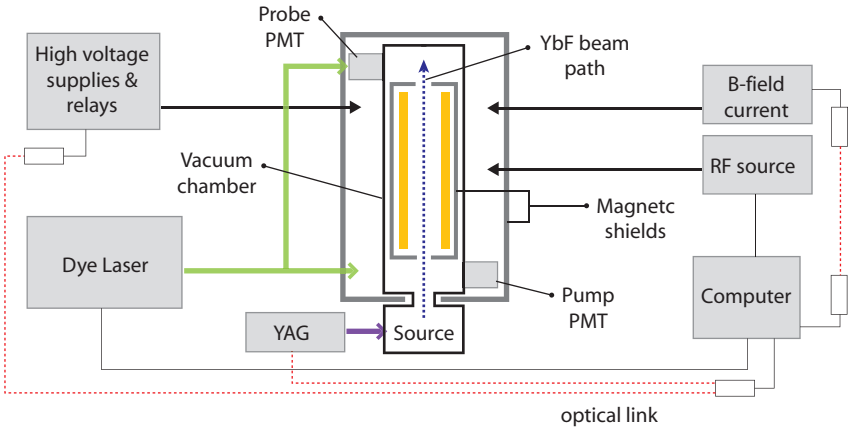

Figure 2.1: *A block diagram of the experimental layout. The HV plates are shown in yellow. The green and purple coloured arrows represent the pump/probe and YAG laser beams. The black lines and arrows indicate electrical connections.*

is referred to as the inner shield. A diagram of the chamber is given in fig. 2.2. All the components for producing YbF are in the source chamber. There is a gate valve between the two that is closed when the source chamber is opened for maintenance. Keeping the main chamber sealed is paramount, because contamination of the plates encourages electrical discharges at high voltage, severely reducing our reliability.[1]

A pair of turbo pumps on the main chamber and two larger ones on the source maintain a vacuum of about 7×10^{-7} mBar when the YbF source is not running and 4×10^{-4} mBar when it is.

2.3 The YbF beam source

To make an efficient measurement of the eEDM we wish to have a large flux of YbF molecules in their groundstate. This is achieved using the supersonic expansion technique which produces a pulsed, cold, but fast moving molecular beam. The technique was implemented in our experiment by Condylis. His thesis [42] contains the details. Compared to the continuous effusive oven source previously used this method results in a much higher flux of molecules in their ro-vibrational and electronic groundstate.

The basic idea behind supersonic expansion is to take a pressurised gas, a mixture of 98% Ar with 2% SF_6 at 4 Bar in our case, and release it into a vacuum through a small aperture. We control the release of gas with a valve that can open the aperture from anywhere between 100 to 200 μs. As the gas expands into the vacuum

[1] Large discharges are unwelcome because they can magnetise our shields, unlock our laser, cause hardware failures or crash the computer.

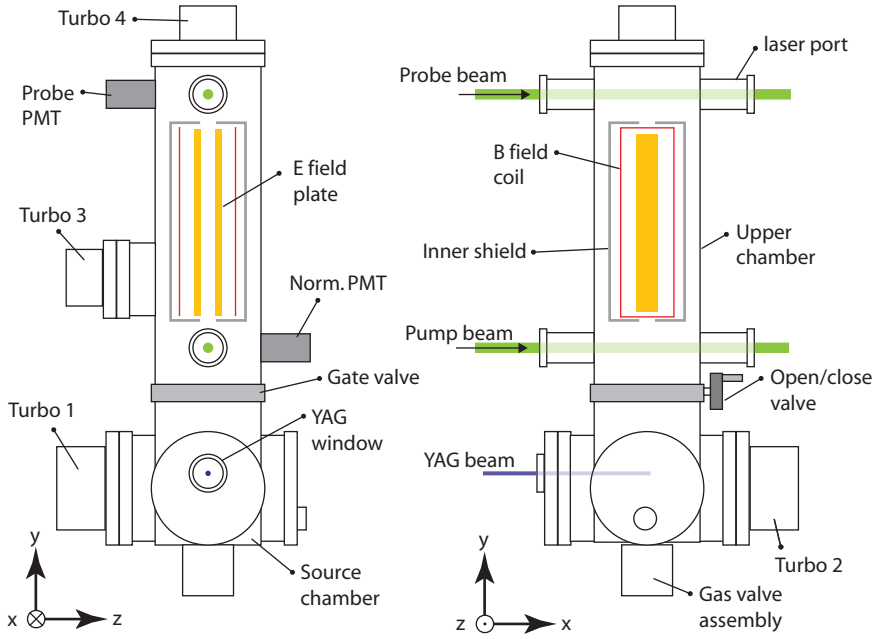

Figure 2.2: *The vacuum chamber and its main components. The cylindrical chamber is about 25 cm in diameter and 2 m in height.*

its thermal energy is converted into translational kinetic energy, resulting in motion along the y - axis.

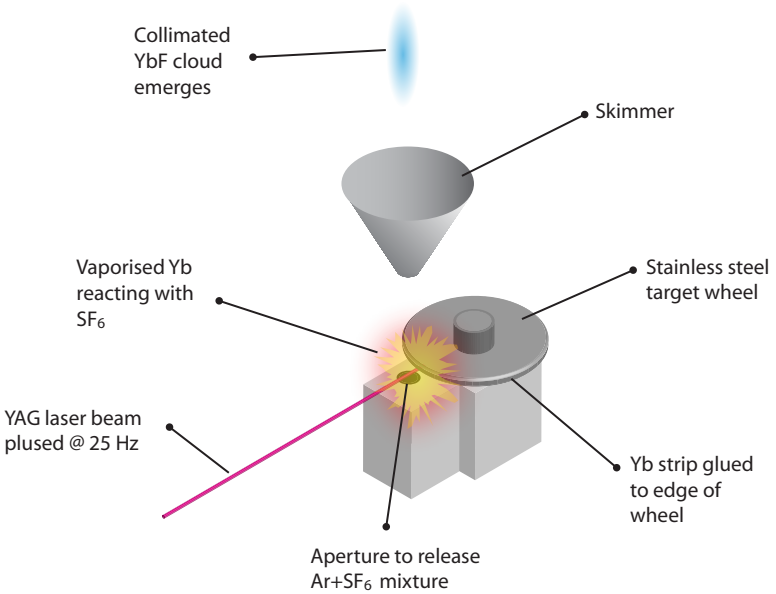

Figure 2.3: *The source setup. The Yb target is ablated in the presence of the expanding 98% Ar with 2% SF_6 mixture producing YbF. A portion of the cloud is selected by the skimmer and a collimated YbF packet emerges.*

In the presence of the expanding gas mixture we ablate a Yb target — a 1 mm thick and 3 mm wide strip of Yb mounted with Torr Seal on the edge of a 12 cm diameter steel disc/wheel — with a pulsed ND:YAG laser. The resulting hot Yb plume reacts with the SF_6 to produce YbF and this thermalises with the cold gas surrounding it. A skimmer, which has a 2 mm diameter aperture downstream selects a fraction of the moving cloud and a collimated beam emerges. A schematic of the setup is given in fig. 2.3.

Our source runs at a rate of 25 Hz and around 10^5 molecules per packet in their ro-vibrational groundstate, X $^2\Sigma^+$ ($\nu = 0, \mathrm{N} = 0$) pass through the probe beam.[2] The flux of 10^5 is inferred from the 1000 counts per shot we detect at the PMT's output by taking into account the solid angle of the detection optics and the quantum efficiency of the probe PMT. It is possible for the source and experiment to be run at 50 Hz, but the YbF flux per shot is reduced, mainly due to an increased pressure of the vacuum, and consequently there is no actual gain in sensitivity. As mentioned in sec. 1.6, the YbF travels at approximately 590 m/s with a FWHM velocity spread of 40 m/s, which corresponds to a translational temperature of ∼4 K.

When running on the same target spot for an hour or so the signal size decreases. Therefore, we have implemented an automated target rotator. The signal is analysed by the computer every $\sim$ 5 mins and if it falls below a pre-determined value the target wheel is automatically rotated a couple of degrees with a stepper motor. Other algorithms were tried, for example stepping the wheel by $\sim 10^\circ$ every 1 hr of data acquisition, but we find that generally large rotations less often result in more unstable signals.

After 5 – 7 days of continuous running the Yb target deteriorates to the point that its surface needs reconditioning. The source chamber is brought up to atmospheric pressure, the target wheel removed and around 100 μm is skimmed off the target on a lathe exposing fresh Yb. The process is not very disruptive and the machine is up and running within 1.5 hours. This can be repeated up to 5 times before the target is so depleted that it needs to be replaced with a fresh Yb strip. A newly glued target takes about 24 hours to cure. Therefore, we keep a spare disc on which a new target can be prepared while the machine runs.

The YbF flux and longterm stability also depend on the power of the YAG pulses and the time delay between them and the opening of the gas valve. The YAG power is adjusted by tuning the delay between the firing of its flashlamp and Q-switch.[3] The typical tuning procedure can be found in [41]. With the automatic stepper, the

[2] Higher rotational and vibrational states are also occupied but they play no part in the measurement.

[3] As the flashlamp ages the laser's output becomes unstable. When running around the clock the flashlamp needs replacing every 2 – 3 months.

target is fairly forgiving to the choice of parameters so we no longer need to stop the experiment every few hours to tune them. Instead, the parameters are only tweaked once a week, usually just after a target skim.

2.4 Pump and probe laser

The biggest change since the last thesis is that the 380D Spectra ring cavity dye laser has been replaced by an 899 Coherent which has proved to be far more stable. As discussed in sec. 1.6 the pump and probe beams are on resonance with the Q(0), $F = 1$ and $F = 0$ transitions respectively. The powers of pump and probe beams are 3 - 4 mW and 1.5 - 3 mW. Because they only differ by 170.25 MHz, two separate light sources are not required, instead an acousto - optic modulator (AOM) in the pump beam path is used to red shift the light. This AOM is referred to as the "pump AOM" to differentiate it from the one we use in the iodine, I_2, lock discussed later. The stability of the system is also much improved and it is now usual for us to stay locked for 10 – 15 hours, as opposed to the 4 – 5 hours with the old set up. This has been a big advantage because we can run through the night without anyone having to be in the lab to look after the experiment.

We use Rhodamine 110 dye pumped with an Ar+ laser lasing on all of its visible lines. As the dye gets older it becomes less efficient and requires more pump power to lase. This causes its output power to become unstable to the extent that it can not be easily locked with our I_2 system. The typical lifetime of the dye when pumped with 3 – 8 W, producing 150 – 180 mW of green light, is about 80 hours.[4]

2.4.1 Iodine lock

The 899 has an integrated reference cavity to which the laser is locked. A laser linewidth of less than 1 MHz is achieved, but the cavity itself drifts up to 10 MHz/hr. Since the Q(0) ($F = 0$) line has a FWHM of about 20 MHz, this level of drift would be problematic so we remove it with an I_2 saturated spectroscopy lock that feeds back to the cavity. The lock is described fully in Hudson's thesis [29]. The iodine feature that we wish to lock to is ∼120 MHz higher in frequency than the Q(0) ($F = 0$) transition. To bridge the gap an AOM is double passed to shift the laser frequency before it enters the lock. The AOM's driving frequency (120 MHz) is controlled by a voltage, V_{LF}, from the computer via a VCO. This means we have a convenient way of adjusting the locked laser's frequency in a linear and repeatable manner, albeit over a small range of $\sim 10 - 20$MHz.[5] The usefulness of this feature

[4] After this time a dye change is required and takes less than 2 hours.

[5] Over larger ranges the AOM becomes inefficient.

is demonstrated in sec. 3.2.4.

The laser unlocks if the optics table is disturbed otherwise it seems as if it is typically an instability in the dye laser cavity rather than the locking optics or electronics. One reason for this conclusion is that at the 380D spectra would only stay locked for 4 - 5 hours with an identical locking scheme. As already stated we can now lock for much longer periods of time and we have even remained locked for 2 days without intervention on occasions.

Changing the dye laser cavity was not the only thing that improved the performance. It was identified that the dye circulator pressure affects the amplitude noise of the laser output, and in turn the locking system. We optimise this empirically with the regulator on the circulator. Being aware of this dependence helps maintain the reliability of the system especially between dye changes when the regulator knob can be knocked. We have also found that the 899 is more stable when running at lower powers. The iodine lock used to require around 100 - 120 mW and when added to the power needed by the machine this meant a total of 200 mW of green light was needed from the dye laser. By tweaking the pump to probe[6] power ratio of the counter propagating beams in the I_2 cell and minimising light scatter from the optics we find 50 - 60mW is sufficient for the lock.

The benefit of running the laser at low powers is twofold: not only is the laser more robust, the time dedicated to dye changes is reduced because the dye does not degrade as quickly. Potentially the I_2 efficiency could be increased further by improving the cross - sectional overlap of the pump and probe beams with a telescopic lens setup.

Shortcomings of the current system are that it needs human attention twice a day, a dye change twice a week and if the dye laser cavity does get knocked it can take up to a day to bring back to life. Therefore, a solid state system has been developed, though it has not yet been integrated into the edm experiment. It is described in detail at the end of this chapter.

2.4.2 Pump/Probe optics and LIF detection

We measure the number of molecules in the $F = 0$ state[7] by recording the laser induced fluorescence (LIF) on the probe PMT as they pass through the probe laser beam. The YbF packet intersects the probe laser 1.3 m away from the source. At this position the molecular cloud spans about 100 mm in the y - direction, due to its 40 m/s velocity spread. Its dimensions in the $x \times z$ are limited to 70×10 mm by the aperture in the inner magnetic shield. A schematic of this is given in fig. 2.4.

[6] These refer to the pump/probe of the saturated spectroscopy lock not of our interferometer.

[7] When I refer only to hyperfine levels they belong to the $X^2\Sigma^+(v = 0, \mathrm{N} = 0)$ state.

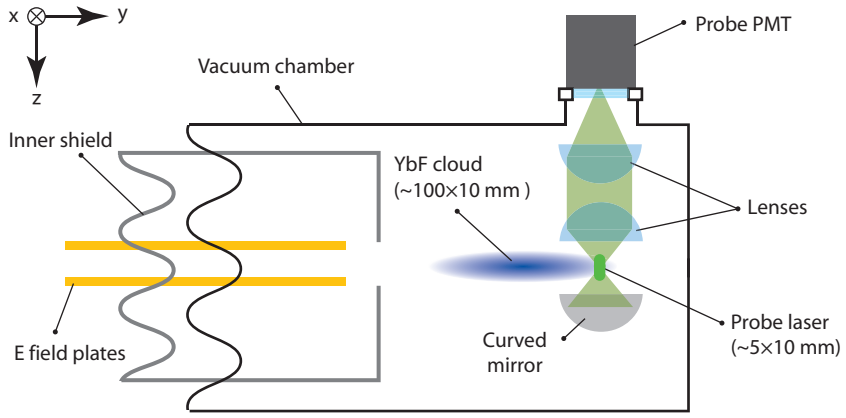

Figure 2.4: *Schematic of YbF cloud passing through the probe laser beam. The optical setup used to collect the fluorescence from the molecules is also shown.*

The probe laser profile is chosen to be 5 mm along y so that we get a time resolved profile of the YbF cloud (see fig. 2.5), referred to as a time of flight (TOF), and 10 mm along z to achieve a good spatial overlap with the molecules.

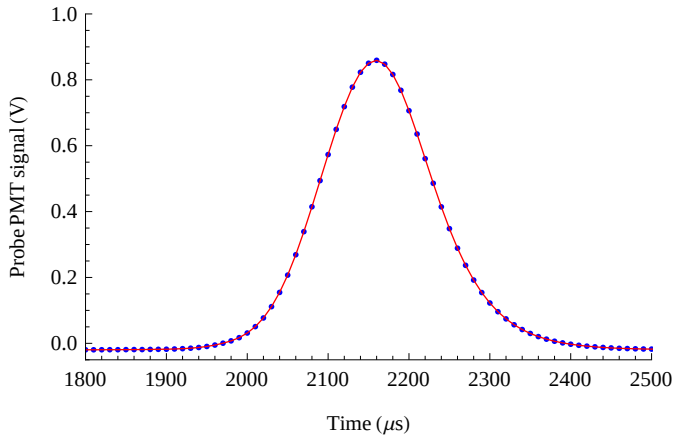

Figure 2.5: *PMT signal as the YbF cloud travels through the probe beam. The x - axis is the time after the firing of the Q - switch.*

The LIF when the cloud passed through the pump laser is recorded on a PMT, which is often termed the normalisation PMT because we can use the TOF data from it to normalise our probe signal on analysis. Each PMT is run in counting mode, and connected to circuitry (effectively an RC integrator) which converts the count rate into a voltage.

To investigate any possible effects related to the polarisation of the pump and probe lasers we periodically rotate their polarisations independently. We have employed the optics train shown in fig. 2.6 before each laser port to achieve this. It

consists of: a polarising beam splitter (PBS) cube to clean up the polarisation from the dye laser, which is in principle linearly polarised; a $\lambda/4$ plate with its slow (or fast) axis tilted 45° with respect to the beam cube so that the resultant light is circularly polarised; followed by a high quality Glan - Taylor cube (*Thorlabs - GT10 - A*) mounted on a motorised rotation mount (*Thorlabs - PRM1Z8*), which is computer controlled via a USB device (*Thorlabs USB DC Driver - TDC001*).

The $\lambda/4$ is not perfect, therefore the power entering the ports change by about $\pm 5\%$. This change is much less than the one which results from the dye laser output power drift. We have photodiodes that record the power of the pump and probe beams so we can also look for power dependent effects.

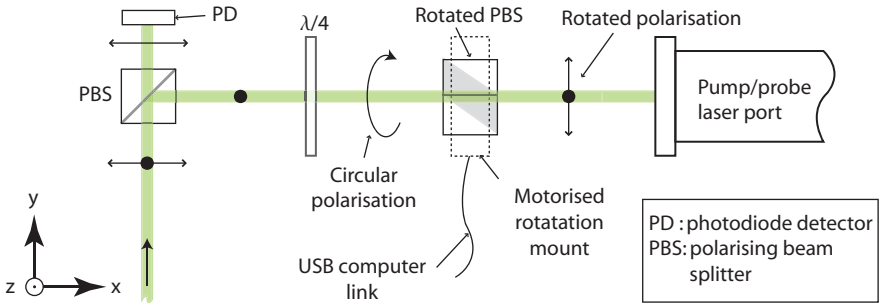

Figure 2.6: *Pump/probe polarisation rotator optics train.*

2.5 E and B fields

A high degree of control and knowledge of the electric and magnetic fields in our interferometer is vital to the experiment. We aim to apply E and B such that they are parallel fields in the z - direction. As well as these we need to consider any stray background fields.

2.5.1 E field control and application

Our large electric fields are produced between a pair of parallel gold coated (for improved field reversibility) aluminium plates that are 70 mm wide, 750 mm long and separated by 12 mm. Each plate is connected to a HV supply via a DPDT relay which is used for reversing the polarity of E. Two spring loaded feedthroughs are used to electrically connect the output cables of the relay box to the plates. They make contact at approximately the middle (in the xy - plane) of the plates.

The plates themselves are exactly the same as described in Ashworth's thesis, though the HV control system has been upgraded. The new setup is shown in fig. 2.7, with it we can now actively control the output of each HV supply, measure

the supply outputs and monitor leakage currents remotely from our computer. The

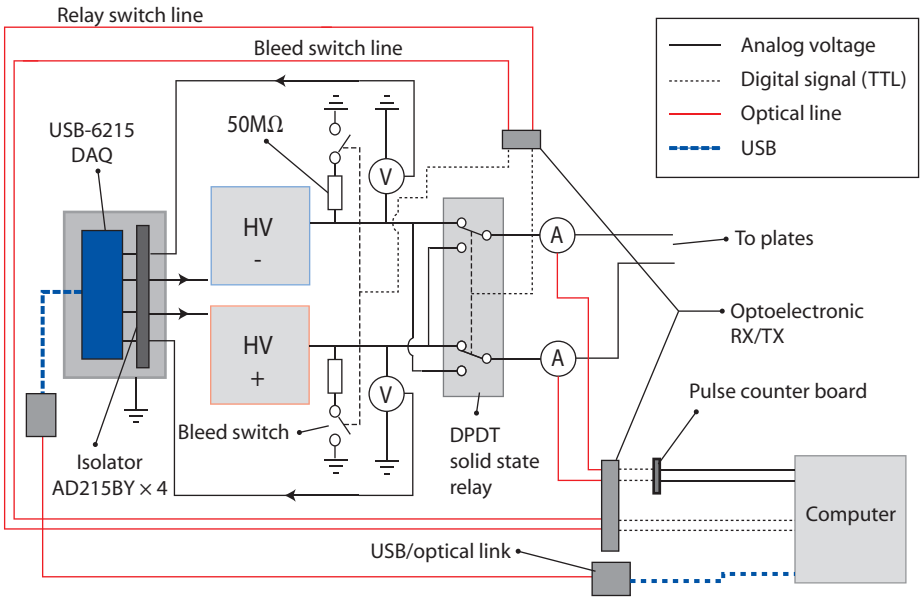

Figure 2.7: *A detailed schematic of our E field control system.*

old pneumatic relay system has also been replaced by a compact, low maintenance solid state one (*Crydom Reed Relay-D series (15 kV)*). As before, the state of the relay switches is set by an optically isolated digital signal (TTL) from the computer, S_E. To cancel out a class of systematics related to the relay state, for example the YbF detecting B-fields produced by the relays, we introduce an additional manual switch. This involves manually reversing the connections at the output of the relay box every 5 – 10 hours of data taking. Sec. 3.2.6 contains more information on this and other manual reversals we carry out.

To address the HV supplies and monitor their output a *National Instruments USB-6215* 16-bit DAQ device, connected to the computer with an optical USB link, is used. It provides the two program voltages (0 – 5 V) needed for controlling the HV supplies and two analog inputs which probe the supply outputs through 1:10000 potential dividers, i.e., 6 kV is measured as 0.6 V. To protect the device from possible discharges its input and output pins are each isolated with an *Analog Devices AD215BY* isolator.[8]

Two home-built floating ammeters, one in series with each plate, are used to monitor leakage currents. Their output, an optical pulse train whose frequency[9] is linearly related to the detected current, is measured on a counter board on the

[8] On occasion (once or twice a week) there is a discharge in the high voltage rack and without the isolators the device fails. This stops the data run and it can only be be reset manually by disconnecting it from its power supply.

[9] Centred at 10 kHz.

computer. The ammeters can detect sub - nA currents and after over a year of operation have not failed. Full details of the ammeter design can be found in [43]. The benefit of the voltmeter and ammeter setup is that we can now record the output of the supplies and currents while we take eEDM data, rather than having to rely on measurements made when the experiment is offline.

An E reversal basically involves setting the supplies to 0 V, switching the state of the relays and then turning the HV back on. With our active control of the supplies the rate of change of voltage and magnitude of current flow can be regulated during this process, meaning any induced B fields can be kept small so as not to polarise the magnetic shields. However, because of capacitance in the system a finite amount of charge often remains on the plates, even when the supplies are set to 0 V. This can cause a large instantaneous spike in current when the relays are thrown. Therefore, bleed switches with current limiting resistors (see fig. 2.7) have been added. Just before the relays are switched these are closed for 1 s to remove excess charge from the plates. When carrying out an E reversal data acquisition is paused so that the associated transients have time to settle before the experiment is resumed. The improved control of the HV hardware combined with a technique we call *overshooting*, discussed in detail in sec. 3.2.2, allows us to switch and settle the fields faster than the RC time of the system would usually let us. The upshot is that we have to introduce less dead time, in comparison to a passive system, to carryout the reversal.

2.5.2 B field

To reduce the influence of external magnetic fields two cylindrical mu - metal magnetic shields are used: the first 'outer' shield encloses the vacuum chamber, the second 'inner' shield sits inside the chamber. The outer and inner shields have shielding factors of $\sim$ 40 and 100 respectively. A pair of copper coils are wound on the inside of the inner shield. Current is driven through these to produce our applied magnetic field B_z. As described in sec. 1.6 we wish to modulate the field over four values when taking data. This is done by driving the coils with a current supply whose output, I_{out}, is switched with two computer controlled digital lines, S_{B_0} and S_{DB}.[10] I_{out} and the corresponding B_z is shown below,

$$\begin{aligned} I_{out} &= \pm |I_{B_0} \pm I_{DB}| + I_{bias} \\ B_z &= \pm |B_0 \pm DB| + B_{bias} \end{aligned} \tag{2.1}$$

where the measured calibration factor is 16.790 ± 0.003 nT/mA. Reading from left

[10] These are both optically isolated from the computer.

to right the first and second ±'s in eq. 2.1 relate to the high/low states of S_{B_0} and S_{DB} respectively. Therefore, switching S_{B_0} reverses the polarity of B_z and S_{DB} steps its magnitude. The magnitudes of I_{B_0} and I_{dB} are set manually via potentiometers on the current supply, such that: B_0 produces a phase shift $\phi_B = \pi/4$, and DB is large enough to modulate the interferometer output signal by an amount that can be easily resolved from noise, but is small enough to maintain a linear interferometer response. I_{bias}, which is used to compensate dc background magnetic fields, is programmed with a voltage, V_{bias}, from the computer. Another supply, used for diagnostic purposes, can scan the current in a continuous fashion over a range of ±20 mA.

As is done with the E field system we manually reverse the connections on the output of the current supply every few hours of data taking. Again this manual switching helps cancel a class of systematics.

It useful to know the general field in the lab. Hence, we have three mini - fluxgate magnetometers, *Stefan Mayer Instruments Magnetic Field Sensor - FLC100*, that record while we take data: one near the computer, another positioned above the optics table and a final one mounted on the HV supply rack. A more sensitive fluxgate, the *Bartington Mag - 03MCL100*, sits between the two magnetic shields and is used to veto data where the field was seen to become so large it could compromise the eEDM measurement.

2.6 rf field

As mentioned in sec. 1.6 pulses of rf - field are used to carry out the *split* and *recombine* phases of the experiment. From now on I will refer to these pulses as rf1 and rf2 respectively. Before discussing the hardware used to apply them a theoretical background of the transitions is given. This will include descriptions of the transition lineshape, Rabi oscillations and the lineshape of our interferometer's output.

2.6.1 rf transition theory

We begin by writing a general time - dependent state of the molecule in what is referred to as the z - basis representation[11],

$$\psi(t) = a_0(t)|0,0\rangle + a_+(t)|1,+1\rangle + a_-(t)|1,-1\rangle \tag{2.2}$$

where a_0 and $a_\pm$, the amplitudes of basis states $|0,0\rangle$ and $|1,\pm1\rangle$ respectively, can

[11] This constitutes taking the z - axis, the direction along which E_z and B_z are applied, as the quantisation axis.

be complex.

Selection rules forbid the rf-field, an oscillating magnetic field polarised along the x-axis, from coupling $|0,0\rangle$ with $|1,0\rangle$. Also the splitting between $|1,0\rangle$ and $|1,\pm1\rangle$ is far smaller ($\sim$ MHz for the E_z we typically apply) than the frequency of the rf field ($\approx 170\,\mathrm{MHz}$).[12] Hence, the $|1,0\rangle$ state is ignored and not included in eq. 2.2.

To see how ψ evolves in the presence of the oscillating magnetic field, $B_x\cos(\omega_{\mathrm{rf}}t+\phi)$, we must solve the time-dependent Schrödinger equation for the system[13],

$$i\hbar\frac{\partial a_z(t)}{\partial t} = \left[\hat{H}_0 + \hat{H}_{\mathrm{rf}}\right] a_z(t)$$

$$= \left[\begin{pmatrix} 0 & 0 & 0 \\ 0 & \hbar(\omega_0+\omega_z) & 0 \\ 0 & 0 & \hbar(\omega_0-\omega_z) \end{pmatrix} + \frac{\mu_B B_x\cos(\omega_{\mathrm{rf}}t+\phi)}{\sqrt{2}} \begin{pmatrix} 0 & 1 & 1 \\ 1 & 0 & 0 \\ 1 & 0 & 0 \end{pmatrix}\right] a_z(t) \tag{2.3}$$

where the $|0,0\rangle$ level has been taken as the zero of energy; $\hbar\omega_0$ is the energy, including the Stark shift from E_z, of the $|1,\pm1\rangle$ states; $2\hbar\omega_z$ is the Zeeman splitting of the states due to B_z; and a_z is the 3-column vector:

$$a_z(t) = \begin{pmatrix} a_0(t) \\ a_+(t) \\ a_-(t) \end{pmatrix}. \tag{2.4}$$

The process of solving eq. 2.3 is made more convenient by transforming into the x-basis, whose basis vectors are $|0,0\rangle$, $\frac{1}{\sqrt{2}}(|1,+1\rangle + |1,-1\rangle)$ and $\frac{1}{\sqrt{2}}(|1,+1\rangle - |1,-1\rangle)$. This is done by applying the transformation matrix, $U = \frac{1}{\sqrt{2}}\begin{pmatrix} \sqrt{2} & 0 & 0 \\ 0 & 1 & 1 \\ 0 & 1 & -1 \end{pmatrix}$, as follows,

$$i\hbar\frac{\delta a_x(t)}{\delta t} = \left[U\hat{H}_0U + U\hat{H}_{\mathrm{rf}}U\right] a_x(t)$$

$$= \left[\begin{pmatrix} 0 & 0 & 0 \\ 0 & \hbar\omega_0 & \hbar\omega_z \\ 0 & \hbar\omega_z & \hbar\omega_0 \end{pmatrix} + \frac{\mu_B B_x\cos(\omega_{\mathrm{rf}}t+\phi)}{\sqrt{2}} \begin{pmatrix} 0 & 1 & 0 \\ 1 & 0 & 0 \\ 0 & 0 & 0 \end{pmatrix}\right] a_x(t) \tag{2.5}$$

[12] Under normal operating conditions the linewidth of our rf pulses is no larger than 100 kHz.

[13] Incoherent processes, such as spontaneous decay, are negligible and so have not been included.

where the fact that $U^{-1} = U$ has been used and,

$$a_x(t) = \begin{pmatrix} a_0(t) \\ a_p(t) \\ a_m(t) \end{pmatrix} = U \begin{pmatrix} a_0(t) \\ a_+(t) \\ a_-(t) \end{pmatrix}$$

Note that in this basis $\psi = a_0|0,0\rangle + \frac{a_p}{\sqrt{2}}(|1,+1\rangle + |1,-1\rangle) + \frac{a_m}{\sqrt{2}}(|1,+1\rangle - |1,-1\rangle)$. Taking the rotating wave approximation this leads to the following coupled differential equations for the amplitudes,

$$i\dot{a}_0 = \frac{\Omega}{2} e^{i(\omega_{\rm rf} t + \phi)} a_p \tag{2.6a}$$

$$i\dot{a}_p = \frac{\Omega}{2} e^{-i(\omega_{\rm rf} t + \phi)} a_0 + \omega_z a_m + \omega_0 a_p \tag{2.6b}$$

$$i\dot{a}_m = \omega_z a_p + \omega_0 a_m, \tag{2.6c}$$

where $\Omega = \frac{\mu_B B_x}{\hbar}$ and is termed the Rabi frequency.

Though analytical solutions for the amplitudes can be found for these equations, the derivation involves cubic polynomials, which have expansive algebraic solutions. Therefore, the full working out is confined to appendix B. Here I take the simplified case where ω_z is assumed to be zero.[14] This is a fairly good approximation to our experiment since we have $B_x \gg B_z$. In the picture of precessing spins this means the time taken to complete an rf transition is much smaller than the inverse of the Larmor frequency $\omega_z = \frac{\mu_B B_z}{\hbar}$. Under this assumption the coupling between the $\frac{1}{\sqrt{2}}(|1,+1\rangle - |1,-1\rangle)$ state and the others disappears, essentially reducing the problem to that of the familiar two-level system, where the ground and excited state amplitudes are a_0 and a_p. Using the substitution $F_p = a_p e^{i(\omega_{rf} t + \phi)}$ it is then straightforward to re-write eq. 2.6 as a set of uncoupled differentials,

[14] The consequences of carrying out the recombine and split phases in a B-field will be discussed in sec. 4.2.6.

$$\ddot{a}_0 = i\delta\dot{a}_0 + \frac{\Omega^2}{4}a_0 \tag{2.7a}$$

$$\ddot{F}_p = i\delta\dot{F}_p + \frac{\Omega^2}{4}F_p \tag{2.7b}$$

$$\dot{a}_m = -i\omega_0 a_m, \tag{2.7c}$$

where $\delta = \omega_{\rm rf} - \omega_0$. These are readily solved using general solutions of the type $e^{i\omega_1 t}\left[A\cos(\omega_2 t) + B\sin(\omega_2 t)\right]$ and can be written in the form of a matrix (in the x - basis), which describes the action of an rf pulse of duration τ on an arbitrary initial state, as follows:

$$\mathbf{M}_{\rm RF} =$$

$$\begin{pmatrix} e^{i\frac{\delta}{2}\tau}\left(\cos\left(\frac{\overline{\Omega}\tau}{2}\right) - i\Delta\sin\left(\frac{\overline{\Omega}\tau}{2}\right)\right) & -ie^{i(\omega_{\rm rf}t_0+\phi)}e^{i\frac{\delta}{2}\tau}\beta\sin\left(\frac{\overline{\Omega}\tau}{2}\right) & 0 \\ -ie^{-i(\omega_{\rm rf}t_0+\phi)}e^{i(\frac{\delta}{2}-\omega_{\rm rf})\tau}\beta\sin\left(\frac{\overline{\Omega}\tau}{2}\right) & e^{i(\frac{\delta}{2}-\omega_{\rm rf})\tau}\left(\cos\left(\frac{\overline{\Omega}\tau}{2}\right) + i\Delta\sin\left(\frac{\overline{\Omega}\tau}{2}\right)\right) & 0 \\ 0 & 0 & e^{-i\omega_0\tau} \end{pmatrix} \tag{2.8}$$

so that $a_x(t_0+\tau) = \mathbf{M}_{\rm RF}\, a_x(t_0)$, and where $\overline{\Omega} = \sqrt{\delta^2+\Omega^2}$, $\beta = \Omega/\overline{\Omega}$ and $\Delta = \delta/\overline{\Omega}$.[15] From this matrix we can see that the rf drives $|0,0\rangle \iff \frac{1}{\sqrt{2}}(|1,+1\rangle + |1,-1\rangle)$ transitions as required for the split and recombine phases. Next I discuss how the transition probabilities and consequently the output of the interferometer depend on the rf parameters, beginning with a single rf pulse.

A single rf pulse

Single rf pulse experiments are regularly used for basic diagnostic purposes and a particularly important one is described in sec. 2.7. Assuming that the *pump* phase of the experiment is ideal then the initial amplitudes will be $a_0 = 1$, $a_p = 0$ and $a_m = 0$. In this case eq. 2.8 gives the ground and excited state probabilities as,

$$\begin{aligned} P_0 &= a_0 a_0^* = 1 - \frac{\Omega^2}{\overline{\Omega}^2}\sin^2\left(\frac{\overline{\Omega}\tau}{2}\right) \\ P_p &= a_p a_p^* = \frac{\Omega^2}{\overline{\Omega}^2}\sin^2\left(\frac{\overline{\Omega}\tau}{2}\right). \end{aligned} \tag{2.9}$$

[15] The $\omega_{\rm rf}t_0 + \phi$ term represents the initial phase of the rf - field.

The dependence of P_0, the population measured in the *probe* phase, on the detuning, amplitude and duration of the rf - field is summarised in fig. 2.8. Since P_p is simply given by $1 - P_0$ it is not plotted.

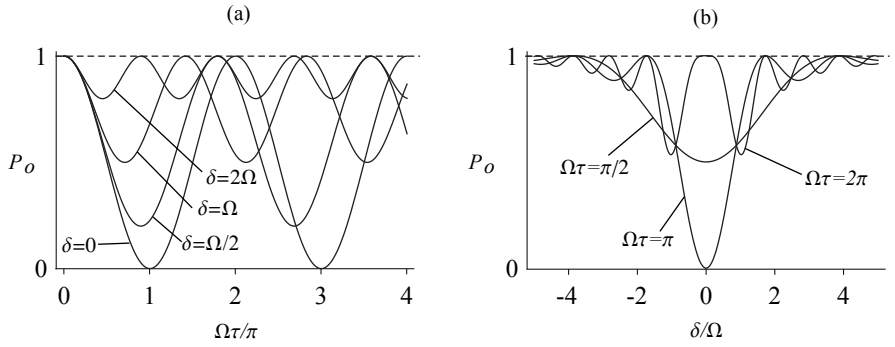

Figure 2.8: *In plot (a) the population oscillates back and forth between the ground and excited states as the duration of the pulse is scanned, these are termed Rabi oscillations. Their contrast decreases as the detuning is increased. The lineshape of the transition is shown in (b) for various rf amplitudes.*

From the plots we can see that the optimum population transfer occurs when $\delta = 0$ and $\Omega\tau = \pi$. This is referred to as a π - pulse. For the split and recombine phase of the experiment we should drive π - pulses to maximise the contrast of our interference fringes as will be shown next.

Interference

The application of two rf pulses, represented by $\mathbf{M}_{\mathrm{RF1}}$ and $\mathbf{M}_{\mathrm{RF2}}$ respectively, separated by an evolution time t_e and acting on an initial amplitude state $a_x(t = 0)$ is described as,

$$a_x(\tau_1 + t_e + \tau_2) = \mathbf{M}_{\mathrm{RF2}}\,\mathbf{M}_e\,\mathbf{M}_{\mathrm{RF1}}\,a_x(0) \tag{2.10}$$

where τ_1 and τ_2 are the durations of the first and second rf pulses, and

$$\mathbf{M}_e = U \begin{pmatrix} 1 & 0 & 0 \\ 0 & e^{-i(\omega_0+\omega_z)t_e} & 0 \\ 0 & 0 & e^{+i(\omega_0-\omega_z)t_e} \end{pmatrix} U$$

$$= \begin{pmatrix} 1 & 0 & 0 \\ 0 & e^{-i\omega_0 t_e}\cos(\omega_z t_e) & -ie^{-i\omega_0 t_e}\sin(\omega_z t_e) \\ 0 & -ie^{-i\omega_0 t_e}\sin(\omega_z t_e) & e^{-i\omega_0 t_e}\cos(\omega_z t_e) \end{pmatrix}.$$

Again, taking the case where all the initial population is in the groundstate the output of the interferometer is given by the expression,

$$P_0 = CONST + INT + RAMS \tag{2.11}$$

where

$$CONST = \left(\cos^2\left(\frac{\overline{\Omega}_1\tau_1}{2}\right) + \Delta_1^2\sin^2\left(\frac{\overline{\Omega}_1\tau_1}{2}\right)\right)\left(\cos^2\left(\frac{\overline{\Omega}_2\tau_2}{2}\right) + \Delta_2^2\sin^2\left(\frac{\overline{\Omega}_2\tau_2}{2}\right)\right)$$

$$INT = \beta_1^2\beta_2^2\cos^2(\omega_z t_e)\sin^2\left(\frac{\overline{\Omega}_1\tau_1}{2}\right)\sin^2\left(\frac{\overline{\Omega}_2\tau_2}{2}\right)$$

$$RAMS = 2\beta_1^2\beta_2^2\cos(\omega_z t_e)\sin\left(\frac{\overline{\Omega}_1\tau_1}{2}\right)\sin\left(\frac{\overline{\Omega}_2\tau_2}{2}\right)\times$$

$$\Big[\cos(\delta_e t_e+\phi)\left(-\cos\left(\frac{\overline{\Omega}_1\tau_1}{2}\right)\cos\left(\frac{\overline{\Omega}_2\tau_2}{2}\right) + \Delta_1^2\Delta_2^2\sin\left(\frac{\overline{\Omega}_1\tau_1}{2}\right)\sin\left(\frac{\overline{\Omega}_2\tau_2}{2}\right)\right)$$

$$+\sin(\delta_e t_e+\phi)\left(\Delta_1\sin\left(\frac{\overline{\Omega}_1\tau_1}{2}\right)\cos\left(\frac{\overline{\Omega}_2\tau_2}{2}\right) + \Delta_2\cos\left(\frac{\overline{\Omega}_1\tau_1}{2}\right)\sin\left(\frac{\overline{\Omega}_2\tau_2}{2}\right)\right)\Big],$$

δ_e represents the detuning of the rf oscillator during the evolution period[16] and ϕ the phase difference between the first and second rf pulses. It is worth re-iterating the assumptions and simplifications that were made in deriving this result: 1) we set $\omega_z = 0$ during the rf transitions, 2) the rf field was assumed to have a perfectly linear polarisation along the x-axis, 3) the rotating wave approximation was used and 4) the rf detunings and amplitudes were taken to be constant for the duration of each rf transition, i.e., there was no rf chirp.

CONST is a constant background term that is independent of T_e. *INT* represents the interference signal we use to measure the eEDM. It is a function of the phase

[16] Though the rf-field is turned off during the evolution period the rf synth is left on and therefore still winds phase.

difference acquired between the $|1,\pm1\rangle$ states (the phase is given by $\omega_z t_e$ in this case since the eEDM interaction has been ignored). The amplitude of it is maximised when both pulses are π - pulses ($\beta_1 = \beta_2 = 1$ and $\Omega_1\tau_1 = \Omega_2\tau_2 = \pi$). The final term *RAMS* is generally referred to as the Ramsey component. Its dependence on the phase $\delta_e T_e + \phi$, explicitly given by $\int_{t_i+\tau_1}^{t_i+\tau_1+T_e}(\omega_{\rm rf}(t)-\omega_0(t))dt$, means it is sensitive to the $|0,0\rangle \longleftrightarrow |1,\pm1\rangle$ energy splitting, $\hbar\omega_0$. This fact makes it a potential source of systematic error as will be discussed in sec. 4.2.3. Under typical operating conditions, where we aim to apply π - pulses to maximise *INT*, the Ramsey contribution is small. Nonetheless, we randomise ϕ when acquiring data to ensure any *RAMS* component in our output signal is washed out (see sec. 3.2.5).

Though Ramsey interference is troublesome to our eEDM measurement, it can be very useful for diagnostic tests, in particular for probing magnitude changes of E_z (ω_0 is a function of E_z). When carrying these tests out we run our experiment as a 'Ramsey' interferometer by setting $\Omega_1\tau_1 = \Omega_2\tau_2 = \pi/2$, which maximises *RAMS*. Sec. 3.2.2 contains one such example where we used Ramsey interferometry to measure the stability of E_z after a reversal.

The hardware used to apply the rf pulses is now described.

2.6.2 rf transmission line

The E - field plates are used as a waveguide to carry the rf - field. When the rf is turned on the whole region between the plates is filled with an rf - field polarised along the x - axis. Our rf source is isolated from the high voltage on the plates with capacitors as appears in fig. 2.9. Compared to a conventional loop antenna setup, which produces problematic inhomogeneous field regions (as discussed in the previous eEDM thesis), this is much more suitable for producing the linearly polarised and uniform oscillating field we require.

To turn the rf - fields on and off we use two fast switches (*Mini - Circuits ZASWA - 2 - 50DR*) in series, which provide an isolation of > 100 dBm when in the off state, before the amplifier as shown in fig. 2.9. These let us address the duration (typically 20μs) and separation of the rf pulses at the sub - μs level. The time that an rf pulse is applied is defined relative to the firing of the Q - switch, which we take to be the zero of time since this is when the molecules are created. The timing of events will be dealt with in more detail in sec. 2.8.

Despite the fact that there is just one rf source, a *HP8657A* synthesiser programmable over GPIB on the timescale of a few 100 ms[17], we can independently manage the frequency and amplitude of rf1 and rf2 using a frequency modulator (fm) internal to the rf synthesiser and an external rf attenuator. These are both con-

[17] The time between pulses is much smaller usually 660μs.

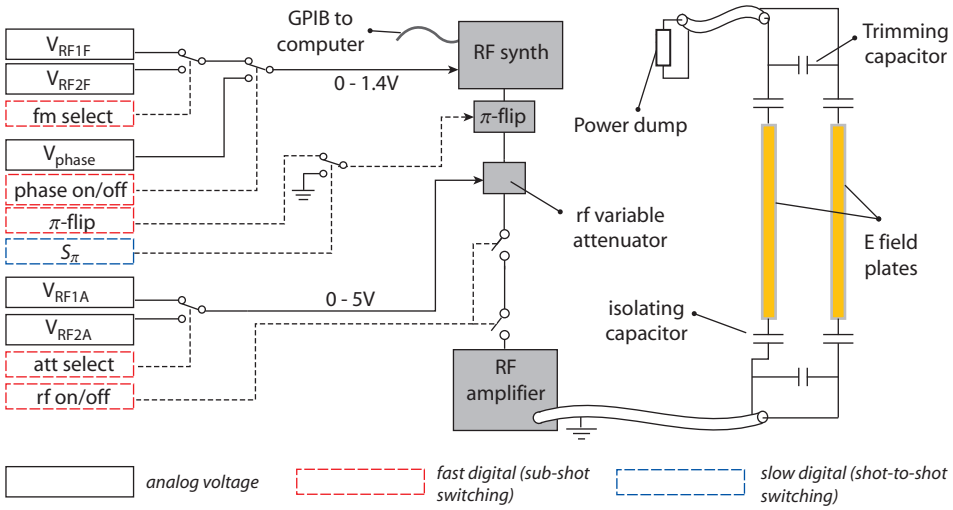

Figure 2.9: *rf control system required to drive the split and recombine phase of the interferometer. The direction of rf propagation is reversible — this diagram shows rf entering the bottom of the machine.*

trolled remotely from the computer with voltages, V_{RF1F}/V_{RF1A} and V_{RF2F}/V_{RF2A}, which set the fm/attenuation parameters for rf1 and rf2 as shown fig. 2.9. The fm's input of $0-1.4\,\mathrm{V}$ corresponds linearly to $0-20\,\mathrm{kHz}$.

Although not shown in the schematic, when the rf switches are in the off position the rf signal is diverted to a frequency counter (*Agilent 53131A*) and power meter (*HP438A*). This gives us a convenient and easy way to make measurements of the rf setup.

A phase difference of π can be introduced between the rf pulses with our 'π-flipper' box, controlled by a TTL line, S_π. By switching S_π from shot-to-shot during data acquisition we average the Ramsey component in the interferometer output to zero. We have measured that the flipper changes the phase to within 1% of π. If not dealt with properly Ramsey interference effects are a potentially large source of systematic error (see sec. 4.9). Therefore, a technique we call 'phase scrambling' is also implemented as a second line of defence against the problem. It relies on our ability to govern the fm with a voltage, which in turn allows us to add a known, but arbitary, phase difference between the two pulses. Details are given in sec. 3.2.5.

By manually reversing the cables which couple rf in and out of the machine we can reverse the propagation direction of the rf. During data acquisition we periodically carry out this manual reversal to check if there are any systematic effects that depend on this parameter.

With the transmission line setup the whole region between the plates is filled

with an rf-field when turned on. This means we have the added benefit (over loop antennae) that we can drive rf transitions anywhere along the length (in the y-direction as defined in fig. 2.2) of the plates. By taking advantage of this property we have been able to use the YbF molecules as a probe to map the static E and B-fields in the interaction region.

2.7 Field maps

From the field mapping experiment we wished to measure the magnitude of E_z, the applied B-field, B_z, and the ambient B-field as a function of position in the y-direction (defined in fig. 2.2). To do this a series of single rf pulse experiments were carried out as follows. Fields of around $E_z \approx 11\,\mathrm{kV/cm}$ and $B_z \approx 2\,\mu\mathrm{T}$ were applied. For reasons that will become clear later this large B_z was chosen so that the single resonance feature (see fig. 2.8 (b)) splits into two due to the Zeeman shift of the $|1,+1\rangle$ and $|1,-1\rangle$ states.[18] The duration of the rf pulse was chosen to be $50\,\mu\mathrm{s}$, small enough that the molecules did not move far in this time but large enough that the splitting could be easily resolved. We then incremented the rf pulse frequency from shot-to-shot to record the rf transition lineshape for a fixed rf timing. One such scan, where the Zeeman split resonance is clearly evident, is shown in fig. 2.10.

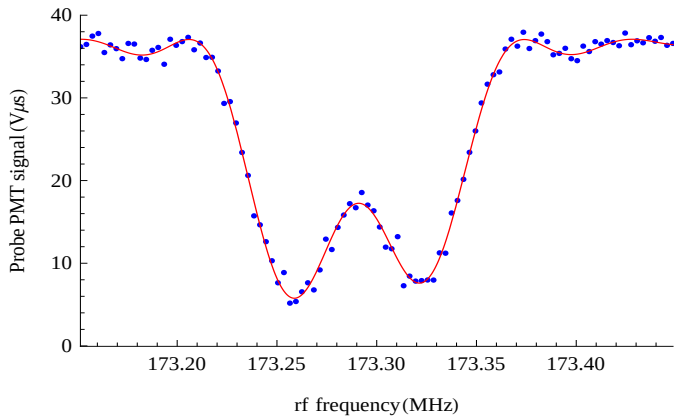

Figure 2.10: *The rf lineshape produced by scanning the frequency over the resonance. A double function of the type given in eq. 2.9 is fitted to the curve. The center of the feature is related to the magnitude of E_z, the separation of the peaks to the size of B_z and the asymmetry in their heights to a circularly polarised component in the rf driving field.*

This was then repeated after changing the rf timing, where increasing the time

[18] In this case we were no longer in the regime I assumed in deriving eq. 2.9, where I took $\omega_z = 0$.

meant the rf pulse was administered when the YbF packet was further along the y-axis. In this manner we built up a collection of resonance curves for various positions along the length of the interaction region. Since we record the time (relative to the firing of the Q-switch) at which the molecules pass the probe PMT (see fig. 2.5) and know the distance of the PMT from the ablation region it is simple to convert an rf timing into a corresponding YbF packet position. Further details can be found in [44].

2.7.1 E-field map

The center of the transition (the mean frequency of the two peaks) in fig. 2.10 can be used to infer the magnitude of E_z, because the relationship between the Stark shift and an electric field is known accurately. The E-field map that results from fitting our rf lineshapes is displayed in fig. 2.11. It can be seen that the field of $\approx$11 kV varies by about 200 V/cm. We were not aware of the E-field wobble shown in the

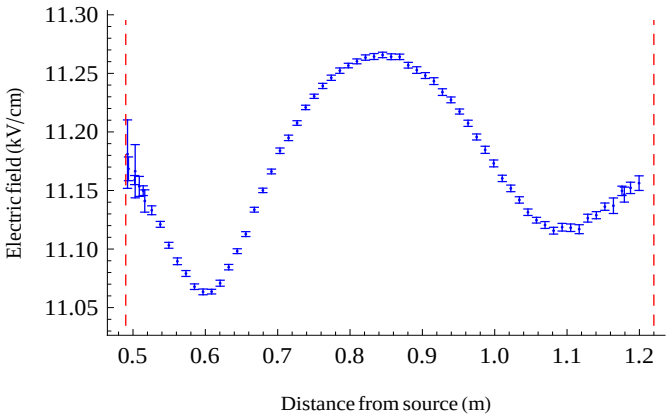

Figure 2.11: *A map of the applied E fields. The red, dashed lines denote the edges of the electric field plates.*

figure before the field mapping data was taken. It corresponds to a change in plate separation of 100 μm and arises because the plates, which are mounted at 0.6 and 1.1 m, bow under the pressure from the spring loaded HV feedthroughs that make contact at about 0.85 m. This field map information is very important especially when investigating and quantifying possible systematic errors.

2.7.2 B-field map

The separation of the two peaks in fig. 2.10 is proportional to the size of the magnetic field in the z-direction. We are insensitive to fields perpendicular to E_z because the Stark effect shifts the $|1, \pm 1\rangle$ states away from $|1, 0\rangle$. This property will be explained in sec. 4.2.5. To make a distinction between an applied field and an ambient field

we repeated the lineshape measurements with the direction of B_z reversed, where the sum and difference of the splittings told us the applied and ambient components respectively.

We see a pretty uninteresting and homogeneous B_z from our coils, but the ambient field is very large (about 100 nT) toward the ends of plates as shown in fig. 2.12. This is one of the reasons we can not use as much of the region between the E plates as we would like. We think it could be coming from the end caps on the inner cylindrical magnetic shield.

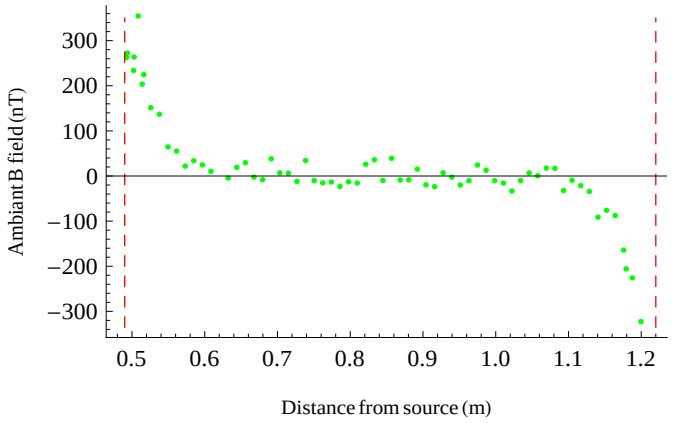

Figure 2.12: *A map of the ambient B-field in the z-direction as function of position along the y-axis. The red, dashed lines denote the edges of the electric field plates.*

2.7.3 rf polarisation field map

In the discussion of the rf transition theory the magnetic rf-field was assumed to be of perfect linear polarisation along the x-axis. However, if there is a small circular component then one of the states $|1,+1\rangle$ or $|1,-1\rangle$ will be coupled more strongly to $|0,0\rangle$ by the oscillating field. This is because the right and left-hand circularly polarised components (about the z-axis) of the rf drive molecules into the $|1,+1\rangle$ and $|1,-1\rangle$ states respectively. Therefore, by looking at the relative amplitudes of the two peaks in the Zeeman split transition we can infer the ellipticity of the field. The rf-field map is given in fig. 2.13, where it is evident that there is some ellipticity toward the edge of the plates.

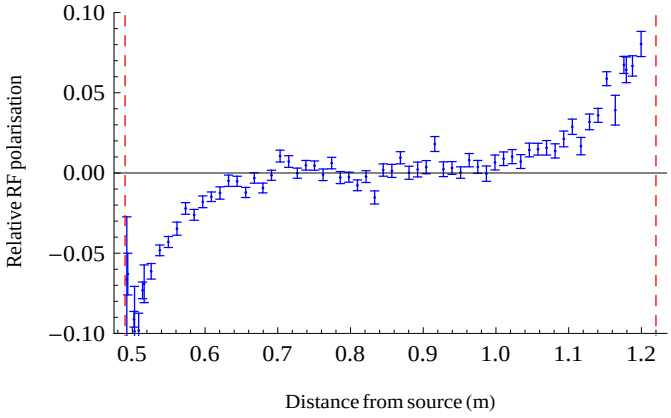

Figure 2.13: *A map of the rf polarisation with the rf entering at the top of the plates. On the y-axis -1 corresponds to full LH circular, +1 to RH and 0 to linear polarisation, with respect to the molecular quantisation axis (parallel to E and pointing in the direction of the B field). The red dashed lines denote the edges of the electric field plates.*

We think rf radiation from the HV isolating capacitors, which are attached toward the ends of the plates, is the culprit, because from a parallel plate waveguide a very pure linear polarisation would be expected.

As mentioned earlier it is possible to send the rf into the bottom and out of the top of the plates or vice - versa. Reversing the propagation direction reverses the sign of the polarisation i.e. the curve in fig. 2.13 is reflected in the x - axis. This gives a useful diagnostics handle for detecting systematic errors related to rf polarisation. During typical data acquisition we apply rf1 and rf2 when the molecules are in a region where the polarisation is fairly linear, corresponding to 0.6 m and 1 m respectively in the field map figure.

2.8 EDM computer

The last piece of hardware to be discussed is the computer. It is interfaced with the apparatus through a variety of PCI cards, and USB and GPIB devices as shown in fig. 2.14.

Since the pump and probe PMT signals provide the raw data used to measure an EDM, special considerations were taken when choosing the card, *PCI - 6133*, on which to acquire them. Firstly, the card has isolated inputs[19] with each having a dedicated analogue to digital converter (ADC), limiting the level of interference from ground and of crosstalk between its inputs. Secondly, its maximum specified sample

[19]Isolated from ground and each other.

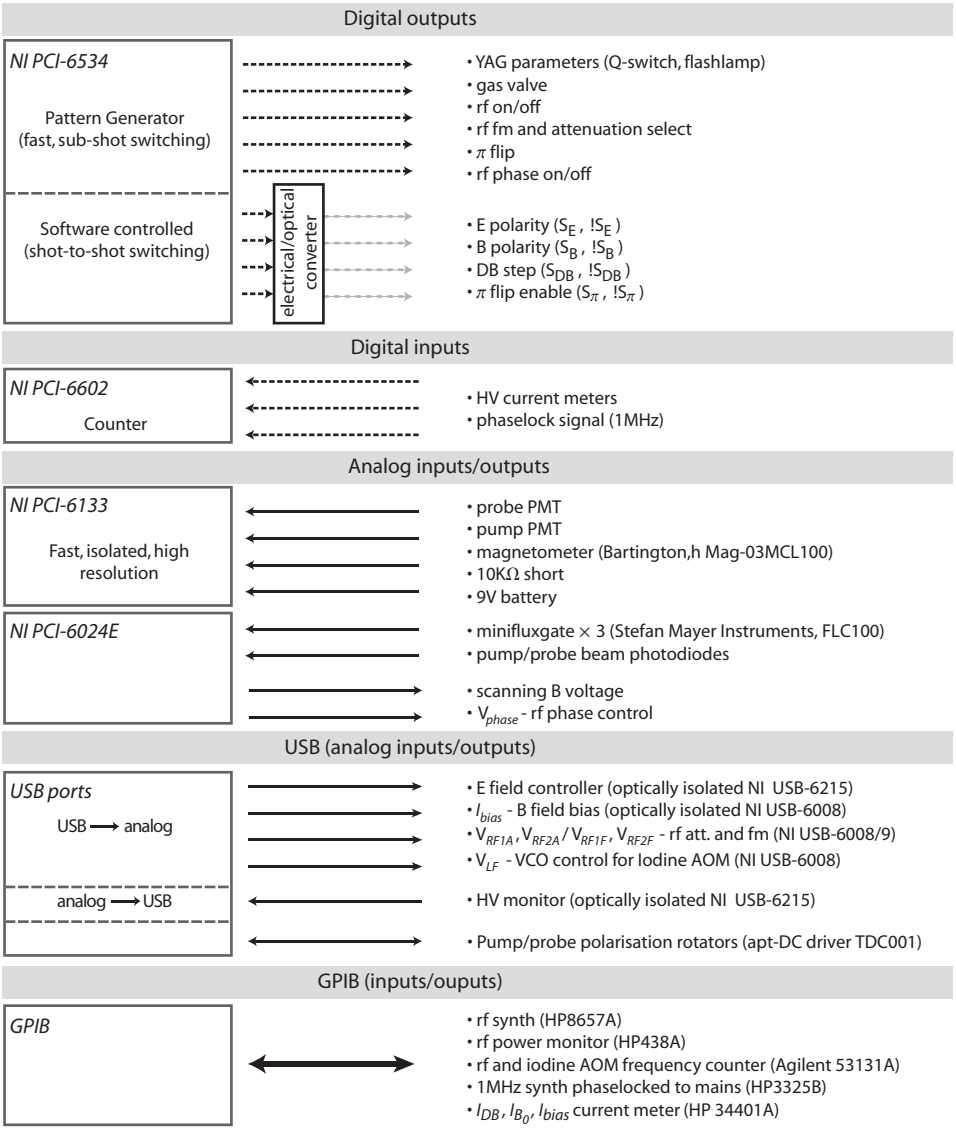

Figure 2.14: *Diagram of the computer's various inputs and outputs.*

rate, 3 MHz, is larger than the 1 MHz we actually acquire at — the PMT amps are set up such that their RC times are around 1 μs. This overspecification keeps us well away from possible problems caused by settling times of the card. The *Bartington* fluxgate magnetometer is also recorded with this card. As an extra precaution, two additional 'null' inputs, one shorted through a 10 KΩ resistor and another connected to a 9 V battery, are recorded during data acquisition. These are used for diagnostic purposes, for example, if we see a signal on the short correlated with the polarity of E something is obviously wrong. Though the mentioned inputs are all sampled in an identical fashion they are processed differently at the end of a shot by the control software: the pump and probe PMT signals are gated so that only data for times when fluorescence would have been expected is stored, the battery signal is gated

with the same limits as the probe, and the short and magnetometer are not gated but their data is averaged every 20 samples.[20]

As mentioned already, when running the experiment shots are fired at a rate of 25 Hz and complete their journey through the interaction region in 1 ms. Anything that needs to be switched during a shot is controlled by the hardware timed pattern generator (PG), which can output digital signals with 1 μs timing granularity. Although not shown in fig. 2.14, the PG board also provides the triggering signal for the analog input cards. All the other digital lines and USB devices can be addressed on a shot-to-shot basis and the GPIB on the order of a few hundred ms.

The switches S_E, S_{B_0}, S_{DB} and S_π each have a corresponding NOT switch, denoted by a '!' preceding their labels in fig. 2.14. These NOT switches do not actually control any hardware, but minimise the net magnetic fields produced by the electronics associated with the digital lines, in particular the current drivers of the LEDs used for optical isolation.

The experiment's clock, used as a timing reference by the PG board, is derived from a 1 MHz oscillator that is software phaselocked to the mains supply. In brief, it involves the computer continuously shifting the frequency of the oscillator to keep its output in phase with the AC mains voltage. This synchronisation suppresses the influence of 50 Hz mains magnetic field noise on our experiment. Over the duration of a block this changes the definition of a second from shot-to-shot by no more than 1 part in 10000.

2.8.1 Firing a shot

Fig. 2.15 details the list of digital instructions sent out by the PG board when a shot is fired and the corresponding events with respect to time. We refer to this list as a 'pattern'. Because a pulsed YbF source (rather than a continuous beam) is used in this experiment, a given position on the timeline corresponds to a well defined spatial position of the molecular packet in the machine (along the y-axis). Therefore, in the figure, time and position can be considered interchangeable. When programming the timing of events for our pattern we define $t = 0$ to coincide with the opening of the Q-switch.

[20] This is to limit the amount of redundant information that is stored per shot.

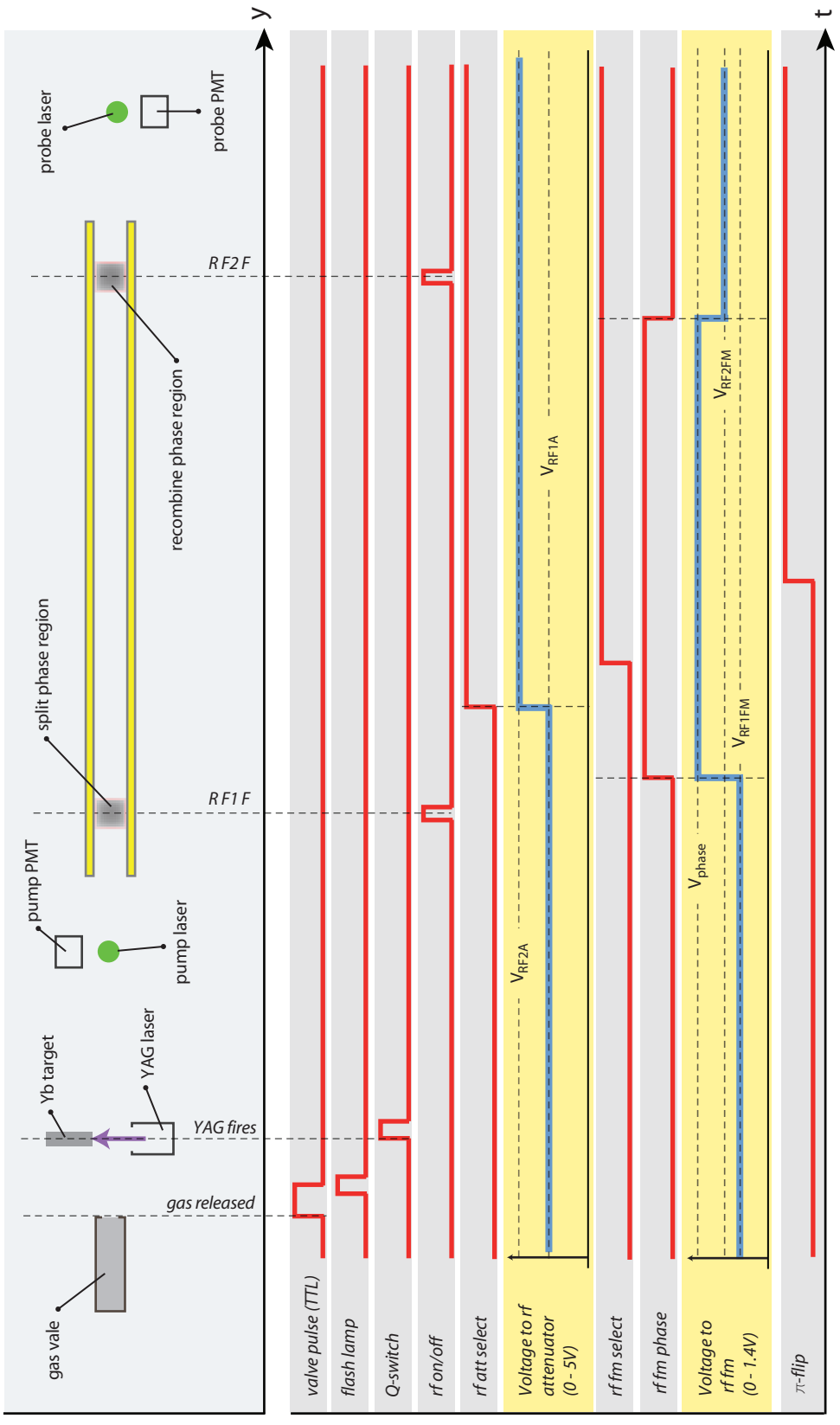

Figure 2.15: *Schematic showing what happens when a shot is fired. Time and position can be considered interchangeable.*

2.9 Frequency Doubling of 1104 nm

The frequency doubling of 1104 nm light was proposed because of the commercial availability of narrow linewidth and powerful infrared fibre lasers. These solid - state devices are particularly suitable for automation purposes as they are a reliable and stable radiation source.

We frequency double 900 mW of IR from a Koheras Boostik Fibre laser into over 150 mW of green. This is done using a nonlinear crystal, Lithium triborate (LBO), inside an enhancement cavity resonant with the IR light. Using such a setup it is possible the EDM experiment could run for a week or more without human intervention.

Since this a new addition and similar systems may be made for use on other experiments in the CCM, this section contains a thorough description of the setup starting with the principles of nonlinear crystals and frequency doubling, followed by details of the design, construction and performance of the doubling cavity. An overview of the setup is given in fig. 2.16.

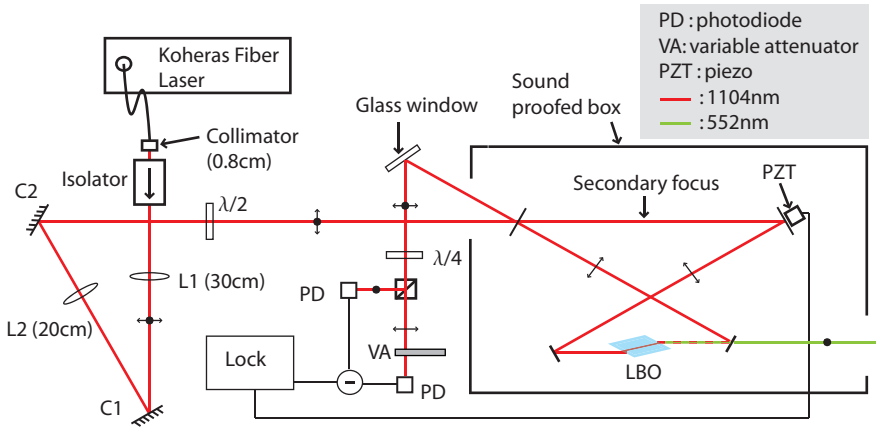

Figure 2.16: *Overview of the doubling laser system where the distance L1 to L2 is 49 cm and L2 to the secondary focus is 70 cm. C1 and C2 are adjustable coupling mirrors.*

2.9.1 Nonlinear crystals

In the presence of an electric field, E, the valence electrons of a dielectric crystal are shifted from their equilibrium position and the medium becomes polarised. This induced polarisation, P (defined as the dipole moment per unit volume), is related to E in the following way:

$$P(E) = \chi E + \chi^{(2)} \cdot E^2 + \chi^{(3)} \cdot E^3 + \ldots, \tag{2.12}$$

where χ is the linear susceptibility, and $\chi^{(2)}$, $\chi^{(3)}$ and so on are the nonlinear susceptibilities of the material. In general $\chi^{(n)}$ and E are a tensor (of rank $n+1$) and vector respectively, but for now this is not important and both can be treated as scalars. For a linear medium all the $\chi^{(n)}$ terms vanish (only χ takes a value) and in the nonlinear case at least one $\chi^{(n)}$ is $\neq 0$. These non-zero terms arise from the fact that the energy potential, $V(x)$, of an electron in a nonlinear material is not just a simple harmonic well, but contains higher orders as shown:

$$V(x) = \alpha x^2 + \beta x^3 + \gamma x^4 \ldots, \tag{2.13}$$

where x is the electron's displacement, and α, β and γ are coefficients which give rise to χ, $\chi^{(2)}$ and $\chi^{(3)}$ respectively. A derivation relating these coefficients to the corresponding susceptibilities can be found in [45].

Efficient frequency doubling requires a crystal which has a relatively large $\chi^{(2)}$ term. This can be demonstrated by putting a fundamental field of frequency ω, $E\cos\omega t$, into eq. 2.12:

$$\begin{aligned} P(E) &= \chi E\cos\omega t + \chi^{(2)}E^2\cos^2\omega t \\ &= \chi E\cos\omega t + \chi^{(2)}\frac{E^2\cos 2\omega t}{2} + \chi^{(2)}\frac{E^2}{2} \end{aligned} \tag{2.14}$$

where the trigonometric identity $\cos^2\theta = \frac{\cos 2\theta + 1}{2}$ has been used. The equation shows that a driving field at ω produces a field proportional to $\chi^{(2)}E^2$ at 2ω. For this to be possible $\beta \neq 0$ and, consequently, $V(x) \neq V(-x)$. Therefore, only crystals without an inversion symmetry — anisotropic crystals — can be used for second harmonic generation (SHG).[21] Anisotropic crystals fall into two categories: *uniaxial*, which have one axis of propagation where the refractive index, n is independent of polarisation (referred to as the optical axis) and *biaxial* — which have two optical axes.[22] Along all other directions light experiences a polarisation dependent n, i.e. a birefringence.

This turns out to be a favourable property, because it aids in solving the problem of phase matching (see sec. 2.9.2). Next we calculate the expected doubling efficiency of 1104 nm radiation with LBO and look at $\chi^{(2)}$ in more detail.

[21] This is a necessary but not sufficient condition for a crystal to be suitable for SHG.

[22] For a uniaxial crystal the crystallographic axes, X, Y, and Z are defined such that Z is along the optical axis, for a biaxial crystal the XZ plane is usually defined to contain the two optic axes.

2.9.2 Theory of Conversion Efficiency

Conversion efficiency is reduced if the fundamental and SH waves do not stay in phase with each other as they travel through the crystal. This is because destructive interference occurs when the two waves become exactly out of phase and power in the SH starts being converted back into the fundamental. Assuming that a negligible fraction of the input power at ω is depleted as it travels through a crystal, of length l, the conversion scales as,

$$\frac{sin^2\left(\frac{\Delta k l}{2}\right)}{\left(\frac{\Delta k l}{2}\right)} \tag{2.15}$$

where Δk is the phase mismatch between the two waves, and is defined:

$$\begin{aligned} \Delta k &= k_{2\omega} - 2k_{\omega} \\ &= \frac{2\omega n_{2\omega}}{c} - \frac{2\omega n_{\omega}}{c} \end{aligned} \tag{2.16}$$

where n_ω is the refractive index at ω and the factor of 2 in front of k_ω accounts for the fact that the fundamental has half the frequency of second harmonic. As can be seen from eqs. 2.15 and 2.16 the refractive index needs to be the same for both frequencies for maximum conversion efficiency, but for a given direction of light polarisation and propagation n usually increases with ω and the condition can not be met.

The problem can be overcome by taking advantage of the birefringence in the nonlinear medium since it is possible to obtain $\Delta k = 0$ if the two fields are polarised along orthogonal axes.[23] This phase matching can be achieved in one of two ways: 1) the angle of propagation relative to an optic axis is chosen such that $n_\omega = n_{2\omega}$, or 2) the propagation direction is chosen to be along or perpendicular to an optic axis, and using the temperature dependence of n, the temperature is adjusted to set $\Delta k = 0$. The former is referred to as "critical phase matching" (CPM) because the phase matching is particularly sensitive to the angle of propagation and the latter "non - critical phase matching" (NCPM) because along or perpendicular to an optical axis the refractive index changes very little with respect to the propagation angle and hence, the phase matching condition is relatively insensitive to small changes in beam direction. Of course, for a given ω phase matching can only be achieved with particular crystals, either because the birefringence is not pronounced enough or the temperatures required are not attainable. One major advantage of NCPM is that a

[23] Here the tensor properties of χ are relevant, because an E along one axis is generating a field in another.

detrimental effect known as spatial walk - off is avoided. This will not be discussed further because we implement NCPM.

So, crystal choice is limited by whether phase matching is possible, but another factor to consider is the coupling strength between the fundamental and SH fields. For this we need to look at the tensor form of $\chi^{(2)}$. Working in the crystal's coordinate system X, Y, Z and assuming that $\chi^{(2)}$ is the only nonlinear term,

$$\begin{pmatrix} P_X^{(nl)} \\ P_Y^{(nl)} \\ P_Z^{(nl)} \end{pmatrix} = \begin{pmatrix} d_{11} & d_{12} & d_{13} & d_{14} & d_{15} & d_{16} \\ d_{21} & d_{22} & d_{23} & d_{24} & d_{25} & d_{26} \\ d_{31} & d_{32} & d_{33} & d_{34} & d_{35} & d_{36} \end{pmatrix} \cdot \begin{pmatrix} E_X^2 \\ E_Y^2 \\ E_Z^2 \\ 2E_Y E_Z \\ 2E_X E_Z \\ 2E_X E_Y \end{pmatrix} \tag{2.17}$$

where d_{mn} are elements of the $\chi^{(2)}$ tensor, $E_{X,Y,Z}$ and $P_{X,Y,Z}^{(nl)}$ are the E and nonlinear P components along the respective crystal axes.[24] For a given propagation direction and phase matching scheme the matrix in eq. 2.17 is used to find what is known as the effective non - linear coefficient, d_{eff}, for the crystal. It represents the coupling strength between the waves at ω and 2ω and needs to be large (or at least non - zero) for doubling. See [46] and the appendix of [47] for details on how to calculate d_{eff}.

Fortunately, the phase matching conditions and d_{eff} values of many nonlinear crystals for commonly doubled wavelengths are extensively and clearly tabulated in the literature, [48] is a good example. There is also a free software package available for download called SNLO, which calculates phase matching conditions and simplifies the process of selecting a suitable crystal.[25]

LBO was chosen for our system to frequency double 1104 nm into 552 nm light. It has a modest d_{eff}, but its physical properties are superior to others: it has a high damage threshold $> 10^5 \mathrm{W/cm}^2$ (CW in the IR), $< 0.1\%$/cm absorption, low susceptibility to water and melting point over 800°C. Propagating the fundmental along the X axis with a polarisation in Z and the SH polarised in Y, NCPM is achieved between a temperature of 370 - 380 K ($\sim 100 - 110°$ C). The two waves are coupled with a d_{eff} of 8.5×10 pm/V.

Assuming no depletion of the 1104 nm as it propagates the equation for the single pass efficiency is:

[24] For many crystals certain d_{mn} terms can be shown to be equivalent or zero using symmetry arguments.

[25] SNLO nonlinear optics code available from A. V. Smith, AS - Photonics, Albuquerque, NM.

$$\eta = \frac{P_{2\omega}}{P_\omega} = \frac{2\omega^2 d_{eff}^2 l k_\omega P_\omega}{\pi n^3 \epsilon_0 c^3} h(\xi) \tag{2.18}$$

where $n = 1.604$, ϵ_0 is the vacuum permittivity and P_w and P_{2w} are the fundamental and SH powers respectively. $h(\xi)$ is a function, derived by Boyd and Kleinmann in [47], that for perfect phase matching and no walk - off depends only on the beam focus, where $\xi = l/\omega_0^2 k_w$ and ω_0 is the beam waist. It is used to calculate how best to use a crystal of a given length l for SHG and takes a maximum value of 1.068 when $\xi = 2.084$ and the focus is at the centre of the crystal, [49] has an analytical formula for $h(\xi)$, which is also given in Appendix A. Putting the relevant numbers into eq. 2.18 for a 20 mm long crystal gives an expected SH power of

$$P_{2\omega} = \eta P_\omega = 2.6 \times 10^{-4} P_\omega^2, \tag{2.19}$$

so on a single pass with a 1 W, 1104 nm laser a fraction of a mW could be produced. The fundamental needs to be around the 5 – 100 W level to get the few hundred mWs of 552 nm required . This is done with an enhancement cavity.

2.9.3 Bow - tie doubling cavity

The enhancement factor ϵ_F for a cavity is defined as $\frac{P_C}{P_{in}}$, where P_{in} is the input power and P_C is the power circulating inside the cavity, and is given by:

$$\epsilon_F = \frac{T}{(1 - \sqrt{(1-T)}\sqrt{(1-L)})^2} \tag{2.20}$$

where T is the transmission of the input coupler $M1$ (see fig. 2.17) and L is the loss (including loss in converting to the SH) per round trip of the cavity as a fraction of power. Minimising L and setting $T = L$ maximises ϵ_F. Small L requires: highly reflective mirrors, and minimal scatter and reflection at the crystal surfaces. We use coated mirrors with reflectivity, $r > 99.9\%$ at 1104 nm, manufactured by VLOC and a polished, Brewster cut crystal from Castech.[26] The bow - tie cavity used for our doubling is made up of two flat mirrors and two focussing mirrors between which the crystal sits as shown in fig. 2.17.

The cavity mirrors are mounted a close as possible to the optics table on 12.7 mm mounts. $M1$ has a T of 1% and a diameter of 12.7 mm whereas the three other

[26] LBO also has some absorption of 1104 nm at the 0.1 – 0.3% level. Generally the better the manufacture and growing procedure of the crystal the lower these and losses through scatter will be. Along with cost this limits the length of crystal which is used.

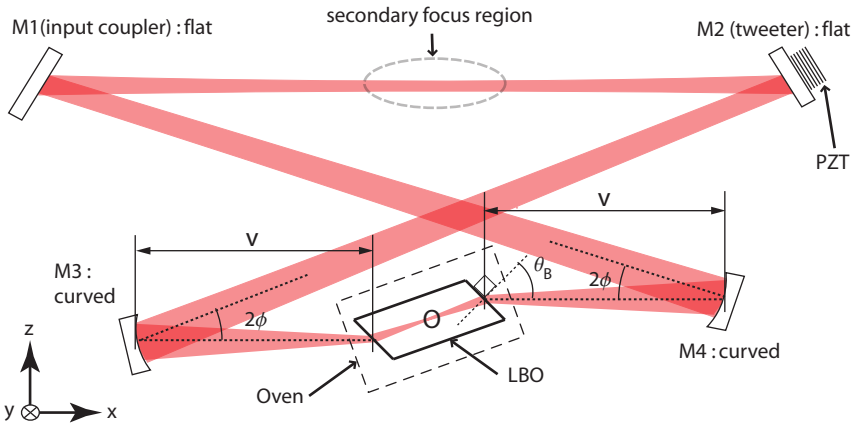

Figure 2.17: *A diagram of the bow - tie cavity. The total distance from $M4$ to $M3$, via $M1$ and $M2$ is defined c_l. The secondary focus occurs $c_l/2$ from $M4$ (and $M3$). O denotes the centre of the crystal and the primary focus. The focal lengths of $M3$ and $M4$ are 50 mm. The Brewster angle $\theta_B = \arctan[n = 1.604] = 58.0°$.*

mirrors are 7.75 mm. By keeping the cavity components small and compact the cavity's sensitivity to temperature drifts in the lab is minimised. To maintain and control the crystal temperature we use an oven supplied by Castech and a heater controller from HPC photonics. The crystal is 20 mm and has a 5×5 mm cross - section.

The cavity design shown in fig. 2.17 is constrained by two factors: 1) the waist of the cavity mode in the crystal should be close to satisfying the condition $\xi = 2.084$ to maximise $h(\xi)$ in eq. 2.18 and 2) the cavity length should be kept as short as possible so that the cavity linewidth is not too small.[27] With this in mind the distance, c_l, between $M4$ (via $M1$ and $M2$) and $M3$ was set to 800 mm, and $M3$ and $M4$ were chosen to have a focal length of 100 mm. This provides a reasonable cavity linewidth and a h value just over 80% of optimum.[28] Mirrors with a smaller focal length would have allowed a shorter cavity and a more favourable waist size, but the resultant beam path would have been obstructed by the oven casing. The angle, ϕ, and distance, v, in fig. 2.17 are found by considering the cavity mode stability and astigmatism. Astigmatism is the difference between the focal positions of the gaussian beam in the *sagittal* plane — this is just the xz plane in the figure and the *tangential* plane — this is the plane that contains the beam and is also perpendicular to the sagittal. The procedure that is used to chose suitable ϕ and v values is now outlined.

A single roundtrip, starting at the centre of the crystal at position O in 2.17,

[27] A short cavity is also less susceptible to vibrations and drifts in temperature.
[28] A 1 m long cavity with a 1 – 2% round trip loss has an linewidth of ∼0.5 – 1 MHz.

can be described by a cavity ray matrix for each plane, where the subscripts s and t denote associations with the sagittal and the tangential planes respectively:

$$M_s = \begin{pmatrix} A_s & B_s \\ C_s & D_s \end{pmatrix} \text{ and } M_t = \begin{pmatrix} A_t & B_t \\ C_t & D_t \end{pmatrix}. \tag{2.21}$$

Because M_s and M_t contain fairly cumbersome terms and do not need to be shown here explicitly to understand the following discussion, the full details are given in appendix A. Matrices for different cavity designs can be found in [50]. The matrix elements are functions of v and ϕ.[29]

For stable cavity mode the following conditions must hold:

$$\begin{aligned} -1 < \frac{A_s(\phi, v) + D_s(\phi, v)}{2} < 1 \\ -1 < \frac{A_t(\phi, v) + D_t(\phi, v)}{2} < 1 \end{aligned} \tag{2.22}$$

where $A_s = D_s$ and $A_t = D_t$ because of the symmetry of our cavity. It is easiest to derive the values of ϕ and v that give $A_s = A_t = 0$, which corresponds to the centre of the stability region. First, we find v_s and v_t in terms of ϕ by solving the equations,

$$A_s(\phi, v_s[\phi]) = 0 \text{ and } A_t(\phi, v_t[\phi]) = 0 \tag{2.23}$$

and then find ϕ so that,

$$v_s[\phi] = v_t[\phi]. \tag{2.24}$$

Using Mathematica to solve these equations we get $\phi = 14.6°(3.s.f)$ and $v_s[14.6°] = v_t[14.6°] = v = 49.3\,\text{mm}$.

To calculate the waist size in each plane at the crystal centre we determine the Gaussian beam parameters q_s and q_t that satisfy:

$$\begin{aligned} q_{s/t} &= \frac{A_{s/t} q_{s/t} + B_{s/t}}{C_{s/t} q_{s/t} + D_{s/t}} \\ &= \frac{B_{s/t}}{C_{s/t} q_{s/t}} \end{aligned} \tag{2.25}$$

where our cavity setup yields $w_s = 54.9\,\mu\text{m}$ and $w_t = 36.7\,\mu\text{m}$.

[29] In general they are also functions of c_l, n and l, but in our case these parameters are fixed.

To efficiently couple light into the cavity the input mode needs to match the cavity mode. The aim is to take the 3.1 μm waist at the output of the fibre and match it to the secondary focus in our cavity, which has a waist of 370 μm. This is done with an 8 mm focal length aspheric fibre collimator, and a telescoping arrangement of two lenses with focal lengths 300 mm and 200 mm as shown in fig. 2.16. Their relative positions are fine tuned by profiling the beam near the secondary focus with a commercial CCD camera.

The cavity only accepts light polarised in the sagittal plane, because the Brewster cut crystal is more reflective for other polarisations. Therefore, we can use the Hansch - Couillaud locking scheme [51] by introducing a small vertical polarisation on the input with a $\lambda/2$ plate to act as a phase reference. To keep the cavity on resonance with the 1104 nm laser the error signal is fed back to the PZT, which is mounted on $M2$. The mass of this mirror was reduced by grinding down its uncoated side to improve the frequency response of the feedback system. The error signal produced when scanning $M2$ is shown in fig. 2.18. An additional feature of

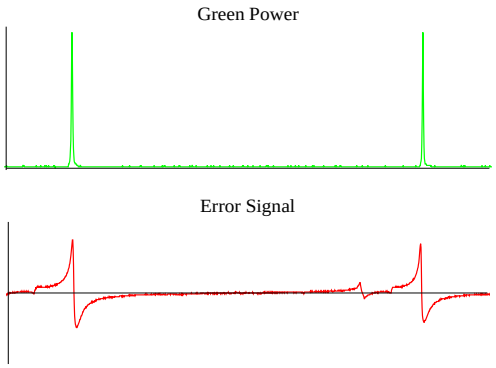

Figure 2.18: *The error and output signal as the cavity PZT is scanned and passes through resonance. The extra features on the error signal are from unwanted cavity modes that have not been extinguished because of imperfect alignment.*

our locking system is that if the piezo voltage driver reaches a predetermined upper or lower limit it automatically resets the output to a mid - ranged value and then attempts to re - lock.[30] This prevents the high voltage supply from pinning, which would result in prolonged periods where the cavity is unlocked and not producing any green light.

The cavity is aligned using the procedure outlined in appendix A. It basically involves systematic adjustment of the coupling and cavity mirrors to maximise the conversion efficiency and to optimise the error signal. After alignment the perfor-

[30] In one complete scan range of the driver we pass through at least two resonances.

mance of the cavity can be measured.

Cavity performance

The noise on the 2nd harmonic intensity when locked is $< 5\%$ and is at a frequency of around 15 kHz. This level of noise is comparable to that seen from our dye laser. Acoustic noise from equipment (and people) in the lab can be troublesome, but our system is isolated from it by placing a sound-proofed box arond the cavity and floating the optics table.

The power relationship between the IR and SH is shown in fig. 2.19. Taking the relationship between the fundamental and the harmonic given in eq. 2.14 we would expect the generated light to increase quadratically with respect to the input. However, this is not the case, we see something closer to $P_{2\omega} \propto P_{\omega}^{1.5}$. This is because the cavity roundtrip loss and hence the enhancement factor changes as P_{ω} is increased; with increasing P_{ω} the conversion losses to the SH become larger. From the figure it can be seen that the 150 mW we require for the interferometer is comfortably achieved. The data above were taken with the crystal oven clamped to

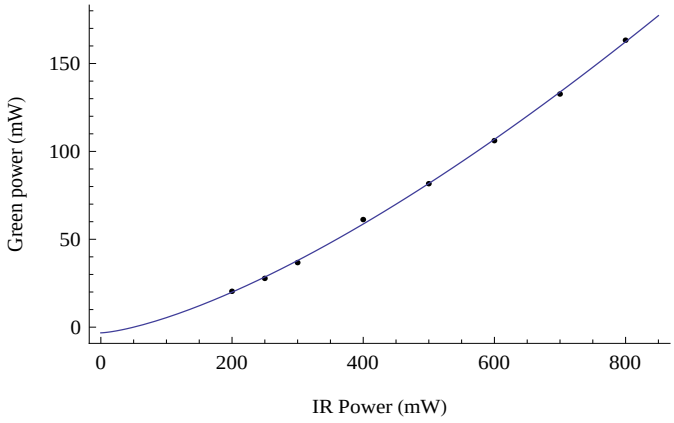

Figure 2.19: *The amount of green light versus pump power when cavity is locked. The IR is measured after the optical isolator which has a transmission of* 95%. *When including the coupling optics a total of* 15% *is lost before entering the cavity. The green is measured after M4 outside the cavity. The maximum conversion efficiency is* 20%

the optics table. An output of 250 mW can be produced, at the cost of long term power stability, by setting the oven up on a 3D translational mount to allow fine adjustments of the crystal position to find *sweet spots* on the LBO input and output faces.[31]. This number can be compared to the theoretical maximum of 320 mW

[31] This problem of stability could be overcome with a more compact oven, which doesn't put as much strain on the mount

calculated using eqs. 2.19 and 2.20 assuming a 1% input coupler and cavity round trip loss of 1%. The discrepancy is largely because the LBO surface and $M4$ reflect at least 20% of the green in total. If more power is required these could be AR coated. Next I summarise the frequency stability and tunability of the fibre laser.

Fibre laser tunability

The Koheras fibre laser can be tuned through 200 GHz by adjusting its fibre temperature. This is done with a built-in temperature controller. The response and settling time is slow ($\sim$ 1 mins), but very linear and repeatable. Fine and fast tuning over a smaller range of 8 Ghz can be achieved by applying a voltage to the fibre PZT. These frequency scans are shown in fig. 2.20.

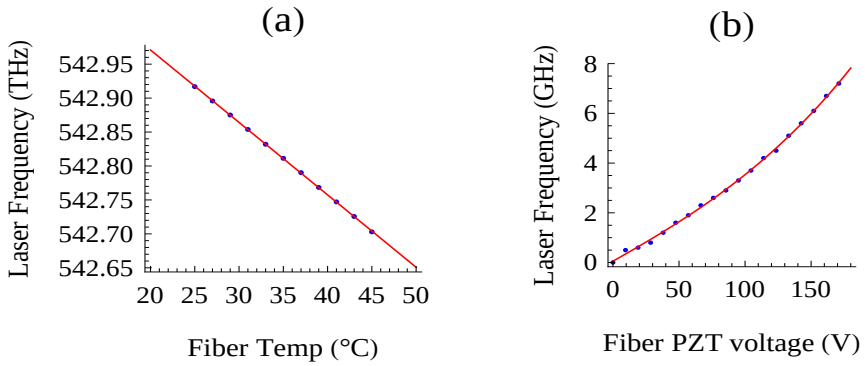

Figure 2.20: *(a) the slow, but broad tuning possible by adjusting the fibre temperature and (b) the fast, fine tuning of frequency with the fibre PZT. The Q(0) transition lies at* 542.810 *MHz, which corresponds to* $35°C$*. There is total a scan range of* 200 *GHz.*

The passive drift of the laser is less than 2 MHz per 15 mins. This slow, small drift and simplicity of tuning means the laser output can be locked to a variety of YbF transitions with relative ease. Coupled with the fact that the system can produce enough green power for at least two days (the mirror mounts creep over this period) without the optics requiring a tweak, makes it ideal for the EDM machine. We propose to use this together with the dye laser system to pump out the X $^2\Sigma^+$ ($\nu = 0, \mathrm{N} = 2$) dark state to increase the number of YbF molecules per shot and thus improve our statistical sensitivity. This second pump laser will act to re-pump the electrons that decay into the dark state under the action of the regular pump beam (see sec 1.6) and will also pump out the thermal population in the state. Assuming similar laser powers in both pump beams and a source temperature of 4 K we should see a factor of 3-4 increase in the signal.

Chapter 3

Experimental method

The basic principle of our EDM experiment (see sec. 1.6) — measuring our interferometer output relative to modulations of B_z and reversals of E_z — remains the same as described in previous theses. Nevertheless, many modifications to the experimental and analysis techniques have been introduced. These have contributed to the automated operation of our machine and allow us to explore possible systematic effects in parallel with the measurement of d_e. In this chapter I discuss the experimental procedure and the methods of analysis we implement.

3.1 Overview

Our most elementary unit of EDM measurement is called a 'block', a sequence of 4096 shots within which each of the machine states are visited an equal number of times. A consecutive collection of blocks is a 'cluster'. Barring any problems with the hardware we usually acquire clusters about 50 – 100 blocks in length (5 – 10 hours of acquisition). Clusters are stopped to carry out a manual reversal of either the E, B or rf cables. These interruptions also provide an opportunity to tune up the dye laser cavity and iodine optics to optimise its output power and stability. Once we have clusters in all eight manual switch configurations we have, effectively, a measurement of the eEDM.

If things look as expected and pass our systematic checks, outlined in sec. 3.3, then more data is acquired to improve the statistical sensitivity, if not an adjustment is made to the experiment based on the results and another dataset or diagnostic data is acquired to investigate. This investigation sometimes involves a 'null' experiment, running the machine in a way where we would anticipate to measure a zero EDM, to test a particular hypothesis. We iterate through this process — uncovering problems[1], diagnosing them and then fixing them — improving our experiment at

[1] Each problem requires a longer integration time to see than the last.

every step. Although this is a rather simplified description, since in practice it is not always viable to work in such a methodical manner, it is essentially how the experiment evolves.

3.2 Taking data

This section details our data taking procedure and starts with defining what we term *waveforms*. Put simply, these govern the parameters that are switched from shot-to-shot during data acquisition, such as E, B_0 and DB. These are not the only parameters we switch. In the explanation of waveforms that follows, however, these three suffice. The additional switches will be discussed in due course. Waveforms were dealt with thoroughly in [29], but they are described here again because there have been slight changes to way we implement them.

3.2.1 Switching waveforms

As illustrated in fig. 1.7 data needs to be taken in eight different machine states to make a measurement of d_e. It has been shown [29, 42, 41] the stray magnetic field noise[2] in our lab is larger at lower frequencies. The YbF source noise is also more pronounced at lower frequencies, though much of its impact is removed by normalising our data with the LIF signal from the pump PMT. Therefore, we should switch between these machine states as often as possible to restrict the amount of low frequency noise that leaks into our measurement. Other noise sources, for example laser frequency/power drifts, are also suppressed by the switching of our parameters. Critically, it is the switching frequency of the E-field that matters when considering magnetic field noise in the EDM signal.

The 14.2 s dead time we have to introduce to carry out an E_z reversal (as explained in sec 2.5.1) means it is impractical to switch it too regularly; a compromise between the effect of low frequency noise and maintaining a reasonable duty cycle has to be made. The settling times for B_z are much shorter (< 5 ms) and it can be modulated without having to introduce any dead time between shots. For this reason B_0 and DB are switched more often than E_z. We use waveforms to define the switching frequencies of our parameters in an efficient and clean way. When running the experiment S_E, S_B and S_{DB} are switched according to particular waveforms.

In essence, a waveform is a list of 0's and 1's. Each bit corresponds to one shot, and its value (0/1) maps to the state (high/low) of the switch that the waveform represents. Our waveforms are not arbitrary strings of binary digits, but are derived from a basis set, using the XOR operator, of square-waves that are defined to start

[2] I will refer to magnetic fields which we do not intentionally apply as stray or background fields.

high, with a period of 2^n bits and length 2^N, where $0 \leq n \leq N-1$. We use $N = 12$ so that our waveforms are 4096 bits (or shots) long.

It is beneficial to use the type of basis set mentioned for many reasons: the generated waveforms can each be represented with a concise N - bit 'wavecode' that clearly indicates which switching frequencies are present in the waveform, all the waveforms are *balanced* (contain as many 0's as 1's), and any two waveforms will be *orthogonal*[3].

To better demonstrate these features I will use a waveform 8 - bits in length, i.e. $N = 3$, as an example. It is simple to extend the ideas for $N > 3$. The waveforms and related wavecodes of an 8 - bit basis set are given below:

Period	Basis waveform	Basis wavecode
2^0	10101010	001
2^1	11001100	010
2^2	11110000	100

Other waveforms can be created from this set with the XOR operator. Let's say we want a waveform that contains both high and medium frequency switching components, we would start with the 011 wavecode, decompose it into the basis and then calculate the resulting waveform as follows:

Wavecode	$\Rightarrow$	Waveform
$011 = 001 \otimes 010$	$\Rightarrow$	$10101010 \otimes 11001100 = 01100110$
011	$\Rightarrow$	01100110

where the waveform generated is balanced and orthogonal to the others. Fig. 3.1 shows possibles waveforms of E, B and DB, which we'll term W_E, W_B and W_{DB}, for an 8 - bit block.

The figure also displays the EDM waveform, W_{EDM}, which is the product $W_E \otimes W_B$. From now on I will drop the XOR operator notation such that $W_E \otimes W_B \Rightarrow W_E \cdot W_B$. This follows from actually saying the word "dot" when we speak about waveforms, rather than using the more awkward "XOR". The signal correlated with W_{EDM} corresponds to the EDM (ignoring any systematic effects).[4] It should be noted that this waveform does not relate to the direction of an individual field as W_E and W_B do, but rather the relative directions of the E and B - fields.

[3] Where the orthogonality of two waveforms can be tested by replacing all the 0's with a -1 and then taking the conventional vector dot product.

[4] Various physical values can be derived by looking at signals associated with other waveforms and their combinations, as will be shown later.

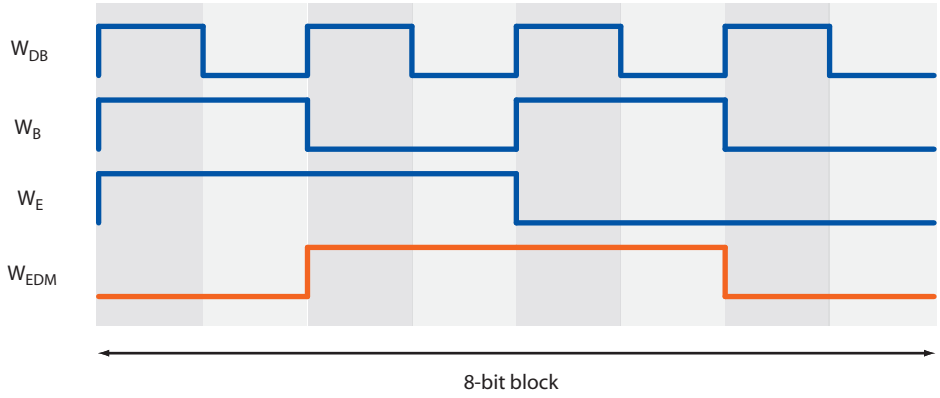

Figure 3.1: *Waveforms for various switched parameters in an 8-bit long block shown in blue. The EDM waveform is shown in orange.*

In general, we refer to the signal, C_W, correlated with a waveform W as a 'channel'. For a block of length 2^N it is calculated as follows,

$$C_W = \frac{1}{2^N} \sum_{i=1}^{2^N} (-1)^{W(i)+1} D(i) \tag{3.1}$$

where $W(i)$ is the value of the waveform at bit position i and $D(i)$ is the signal value at shot i. $D(i)$ is derived by integrating the probe PMT TOF (see fig. 2.5) over a gate in time that picks out the central portion of our cloud. If we are normalising the data, the value is first divided by the integral of the TOF measured by the pump PMT before being entered into eq. 3.1. In practice, we analyse our data over a variety of gates as will be described in sec. 3.3.4.

The method used to estimate the block error of a channel is described here briefly. We first split our 4096 data points up into sets according to machine state and construct a covariance matrix from them. Since a given channel value consists of some linear combination of the set averages we can use the definition of variance for a sum of variables to pick out the relevant elements from the covariance matrix and calculate the uncertainty. This calculation method respects that data from different sets is correlated, but assumes that data within a set is independent. It is employed as a general indicator of how noisy a block was compared to others and is not used in deriving the final error bars on channel values over a whole dataset (see sec. 3.3.2).

In the past W_E, W_B and W_{DB} were fixed from block to block. However, this left us sensitive to noise leaking into our experiment in a systematic way. For this reason, a 'random waveform generator' has been added to our control software. It creates a new set of random wavecodes, and hence waveforms, at the beginning of every block. This prevents specific frequency components of noise leaking into a

channel in the same way every block. The generator also applies the NOT operator on a random selection of the waveforms to invert them ($0 \rightarrow 1$ and $1 \rightarrow 0$), which changes the sign of any contributions from noise so that over many blocks they are averaged to zero. The waveform generator works within certain constraints to maintain a practical duty cycle and keep away from low frequency noise: W_E can only be inverted, it has a fixed wavecode, 111100000000, that switches E relatively infrequently (10 times in a block) and when W_B is created the resulting $W_E \cdot W_B$ must have a fast switching component. In addition, to ensure that the channels are independent, the software checks that all waveforms, inlcuding all the possible dotted combinations, are unique.

As was mentioned earlier in this section, we have to introduce a substantial amount of deadtime when switching E. This would be larger and E would have to be switched less often if we did not implement the technique described next.

3.2.2 Switching E with an overshoot

The charging process of capacitor plates is typically limited by a characteristic time, T_0, as follows:

$$V_C = V_0 \left(1 - e^{t/T_0}\right) \tag{3.2}$$

where T_0 is dependent on the resistance and capacitance of the system, V_C is the voltage drop across the capacitor and V_0 is the supply voltage. We beat this limit when carrying out an E reversal by briefly *overshooting* the HV supply voltages as shown in fig. 3.2. The figure depicts the control signal sent to our negative HV supply when reversing E with respect to time, where our target voltage is 6 kV (1.94 V on the control).[5] The overshoot is defined as a factor of the target voltage, so in this case if a factor of 1.2 was being used then the control during the overshoot period would be set to 1.2×1.94 V.

An optimum overshoot factor of 1.15 was found empirically by taking blocks of what we call Ramsey data. This involved switching only S_E during the block and setting rf1 and rf2 as $\pi/2$ pulses, making our interferometer output signal dependent on the phase difference acquired between $F = 0$ and $F = 1$. The splitting of these hyperfine levels is sensitive, via the Stark effect, to the E field, so by minimising the changes in our signal we could find the most suitable overshoot factor. Ramsey interferometry was discussed in sec. 2.6.1.

[5]The control voltage for the positive supply is not shown, because it has exactly the same features. It only differs in sign and by a few percent in magnitude to account for differences in calibration factors between the HV supplies.

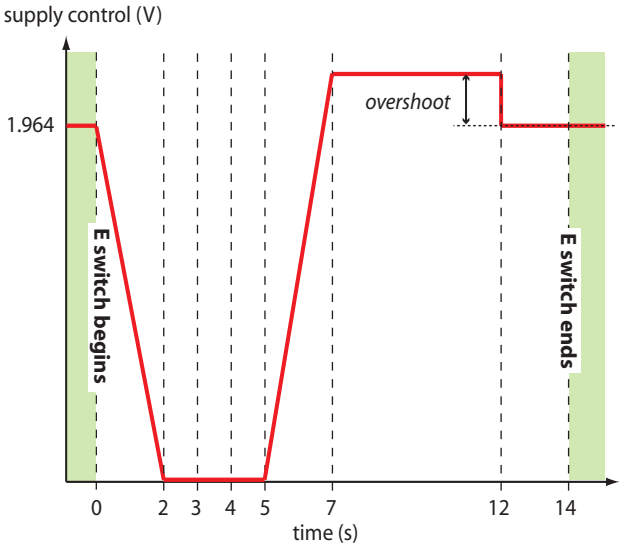

Event	Time (s)
- acquisition stops & switching begins	0
- ramp down	0 - 2
- delay	2 - 3
- bleed switch on	3 - 4
- relay state switches	4
- delay	4 - 5
- ramp up	5 - 7
- overshoot held	7 - 12
- delay	12 - 14
- switching ends & acquisition resumes	14

Figure 3.2: *Overshoot applied in control voltage sent to the negative HV supply during an E switch.*

Fig. 3.3 shows ±6 kV data from two blocks, one without any overshoot in blue, and the other with an overshoot of 1.1 in red. It can be seen in the blue signal that the field varies and takes some time to settle after a switch. However, the red line is flatter because the target voltage is reached much more quickly. In the data taken the length of the interferometer was 660 μs. Therefore, the peak of the Ramsey

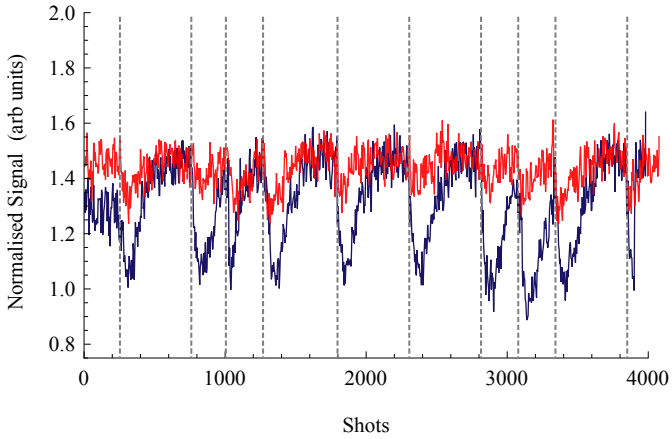

Figure 3.3: *A block of Ramsey data, where the signal is sensitive to changes in the magnitude of E. Blue data taken with a 14 s switch duration without overshoot. Red data with overshoot factor of 1.15. Vertical dashed lines show positions of the E reversals. Note: data is not acquired during an E switch.*

interference curve (a signal of ≈ 1.7 in the figure) is separated from a trough (a signal of ≈ 1) by $\pi/660\,\mu\text{s} = 4760\,\text{rad/s}$ (757 Hz). This corresponds to a field change

of 3.2 V/cm or 1.76 V per plate. So, E is stable to around 1 V/cm (1 part in 10000) during acquisition with the overshoot compared to 2.5 V/cm without.

If we did not use this technique we would have to add 4 – 5 s to each of the 10 E reversals we carry out in a block, resulting in about 10 % less data in a day.

3.2.3 Live block to block analysis

Rather than waiting until the end of a cluster to analyse our data and check that things were working correctly (e.g. checking if the laser was locked throughout) some information is presented 'live' by our control software to the experimenter on a block to block basis.

Before a block has begun the computer measures (via the relevant monitoring devices) and displays the outputs of the HV supplies, the magnitudes of I_{B_0}, I_{DB} and I_{bias}, the rf1/rf2 frequency and amplitude, and the iodine lock AOM frequency. In this way, any obvious problems with the hardware can be seen immediately. The leakage currents, which are sampled every shot are displayed in real - time. This lets us confirm E is actually reversing — indicated by a change in sign of the charging currents after a reversal, and that HV breakdowns are not present — an absence of large currents spikes.

After each block a selection of channel values are calculated (using eq. 3.1) and displayed to the user on scatter plots, giving us an overview of the cluster's general health. These channels are summarised in table 3.1 with their allocated names, associated waveforms and physical relevance. The values are also stated as a combination of the eight points on the interference curve shown in fig. 1.7. The EDM - channel, which will be denoted ***EDM*** from now on, is not displayed because we run blind to it, as will be explained in sec. 4.1.1.

If ***BShift*** (the uncancelled background B - field) is large, data is acquired on nonlinear regions of the interference curve, where the interferometer contrast is reduced and a certain correction, which will be discussed later (see sec. 3.3), we have to apply is pronounced. Therefore, the control software adjusts B_{bias} between blocks such that it is locked to drifting background magnetic fields, using the ***BShift*** value as an error signal for feedback[6]. Its effect can be seen in some example data, fig. 3.4, where there was an initially big ***BShift***. The lock is essential to automated running, as we no longer have to interrupt the experiment every few hours to manually tweak the bias field. The gain is chosen such that we shift B_{bias} an eighth of the measured background field, since stronger feedback can induce oscillations in ***BShift***.

The slope and contrast of our interference curve is represented by ***DB***. This has a close relationship with ***SIG***. We wish to keep ***DB*** as large as possible during data

[6] When deriving the error signal the channel is first divided by ***DB*** as a way of normalising it.

Table 3.1: *Channel values displayed live after each block.*

Channel name	Waveform	Physical relevance
SIG	N/A	Average signal. If this drops in size it indicates something is wrong, e.g., that the laser has unlocked. $= \frac{1}{8}$(A + B + C + D + A' + B' + C' + D')
DB	W_{DB}	Change in signal when B_z's magnitude is modulated. Relates to slope of interferometer and is used as a means of calibrating signals. Represents the general health of the machine. $= \frac{1}{8}$(A − B − C + D + A' − B' − C' + D')
BShift or ***B***	W_B	Dependence of interferometer output on direction of B_z. Indicates the background magnetic field has not been cancelled by B_{bias}. $= \frac{1}{8}$(A + B − C − D + A' + B' − C' − D')
EShift or ***E***	W_E	Change in signal when E is reversed. Evidence that something is wrong with the electric fields. $= \frac{1}{8}$(A + B + C + D − A' − B' − C' − D')

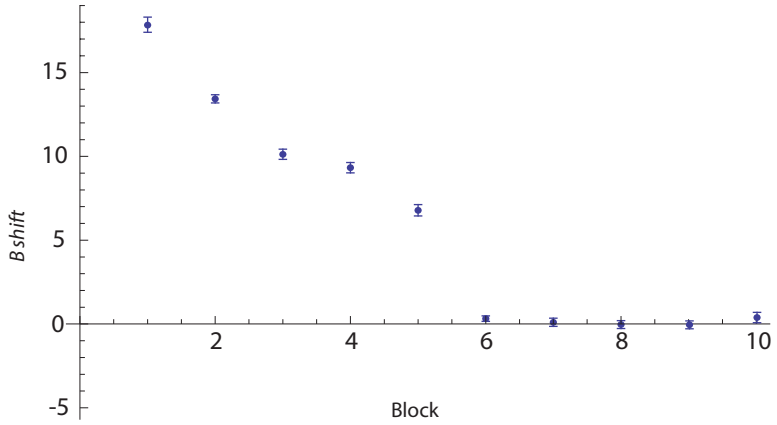

Figure 3.4: *A large initial BShift being removed by the B_{bias} feedback.*

acquisition because our EDM sensitivity is proportional to $\frac{1}{\sqrt{DB}}$. Deterioration of the Yb target is one of the main reasons it can decrease. Therefore, the automatic target stepper (see sec. 2.3) is very important in maintaining a healthy ***DB***, especially during unmanned overnight runs.

One other important number that is also displayed is the fraction, ***DB/SIG***. This tells us if we are getting the most out of the molecules and provides a measure of how well tuned up the experiment is. When things are working well it is about 0.11 – 0.13. Poor alignment of the pump and probe beams through the machine are often the culprit of a small ratio. These are tuned up offline by maximising the TOF signals on the PMTs.

3.2.4 Modulating rf and laser parameters

One way of searching for systematics in a precision measurement is to intentionally change some property of the experiment and see if the outcome is as expected. Since we have such convenient control of the rf and laser parameters we modulate them during data acquisition to do just this.

The frequency and amplitude centres of rf1/rf2 are set with the control voltages V_{RF1F}/V_{RF2F} and V_{RF1A}/V_{RF2A} respectively. We modulate the rf parameters by stepping these values by $\pm\,\Delta V_{RF1F}/\pm\,\Delta V_{RF2F}$ and $\pm\,\Delta V_{RF1A}/\pm\,\Delta V_{RF2A}$ from shot to shot. The same is done for the laser frequency with $V_{LF} \pm \Delta V_{LF}$. As with the other switched quantities each is assigned a waveform labelled W_{RF1F}, W_{RF2F}, W_{RF1A}, W_{RF2A} and W_{LF} from the random generator at the beginning of a block.

The step sizes in terms of a voltage and what they correspond to physically are listed in table 3.2. These step sizes are chosen to be small in comparison to the rf transition linewidths, Rabi curve period and electronic transition linewidths respectively, but large enough such that their effect on the interferometer output signal can be resolved from noise after a block or two of integration.

Table 3.2: *Step sizes of rf and laser parameters.*

Parameter	**Step size (V)**	**Physical step**
$\pm\Delta V_{RF1F}$	± 0.1	± 1.5 kHz
$\pm\Delta V_{RF1A}$	± 0.1	± 0.1 dB
$\pm\Delta V_{RF2F}$	± 0.1	± 1.5 kHz
$\pm\Delta V_{RF2A}$	± 0.1	± 0.1 dB
$\pm\Delta V_{LF}$	± 0.05	± 0.33 MHz

Now we can seek out certain systematics by correlating our data with the modulations in various ways. The most obvious line of investigation would be to see if the EDM we measure depends on the state of any these parameters.[7] For exam-

[7] If things are working as expected then it shouldn't.

ple, to check if the EDM depends on the frequency of rf1, we would calculate the ***EDM.RF1F*** channel (the channel of the $W_{EDM} \cdot W_{RF1F}$ waveform). In fact, we look at all possible channel values when analysing our data to search for anything untoward. More details of this will be given in sec. 3.3.5.

An additional benefit of switching these parameters is that we can lock them using a scheme similar to the one implemented for B_{bias}, as is described next.

rf lock

To maximise ***DB*** the frequencies and amplitudes of rf1 and rf2 need to be tuned such that they are π - pulses (see sec 2.6.1). We do this tuning by using the channel values of the rf parameters dotted with ***DB*** as error signals and feeding back to the control voltages. For example, to adjust the rf1 amplitude we look at the channel value of $W_{RF1A} \cdot W_{DB}$, ***RF1A.DB***, at the end of the block and then shift V_{RF1A} accordingly. ***RF1A.DB*** represents the change in the size of ***DB*** when the rf1 amplitude is stepped. Therefore, when this channel is zero the amplitude is optimised. The lock is shown in action in fig. 3.5. The automated rf locks help suppress the influence

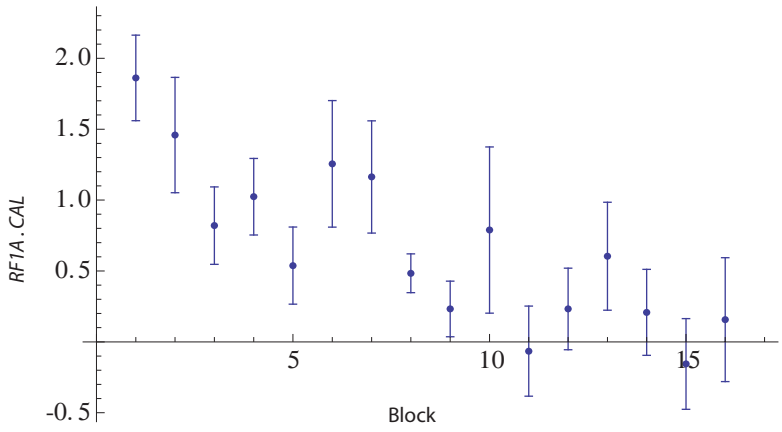

Figure 3.5: *A rf1 amplitude detuning being removed with our locking scheme.*

of drifts in E_z (due to instabilities of HV supply outputs) and the gain of the rf amplifier.

There are some practical factors, however, that prevent us applying perfect π - pulses. Firstly, the molecular packet spans a finite distance in the y - direction when the pulses are fired (about 4.5 cm for rf1 and 6.9 cm for rf2[8]). When combined with the fact that E_z is not uniform along this direction (see fig. 2.13) it is not possible for all the molecules to be simultaneously on resonance with the rf - field. The Stark shift varies across the YbF cloud by 10 kHz. Secondly, the rf transitions are carried

[8] The pulses are 20 μs long, during which the molecules travel around 1 cm.

out in the applied magnetic field, B_z, and because of the Zeeman interaction the $m_F = +1$ and -1 levels of the $F = 1$ state have different resonant frequencies. Under normal operating conditions the splitting is just under 200 Hz, where the rf transition (FWHM) linewidth, dependent on the pulse duration, is $1/20\,\mu\text{s} = 50\,\text{kHz}$. More will be said about these issues and their potential to produce systematic errors in sec. 4.2.

Laser Q(0) $F = 0$ lock

Over the course of a day the angle of the probe laser beam with respect to the molecular beam can change by a small amount, $\Delta\theta$ (in rad), because of drifts in the dye laser cavity and probe optics. Despite the fact that the two beams are nominally perpendicular, deviations in this angle can result in a relatively large Doppler shift given by:

$$\begin{aligned} \Delta f &= \frac{u_{mol}}{\lambda}\,\Delta\theta \\ &= \frac{540\,\text{m/s}}{552\,\text{nm}}\,\Delta\theta \\ &\approx 1000\,\text{MHz}\,\Delta\theta, \end{aligned} \tag{3.3}$$

where u_{mol} is the velocity of the molecular beam and λ is the laser frequency. The FWHM linewidth of the Q(0) ($F = 0$) transition is about 25 MHz so a $\Delta\theta$ of only 1 mrad would result in a substantial relative frequency detuning.

Therefore, we use the LF - channel as an error signal and adjust the iodine lock AOM frequency accordingly to keep the laser on resonance. When the laser frequency is centred on Q(0) ($F = 0$) the LF - channel equals zero. Thus, we use the molecules themselves as the laser frequency reference. It should be noted that one problem with our current setup is that both the pump and probe beams are modulated together, it would be nicer to have independent control of the two.

As part of our live analysis the rf and laser frequency error signals are also listed after each block. This helps us track any unexpected changes in the parameters.

3.2.5 rf phase control

By locking our rf parameters we reduce, but not completely remove, the Ramsey component in our interferometer output.[9] If the E - field magnitude changes when it is reversed the Ramsey component can produce a fake EDM (see sec. 4.2.3). We

[9] Perfect π - pulses would result in a vanishing Ramsey component.

usually refer to this change in the field magnitude as an E asymmetry. Contact potentials on the relay switches would be one mechanism that could result in such an effect.

Since we are unable to apply exact π - pulses, we switch our π-flipper (according to a waveform, W_π) during a block. This averages out the Ramsey component in our signal, turning it into noise. However, because the systematic can potentially be very large (see sec. 4.2.3) we also introduce an arbitrary phase between the rf pulses, which is changed from block to block. We call this phase scrambling.

Phase Scrambling

Before explaining the phase scrambling technique I remind the reader that $0-20\,\text{kHz}$ can be added to the output frequency of the rf synth with a voltage controlled frequency modulator (fm). This is used to set the frequency of rf1, the phase scrambler and rf2 with the control voltages V_{RF1F}, V_{phase} and V_{RF2F} respectively. These result in fm frequencies of ω_{fm1}, ω_p and ω_{fm2}, which have the associated times, t_{fm1}, t_p and t_{fm2} as shown in fig. 3.6, where the separation between rf1 and rf2 is τ. Because

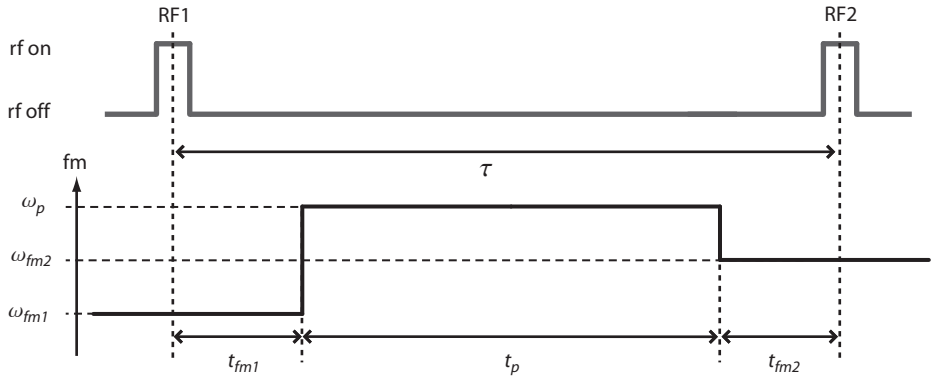

Figure 3.6: *Important definitions for phase scrambling.*

the fm output is phase continuous, we can define the phase between the rf pulses as follows:

$$\phi_{rf} = \omega_{fm1}\, t_{fm1} + \omega_p\, t_p + \omega_{fm2}\, t_{fm2}. \tag{3.4}$$

Therefore, by changing ω_p, we have arbitrary control of the phase difference. Fig 3.7 shows a Ramsey interference scan where the phase was scanned by stepping V_{phase} between shots and $t_p = 500\,\mu\text{s}$. To scramble our phase over a dataset we pick a random V_{phase} between blocks anywhere between $0-0.7248\,\text{V}$, which corresponds to a phase of $0-14\,\pi$ (to 1.5 parts in a 1000).

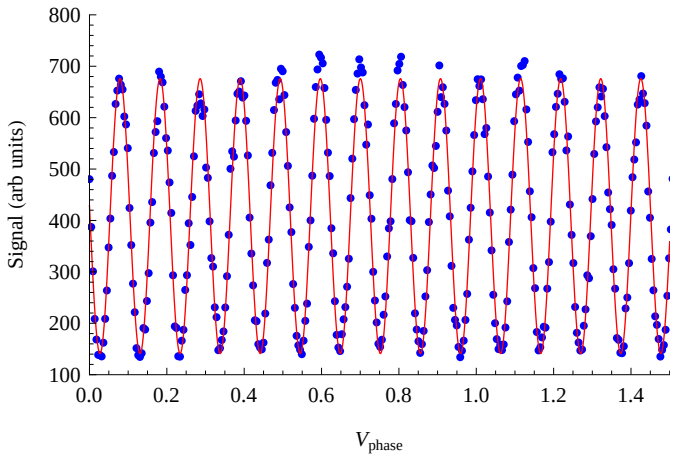

Figure 3.7: *Scanning through Ramsey fringes with our rf phase control, V_{phase}.*

Pump/probe polarisation rotators

Because the pump and probe processes involve driving electronic transitions between states with magnetic sublevels it is important to check whether our interferometer output is affected by the polarisation of the laser beams.

The quantisation axis of our molecules in the pump and probe regions are not expected to change with the reversals of E and B since they are well outside the electric field plates and inner magnetic shields. Therefore, we should not see anything in the EDM channel with respect to polarisation. Nonetheless, the polarisation is rotated independently for each beam between blocks to test this using the setup shown in fig. 2.6. Random, but known, rotation angles lying anywhere between $0-360°$ are chosen. We can then analyse the data looking for any relationships with our signal and the pump/probe beam polarisation angle.

Of course, when rotating the polarisation we may inadvertently be changing the amplitude of the beam entering the machine. For example, the Brewster effect comes into play if the laser beam is not exactly at normal incidence on the laser port window. However, these types of amplitude changes are small compared to the longterm variations of the laser power, which is recorded during acquisition.

3.2.6 Manual reversals

As already mentioned we manually reverse the connections between: 1) the E field plates and HV supplies, 2) the B_z coil and current source and 3) the rf amp and transmission line. These are a powerful diagnostic tool when it comes to understanding and testing correlations we see in our data.

The first two tell us whether something is actually dependent on the direction of the E and B fields or whether it is some artifact associated with the switching

hardware. For example, a non - zero EDM signal due to the magnetic field produced by the HV relay switches would not change sign when the E cables were reversed whereas a real EDM would.[10]

Swapping the rf connections not only reverses the direction of the rf propagation, but also the circular polarisation components of the rf field, as discussed in sec. 2.6. Therefore, we can check to see if the interferometer output is dependent on these properties with the rf manual switch.

According to a lab convection each manual switch is referred to as being in a state, 'True' or 'False', depending on which way round the cables are connected. Each manual switch state is recorded at the beginning of a cluster so we can group our data appropriately when it comes to analysis. Ordinarily one connection is reversed between successive clusters[11] such that overall we have approximately equal amounts of data in each state.

3.3 Data analysis

This section details our analysis methods used to find the value of the EDM, its error and test the data for systematic effects. Unless otherwise stated it should be assumed that we use *normalised* data: each data point attached to a shot is derived by taking the integral of the probe TOF (see fig. 2.5) over a gate $2066-2246\,\mu$s and dividing it by the pump TOF integrated over $\frac{2066}{3.842}-\frac{2246}{3.842}\,\mu$s. The gates correspond to the central portion of the molecular cloud and the factor of 3.842 is the ratio of the distances of the probe and pump PMTs from the Yb target in the y - direction.

Before carrying out a full analysis any blocks that look faulty, such as ones where the laser was unlocked, are discarded. We then have to apply a correction to the EDM of each block, which arises from changes to the amplitude of the interferometer lineshape.

Lineshape correction

Because of the limited way in which we sample the interference curve when taking data (see. 1.7) $\boldsymbol{EDM}$ is dependent not only on the phase shift caused by d_e but also on amplitude changes of the lineshape when E_z and B_z are reversed.[12] Therefore, we are required to account for this by applying a correction to $\boldsymbol{EDM}$ before deriving d_e.

[10] Not all fake EDMs behave like this. See for example the Geometric phase effect, described in sec. 4.2.4.

[11] This usually means a reversal at around 10 am and one in the evening at 7 pm.

[12] For example, if the E reversal is asymmetric the contrast of the interference curve could change when E_z is reversed.

The procedure for finding the correction term is fairly simple. First we make a linear approximation to the lineshape as is shown in fig. 3.8.[13] The output signal,

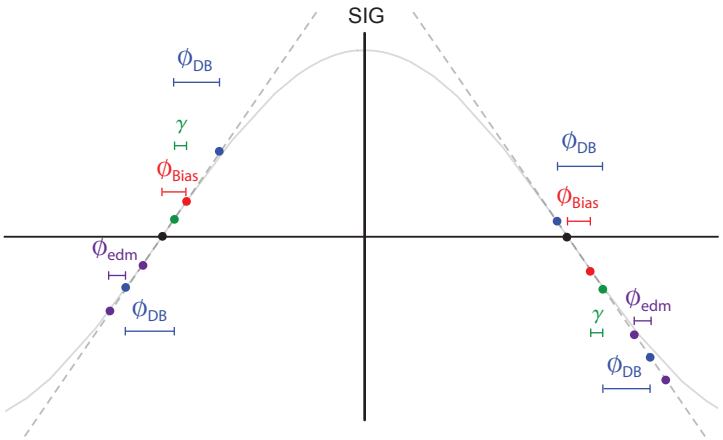

Figure 3.8: *The linear approximation of the* $\cos^2$ *curve and definitions used in deriving the lineshape correction of the EDM channel.* ϕ_{Bias}*: phase due to an uncancelled bias field,* γ*: accounts for an inexact magnitude setting of the B step (if set perfectly* $\pm B$ *provides a phase step of* $\pm\pi/4$ *and* $\gamma = 0$*),* ϕ_{DB}*: due to the DB step and* ϕ_{edm}*: represents the phase shift caused by a real EDM.*

SIG, as a function of the various phases defined in the figure and the switch states of E, B and DB represented by S_E, S_B and S_{DB}, which take values of ± 1, is then:

$$SIG\left[S_E, S_B, S_{DB}\right] = -\left(\phi_{Bias} \cdot S_B + \gamma + \phi_{DB} \cdot S_{DB} + \phi_{edm} \cdot S_E \cdot S_B\right) \tag{3.5}$$

where a one - to - one relationship between the phase and signal has been used. Eq. 3.5 can be generalised so that it has an arbitrary dependence on S_E and S_B,

$$SIG = -(1+a\cdot S_E+b\cdot S_B+c\cdot S_E\cdot S_B)\left(\phi_{Bias} \cdot S_B + \gamma + \phi_{DB} \cdot S_{DB} + \phi_{edm} \cdot S_E \cdot S_B\right). \tag{3.6}$$

Using this definition of SIG the EDM channel equates to,

[13] This approximation is not neccessary it just makes the derivation of the correction slightly clearer. In fact, the correction holds for any function aslong the functional form does not change when E or B are switched.

$$\begin{aligned}\boldsymbol{EDM} &= \frac{1}{8}\left(SIG[1,1,1]+SIG[1,1,-1]+SIG[-1,-1,1]+SIG[-1,-1,-1]\right.\\ &\quad \left.-SIG[1,-1,1]-SIG[1,-1,-1]-SIG[-1,1,1]-SIG[-1,1,-1]\right)\\ &= -(c\gamma + a\phi_{Bias} + \phi_{edm})\end{aligned} \tag{3.7}$$

where it can be seen that there is a non - edm term, $-(c\gamma + a\phi_{Bias})$, in the channel. This is the term we need to correct for. a and c can be evaluated from the other channel values listed below in eq 3.8. Rather than assigning a name to each as I did in table 3.1 I use the form $C_{\{x\}}$ to label the channels so that the switches the channel depends on are in the parenthesis. For example, ***BShift***, which corresponds to the signal correlated to the switching of B, and ***EDM***, to the combination of the E and B switches, would be labelled C_B and $C_{E\cdot B}$ respectively.

$$\begin{aligned}C_{\{E\}} &= -a\,\gamma - c\,\phi_{Bias} - b\,\phi_{edm}\\ C_{\{B\}} &= -b\,\gamma - \phi_{Bias} - a\,\phi_{edm}\\ C_{\{DB\}} &= -\phi_{DB}\\ C_{\{E\cdot DB\}} &= -a\,\phi_{DB}\\ C_{\{B\cdot DB\}} &= -b\,\phi_{DB}\\ C_{\{E\cdot B\cdot DB\}} &= -c\,\phi_{DB}.\end{aligned} \tag{3.8}$$

By re - arranging these and substituting into eq. 3.7 we get the corrected EDM channel,

$$\boldsymbol{EDM^{corr}} = \frac{1}{1-\left(\frac{C_{\{E\cdot DB\}}}{C_{\{DB\}}}\right)^2}\left[C_{E\cdot B} - \frac{C_{\{E\cdot DB\}}C_{\{B\}}}{C_{\{DB\}}} + \frac{\gamma}{\phi_{DB}}\left(\frac{C_{\{E\cdot DB\}}C_{\{B\cdot DB\}}}{C_{\{DB\}}} - C_{\{E\cdot B\cdot DB\}}\right)\right] \tag{3.9}$$

where the ratio $\frac{\gamma}{\phi_{DB}}$ can be measured offline by scanning the interference curve. For example, if we find I_{B_0} as defined in eq. 2.1 is set too large by $10\,\mu$A and a $I_{DB} = 100\,\mu$A is being used then $\frac{\gamma}{\phi_{DB}} = \frac{10}{100}$. In practice, we set I_{B_0} well enough so

that $\frac{\gamma}{\phi_{DB}} < 0.05$ and consequently the contribution from the last term in eq. 3.9 is negligible.

In reality, there will not be a simple one - to - one relationship between the change in our PMT signal and the change in phase as was assumed here. The next section describes how we take the corrected EDM channel, as defined in eq. 3.9, from each block and convert it into an actual EDM value, d_e. From here on I will drop the superscript on $\boldsymbol{EDM^{corr}}$ and it should be assumed that $\boldsymbol{EDM}$ refers to the corrected channel value. If a distinction is required it will be stated.

3.3.1 EDM in physical units

$\boldsymbol{DB}$ is the change in signal when the known magnetic field, DB, is stepped. Therefore, we can use it as a calibration factor to derive what d_e is represented by the EDM - channel value for each block as follows,

$$\frac{\eta\, d_e\, E_{eff}}{\mu_B\, DB} \;=\; \frac{\boldsymbol{EDM}}{\boldsymbol{DB}} \cdot M_s \tag{3.10}$$

where M_s is a function that 'signs' the data depending on the manual state of the E and B cables. It equals +1 when both were in state True or False, and -1 when only one was in state True or False when the block was acquired. We do not sign with the rf manual state because a real EDM is independent of this. After re - arranging eq. 3.10 we get a value in physical units:

$$d_e \;=\; \frac{\boldsymbol{EDM}}{\boldsymbol{DB}} \times \frac{\mu_B\, DB}{\eta\, E_{eff}} \tag{3.11}$$

where DB is typically set to 1.7 nT and η depends on the plate voltages. We can then derive the mean and error of the EDM dataset.

3.3.2 EDM mean and error

Before calculating a final result we inspect the distribution of the data. Generally, things look very Gaussian - like, except for a few outliers. This characteristic is seen more clearly in fig. 3.9, a quantile - quantile plot, as a deviation from the $x = y$ line. The data is from a large null test[14] containing over 7000 blocks, which will be discussed in sec. 4. A possible explanation for the outliers could be that they belonged to blocks that were especially noisy. So by weighting the data by the EDM error of each block we should be able to 'pull' them in. However, we find that this is

[14] Control experiments where we intentionally configure the apparatus so that we expect to register a zero eEDM.

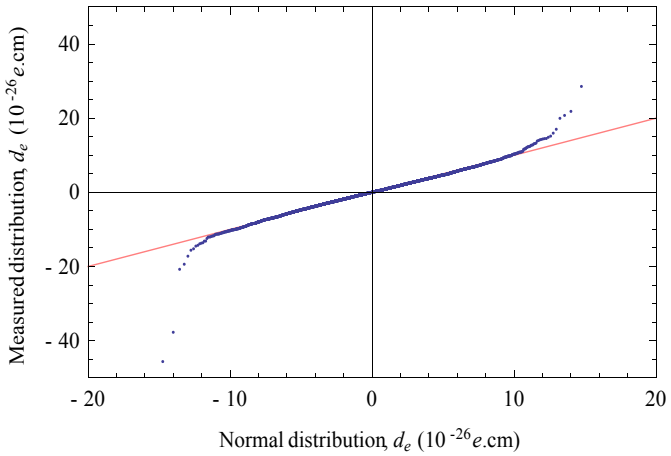

Figure 3.9: *A Q - Q plot comparing the measured EDM distribution to a normal distribution. This plot makes clear the presence of the outliers.*

not the case. In fact, the EDM uncertainty estimates from block to block are fairly constant. This indicates that the noise seen by a block is different to that seen by many blocks.[15]

Considering that the distribution contains these outliers it is unsafe to derive a final mean, $\overline{EDM}$, and error, $\pm\sigma_{EDM}$, assuming purely Gaussian statistics. Instead, we use a trimmed mean technique that is robust to the effect of the outliers.[16] The implementation is described below.

Trimmed means and bootstrapping

Let's say there are N EDM data points in our dataset, we draw from it N times with replacement.[17] This creates a new synthetic dataset, which is equal in size to the original dataset. The process is then repeated M times (in our case usually 5000) so that we are left with M samples each of length N. We then calculate the trimmed mean of each of the datasets, where the upper and lower 1 % of the values are removed. Next a cumulative distribution function (CDF) of these trimmed means is generated. If we want the 68 % confidence interval we find the EDM values, EDM^- and EDM^+, which correspond to the CDF when it equals $0.16 = 0.5 - \frac{0.68}{2}$ and $0.84 = 0.5 + \frac{0.68}{2}$ respectively. The final bootstrapped result for the mean and error is then given by:

$$\overline{EDM} = \frac{EDM^+ + EDM^-}{2} \qquad \sigma_{EDM} = \frac{EDM^+ - EDM^-}{2}. \tag{3.12}$$

[15] This tallies up with our noise spectrum not having a flat power spectrum.
[16] Which we argue are caused by fluke occurrences, drop outs in laser power, electrical spikes etc.
[17] Meaning that we are allowed to pick the same point more than once.

This can be done for any choice of confidence interval. This numerical method of creating many synthetic samples to evaluate the uncertainty is known as bootstrapping. In our case, it means we do not have to assume a particular function of the underlying distribution of our data, except that it has a single peak.

3.3.3 Probing for systematic effects

The data is then tested empirically for evidence of systematic effects.

3.3.4 Analysing the EDM versus arrival time

The temporal width of the TOF recorded by the probe PMT corresponds to the spatial spread of the molecular cloud as it passes through the probe laser beam.[18] A good approximation is to say that the cloud began as a point source and that the spatial spread originates solely from the velocity distribution of the YbF, where earlier times on the TOF correspond to faster moving molecules.

Therefore, molecules of specific velocity classes will have been in particular positions when rf1 and rf2 were administered and also traversed distinct regions between the time they were fired. This means that the impact of the inhomogeneous magnetic and electric fields on our measured EDM can be tested by moving the position of the gate that we integrate the TOF over. A real EDM would be independent of the choice of gate. To test this data is analysed over three gates, referred to as the *fast*, *slow* and, the previously defined, *central* gates. The fast (slow) gates for the probe and pump are $2065-2155\,\mu$s ($2156-2246\,\mu$s) and $\frac{2065}{3.842}-\frac{2155}{3.842}\,\mu$s ($\frac{2156}{3.842}-\frac{2246}{3.842}\,\mu$s), shown in fig. 3.10 as the red (green) regions. The central gate, which contains both the fast and slow gates, is also shown in the figure.

If we see something interesting then we can delve a bit deeper and split the TOF into smaller sections.

3.3.5 Non-zero channel finder

The EDM is not the only interesting value to look at. In fact, we apply an analysis similar to the above to all possible channels, i.e., the channels corresponding to all possible undotted and dotted combinations of the 9 switching waveforms — W_E, W_B, W_{DB}, W_π, W_{RF1F}, W_{RF2F}, W_{RF1A}, W_{RF2A} and W_{LF}. Including *SIG* this gives a total of $2^9 = 512$ channels. Rather than displaying all of them, any channels that have a mean to error ratio larger than a threshold we chose (typically 3) are

[18] The profile of the probe laser in the y-direction ($\sim 0.5\,$cm) also adds to this width by a small amount.

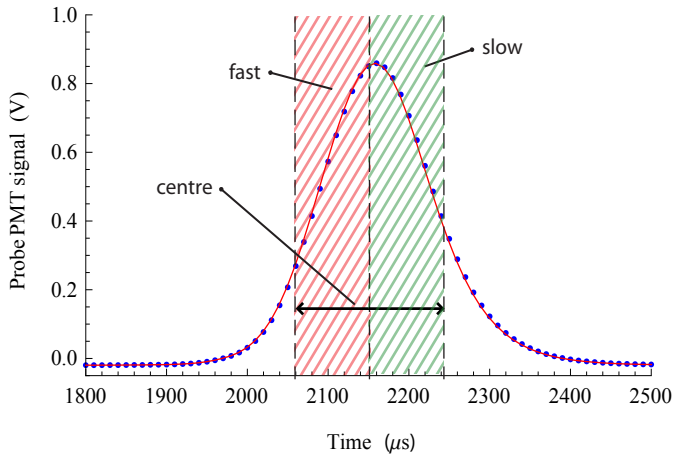

Figure 3.10: *A TOF overlaid with the various analysis gate regions.*

considered to be 'non - zero' and tabulated by the analysis software. The non - zero channel finder is also run on data that has first been separated according to manual state. On inspection of the tables we should be able to provide a physical explanation for the channels we see and their behaviour with respect to the manual state of the machine. Channels dotted with W_E, W_B and $W_E \cdot W_B$ are particularly interesting, because they are closely related to the EDM.

Analysing all analog inputs

So far I have only considered the normalised data from the probe PMT. However, we can search for non - zero values in the other analog inputs. The battery and 10 kΩ short, our *null* tests of the analog acquisition card, should not be correlated with any of the switched parameters. Unnormalised probe PMT data should give the same results as the normalised. The pump PMT should be sensitive to solely the laser frequency stepping waveform, W_{LF}. Probably the most interesting inputs are the magnetometers. If any detect a magnetic field that switches with E then we could have a fake EDM. A switching field of around 0.1 nT outside the two magnetic shields would correspond to an EDM of $5 \times 10^{-28}\, e$.cm.

As of yet we have not found any worrisome non - zero channels in any of our analog inputs when analysing our data (see sec 4.1.3).

Chapter 4

Results and systematics

During my PhD I have not made an EDM measurement. Nevertheless, a large *null* dataset, where everything except the E switch was enabled, has been taken with a sensitivity that is a factor of two better than the Tl experiment. What we have from this dataset is a benchmark with which to compare subsequent data where the E-field is switching. Any new effects we see must be associated with physical processes that depend on the switching of the relays, the direction of the electric field or any asymmetries in magnitude introduced by the field reversal. In addition, the act of taking such a large amount of data focused our attention on identifying, characterising and quantifying various systematic effects. A major part of this involved the design and implementation of some important diagnostics experiments that let us empirically measure the size of the systematics, rather than relying solely on theoretical models. To provide a context for these, their results are incorporated in the discussion of the null data set, which is the focus of this chapter. At the end of the chapter I briefly deal with the sources of noise that are relevant to the experiment.

4.1 Null dataset

Once the experiment was in a state where it could run without too much human intervention an EDM measurement was started. After 3 months of acquisition it was realised that the optic fibre controlling the switching of the HV relays had failed very early on in the dataset and hence, the E direction was not actually reversing except when a manual reversal was applied. This problem was left undetected for such a long period because at the time leakage currents were not displayed in real-time, as explained in sec. 3.2.3, or actively looked at very often on analysis. Moreover, E reversals do not show up in the channel values because none of them, except ***EDM*** (if d_e is non-zero), are actually expected to depend on the direction of E. This data,

where the E - field was not switching, makes up what I refer to as the null dataset.

The null dataset consists of 7380 blocks taken at $\pm 11.7\,\mathrm{kV/cm}$. 1440 blocks were also taken at $\pm 3.3\,\mathrm{kV/cm}$ for diagnostic purposes.

4.1.1 Overview

The null dataset has proven to be extremely useful. We have been able to assess the reliability of the experiment over a very large duration of time. Apart from the failure of the relay switch optical link nothing of major significance went wrong with the apparatus throughout the whole 3 months and the experiment typically ran continuously 7 days and nights a week without too much effort. Also the analysis procedure has been streamlined and honed with new techniques, such as the non - zero channel finder. A complete analysis of the 20 GB dataset can comfortably be carried out on a regular desktop computer.

With regard to results, it is very satisfying that the final *null* EDM, d_e^{null}, is consistent with zero, there is nothing unusual when the data is analysed for different arrival times (sec. 3.3.4) or versus the E, B and rf manual states, all 512 channels analysed by the non - zero channel finder have values that agree with our physical understanding of the experiment and the systematic effects that have been investigated are shown to be at a safe, non - problematic level. When discussing these results in more detail I will follow what may appear a slightly backwards order. The non - zero channel finder and systematics will be dealt with first (see sec. 4.1.3 and 4.2), and the null EDM result will be given at the end (sec. 4.3). This is because we implemented a method, often used in particle physics experiments (e.g. [52, 53, 54]), called *blind* analysis.

Blind analysis

Blind analysis involves hiding the final result from the experimenters until the experiment and analysis is fully complete to prevent it being biased by their preconceived notions [55]. Blind analysis is used by experimenters not because they consider themselves corruptible or dishonest, but because they want to remove any possibility of unconsciously affecting their final result. This is particularly important for precision measurements, where after evaluating systematic effects corrections are often applied to the final result. A statement made by F. G. Dunnington in a 1932 paper [52], describing his blinded charge to mass ratio measurement of the electron, sums this up well:

"It is easier than is generally realized to unconsciously work towards a certain value. One cannot, of course, alter or change natural phenomena [...], but one can, for

instance, seek for corrections and refinements which shift the results in the desired direction."

Our final result was hidden by the analysis software which added an unknown, but constant, offset to the EDM value.[1] Only once we were satisfied with the experimental procedure and our understanding of systematic effects was the offset removed to unveil the actual result. More information can be found on the subject of blind analysis in [56].

Although we were blind to the actual value of the EDM, we could still search for any irregularities in the blinded EDM as we took data. This is discussed next, before moving on to the results of the non-zero channel finder.

4.1.2 Blinded eEDM analysis

During data acquisition we frequently looked at the (blinded) EDMs found in each manual state for the fast, central and slow analysis gates (see fig. 3.10). This would tell us if there was some problem with the experiment or indicate the presence of a systematic effect. It should be a noted that the same blind was applied to the data irrespective of the gate. The EDM values from the dataset broken down by the various analysis gates and manual states are given in table 4.1. Each manual state contains roughly the same amount of data and EDMs are calculated using the method described in sec. 3.3.2.

Looking down the table there are no major discrepancies in the EDM values and errors between manual states. One of the important things this indicates is that the E, B, and rf hardware is working properly. For example, a problem in the rf transmission line, a faulty rf cable or failed capacitor, could cause one manual rf state to produce different results than the other. The fact that the values with respect to the manual E state are consistent with each other implies there is no large fake EDM induced by the electrical-to-optical circuitry that is used to control the switching of the HV relay supply. One possible EDM inducing mechanism would be a magnetic field, generated by the circuitry, that changes when S_E is switched.[2]

The EDM versus the time of arrival at the probe PMT, as explained in sec. 3.3.4, is displayed across the table. It is apparent that the choice of gate does not affect the central value. However, the errors are larger for the fast and slow gates. This is what you would expect, because there are fewer molecules detected in these gates.

[1] This offset was a random number of the order $10^{-27} - 10^{-26}$ e.cm generated by the analysis software before we started acquiring data.

[2] Though such types of effects are averaged out by the manual E reversals, if the fake EDM is large enough it can leak through into the final result. Only in the limit of taking an infinite amount of data do the contributions average exactly to zero.

Table 4.1: *Blinded EDMs in units of* 10^{-27} *e.cm broken down by manual state and analysed for various gates in time. The same blind is applied to all EDM values. The actual value of the blind is given in sec. 4.3.*

Manual state			**Analysis gate**		
E	B	rf	fast	central	slow
T	T	T	5.0 ± 1.8	4.8 ± 1.4	4.4 ± 1.7
T	T	F	3.6 ± 3.1	3.6 ± 3.2	3.9 ± 1.5
T	F	T	4.4 ± 1.5	4.8 ± 1.1	5.4 ± 1.1
T	F	F	1.8 ± 2.6	1.4 ± 2.3	1.3 ± 3.8
F	T	T	1.9 ± 3.5	1.9 ± 3.0	1.6 ± 2
F	T	F	1.2 ± 2.3	1.4 ± 1.6	1.6 ± 1.7
F	F	T	2.6 ± 1.7	2.0 ± 1.2	2.0 ± 1.3
F	F	F	5.4 ± 2.1	5.3 ± 1.5	5.2 ± 1.6
Overall EDM:			3.21 ± 0.63	3.25 ± 0.47	3.27 ± 0.5

When a dataset with a reversing E is taken it will be particularly useful to compare it with table 4.1 to check to see if any new features are seen. If no systematic effects are "turned on" by the switching of the E - field then things should generally look the same.

We can also look at the EDM from the unnormalised data which is given in table 4.2 along with the normalised data for comparison. There does not appear to be any major difference between the mean values, which demonstrates that the act of normalising the data does not pull the final result about. Nonetheless, the error bar is reduced after normalisation, indicating source noise is significant. Other noise sources will be dealt with in more detail in sec. 4.4.

Table 4.2: *EDM values of unnormalised and normalised data (*10^{-27} *e.cm).*

	Analysis gate		
	fast	central	slow
Unnormalised	3.164 ± 0.735	3.186 ± 0.570	3.181 ± 0.61
Normalised	3.205 ± 0.625	3.250 ± 0.465	3.273 ± 0.500

Prior to examining specific systematic errors I give the results of the non - zero channel finder.

4.1.3 Non - zero channel finder

Of all the 512 channels we analyse only 12 are non - zero — defined here as channels that have a mean to error ratio larger than 3. These are displayed in table 4.3. The channels were evaluated for normalised data *not* weighted by manual state. It should be noted that "dotted" channels in the table are defined as explained in sec. 3.2.1, so for example, ***LF.DB*** is not the product of the ***LF*** and ***DB*** channels, but the channel value of the waveform, $W_{LF} \cdot W_{DB} = W_{LF} \otimes W_{DB}$.

Table 4.3: *Non - zero channels in normalised data not weighted by manual state. Channels are ranked by the ratio of their magnitude their uncertainty.*

Channel	**Mean value and error**	**mean/error**
DB	9.43 ± 0.05	203
LF	0.608 ± 0.004	166
SIG	69.4 ± 0.5	144
LF.DB	$4.40 \pm 0.08 \times 10^{-2}$	51.9
RF1F.RF2F	$-4.13 \pm 0.09 \times 10^{-2}$	45.6
π***.RF2A***	$-3.86 \pm 0.12 \times 10^{-2}$	33.6
RF1F	$6.09 \pm 0.28 \times 10^{-2}$	21.8
RF2A	$-2.29 \pm 0.18 \times 10^{-2}$	12.4
π***.RF2A.DB***	$-0.878 \pm 0.080 \times 10^{-2}$	11
RF1A	$-1.73 \pm 0.17 \times 10^{-2}$	10.3
RF2F.DB	$0.535 \pm 0.097 \times 10^{-2}$	5.51
RF1F.DB	$0.402 \pm 0.100 \times 10^{-2}$	4.02
All other channels	N/A	< 3

Explanation of non - zero channels

SIG (the average LIF signal) and ***DB*** (the slope of the interference curve) are both channels that should be non - zero.

LF: the change in signal when the laser frequency is stepped. As mentioned in the description of the laser lock (see sec. 3.2.4) the pump and probe beams are not stepped independently. The frequency difference between the two depends on: 1) the setting of the VCO that drives the pump AOM[3] and 2) any Doppler shifts (given by

[3]This was set at the beginning of the dataset and not re - adjusted thereafter.

eq. 3.3) we inadvertently introduce through misalignments of the two beams. During data acquisition the laser lock derives its error signal from unnormalised probe PMT data and consequently, when we look at the value of ***LF*** in the unnormalised data it is consistent with zero, i.e., the pump beam was on resonance on average during the dataset. However, the ***LF*** channel is non-zero in the pump PMT signal and corresponds to an average pump laser detuning of 1.5 MHz. It is this detuning on the pump that results in a non-zero ***LF*** channel in the normalised data.

Because the pump laser is slightly off-resonance, when its frequency is stepped the amount of molecules driven into the $F = 1$ state during the pump phase of the experiment changes, and in turn so does the interferometer contrast. Hence, the ***LF.DB*** channel, which is the change in the interferometer contrast when the laser frequency is stepped, is non-zero. Since the rf parameters also effect the interferometer contrast in much the same way — a detuning results in a reduced contrast — I now consider dotted channels of the type ***x.DB*** together.

RF1F, ***RF1F.DB*** and ***RF2F.DB***[4]: represent the detuning of the rf frequencies. The channel values are consistent with rf1 and rf2 being red-detuned by about 100 Hz each on average, which is relatively small compared to the 50 kHz FWHM of the transition.

When we stop the experiment to carry out maintenance — a dye change, YAG flash lamp change etc. — we turn off the HV supplies (primarily for safety reasons). After restarting data acquisition the supplies drift around before stabilising, which can be seen in the often larger ***RF1F*** and ***RF2F*** channel values at the beginning of clusters. If the output of the live analysis shows particularly large detunings we sometimes give the lock a helping hand by manually adjusting V_{RF1F} and V_{RF2F}. When considering this, combined with the drifts of the HV supplies, the 100 Hz detunings we see are reasonable.

RF1F.RF2F: this measures the correlation between the detunings of rf1 and rf2. The sign of the channel indicates that the correlation is positive, i.e. when rf1 is red/blue detuned rf2 is also red/blue detuned. This is the behaviour that would be expected as a result of slow drifts (over the duration of a few blocks) of the HV supply outputs, since any detunings induced by these are common to both rf pulses.

π***.RF2A***/π***.RF2A.CAL***: shows that there is an imperfection in the π-flipper, in that not only does it modulate the relative phase of the rf the pulses but also

[4] At the levels of noise we are working at, the fact that ***RF2F*** does not appear in table 4.3 is not significant.

the amplitude of rf2. This feature, which we were unaware of before the dataset was acquired, was confirmed in offline tests of the π - flipper hardware. In itself the amplitude modulation can not cause Ramsey effects to leak into our EDM measurement, especially when taking into account that we also implement the phase scrambling technique described in sec. 3.2.5.

RF1A / ***RF2A***: the change in signal when the rf amplitude is stepped. These channels indicate the amplitudes are on average both high by about 2 % of the optimum. Like the rf frequency channels these typically have bigger magnitudes at the beginning of clusters. This is most probably because when data acquisition is stopped the rf amplifier is not active and therefore drifts once the experiment is restarted before settling down.

When the data is weighted by the manual E and B states, as we do to derive an EDM, we see that all the channels are zero. The other analog inputs give the expected results: the *Bartington* magnetometer detects the B_0 and DB steps in data weighted by the manual B state, no magnetic field is detected to switch with E in any of the magnetometers (we have three mini - fluxgates positioned around the lab in addition to the *Bartington*), and the null analog inputs, the 9 V battery and 10 KΩ short, are not correlated with any of the switched parameters.

It is pleasing that the channels we see are simply explained and behave as expected. Moreover, they do not indicate any physical mechanisms that could produce a fake EDM.

The results discussed so far do not indicate the presence of any systematic effects. The next section deals with the investigation of specific systematic effects that would not necessarily show up in the blinded EDM analysis or non - zero channel finder.

4.2 Systematics

In this section I go through specific systematic effects that we have investigated either practically, through experiment, or theoretically, with mathematical models. I discuss what physical parameters each depends on and quantify the potential size of the fake EDMs they could produce. For the majority of effects, this is the first time this has been done. A total error, incorporating all the systematics, is given at the end.

4.2.1 $F = 1$ systematic

To read out the population in the $F = 0$ state during the probe phase of the experiment we drive the Q(0) ($F = 0$) transition and measure the resulting fluorescence. Because the Q(0) ($F = 1$) transition has a non-negligible linewidth, we also inevitably drive molecules out of the $F = 1$ state. In itself, this is not a problem, but it was argued that if there is any large systematic associated with probing the $F = 1$ level then a fraction, R_{sys}, of it would leak into our probe signal. The first step in evaluating the potential size of the systematic was to estimate R_{sys}, which involved measuring the Q(0) ($F = 1$) linewidth. To do this we blocked the pump beam and scanned the dye laser over the Q(0) ($F = 1$) transition. Simultaneously, we recorded the laser transmission signal through a 150 MHz reference cavity to give us a means of calibrating the frequency axis. This data is shown in fig. 4.1, where the laser power was set to a value similar to that used when we take EDM data, ≈ 1.5 mW. The power setting was important because there is a dependence of the linewidth on beam intensity, due to power broadening. A double Lorentzian is fitted to the data to account for the nearby Q(0) ($F = 0$) transition, which is just out of the scan range to the right of the main peak. The scan was repeated 5 times and

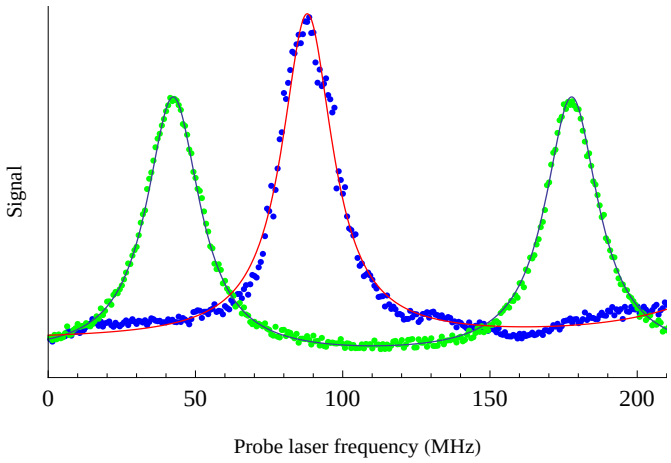

Figure 4.1: *Blue points are the laser induced fluorescence spectrum of the Q(0) ($F = 1$) transition; a double (to accommodate the neighbouring Q(0) ($F = 0$) transition) Lorentzian fit to the data is shown in red. Green points are the transmission from a 150 MHz (free spectral range) reference cavity; an Airy function fit is shown in dark blue. The laser power was $\approx 1.5\,mW$*

the FWHM, $\Gamma_{F=1}$, was found to be 29.6 ± 0.4 MHz.

During normal data acquisition the probe laser is 170.25 MHz blue detuned from Q(0) ($F = 1$). At this level of detuning and taking the upper limit of $\Gamma_{F=1}$, 30 MHz, the fluorescence signal from the transition as a fraction, ϵ, of the maximum (on

resonance value) is:

$$\begin{aligned} \epsilon &= \frac{(\Gamma_{F=1}/2)^2}{\Delta f^2 + (\Gamma_{F=1}/2)^2} \\ &= 7.70 \times 10^{-3}\,(3.\,s.\,f.) \approx \frac{1}{130} \end{aligned} \tag{4.1}$$

where Δf is the detuning, and the function on the right hand side is a normalised Lorentzian. On average, when driving the Q(0) $(F = 1)$ transition in comparison to Q(0) $(F = 0)$, around twice as many photons are emitted before the molecule falls into a dark state. Factoring this into the result of eq. 4.1 we get $R_{\rm sys} \approx (2/\epsilon) = (1/65)$.

The next step was to take some EDM data with the probe beam on resonance with the Q(0) $(F = 1)$ transition to check if any large systematics were present. For this the relay switch optical link was fixed, so that E was actually reversing. Upon analysis we found that the $F = 1$ data failed one of our systematic checks: an EDM on the order of $10^{-26}\,e$.cm dependent on the arrival time was seen in the analysis. Furthermore, this dependence changed with probe beam polarisation. The characteristics of the systematic are shown in fig. 4.2, where the difference in EDM value between the fast and slow gates is plotted with respect to the angle of the probe polariser.

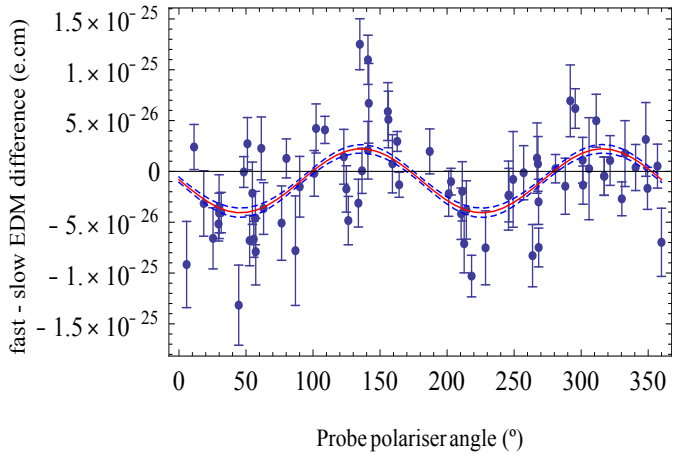

Figure 4.2: *The difference between the EDM measured in the fast and slow gates with respect to the probe beam polarisation angle when probing on the Q(0) $(F = 1)$ transition. Each point represents the result from an individual block. The peak - to - peak difference is* $8 \times 10^{-26}\,e.cm$. *The 68 % confidence band is shown as a dashed blue line.*

One hypothesis for the effect is that the LIF seen when driving the Q(0) $(F = 1)$

transition not only relates to the population in the $F = 1$ state, but also the phase difference between the $|1, \pm 1\rangle$ sublevels; these states can be driven to the same excited state by light polarised perpendicular to the quantization axis of the molecule.[5] So, if the E and B fields that the molecules see after rf2 are not uniform over the length of the YbF cloud and change when E_z and B_z are switched then it possible such a systematic would be seen.

To estimate the size of the fake EDM this systematic could cause in normal $F = 0$ probe data we take the peak - to - peak amplitude in fig. 4.2 and account for the suppression from $R_{\rm sys}$ and the rotation of the probe beam's polarisation. Noting that the polarisation is rotated randomly between every block the rotator's suppression factor can be taken to be approximately $\frac{1}{\sqrt{n_{\rm blocks}}}$, where $n_{\rm blocks}$ is the number of blocks in the dataset to give,

$$\begin{aligned} d_{\rm e}^{F=1} &= \frac{R_{\rm sys}}{\sqrt{n_{\rm blocks}}}\, 8 \times 10^{-26}\, e.{\rm cm} \\ &= 1.5 \times 10^{-29}\, e.{\rm cm}. \end{aligned} \tag{4.2}$$

This is more than an order of magnitude smaller than $5 \times 10^{-28}\, e.$cm, the sensitivity we wish to measure d_e to. In preliminary data where we probe the $F = 0$ level with the E - field switching no dependence on the angle has been seen.

4.2.2 g - factor dependence on E

As was shown in eq. 1.18, sec. 1.6, the Zeeman splitting of the $|1, \pm 1\,\rangle$ states by the magnetic field B_z results in a phase difference, $2\phi_B$. I repeat the equation here, but explicitly state the dependence of the interaction on the g - factor, g_F,

$$\phi_B = -\tfrac{1}{\hbar}(g_F\, \mu_B\, B_z)\tau, \tag{4.3}$$

where g_F relates the total angular momentum of the states ($m_F = \pm 1$) to the interaction with an applied magnetic field (B_z). For the $F = 1$ state the electron and F nuclear spins both contribute to the total angular momentum equally, but compared to the electron the nucleus has a negligible magnetic moment. Hence, g_F is $g_e/2 = -2.002/2 = -1.001\,(4.\,s.\,f.\,)$. We do not need to know the value of g_F to an extremely high precision. What is more important for an EDM measurement is that it does not change when E is switched, since under certain conditions (these will be outlined later) this could masquerade as an EDM.

[5] Meaning, interference can occur between state amplitudes of $|1, \pm 1\rangle$.

When a static E field is applied to a molecule a mixing of its states and consequently their angular momenta occurs.[6] The amount of mixing depends on the size of the applied field, so if the magnitude of E changes when it is reversed we could imagine the value of g_F also changing. To test this empirically we acquired scans of the interference curve, by incrementing B_z between shots, at various E-fields. A $\cos^2$ lineshape was then fitted to each scan and the lineshape's period was used as a measure of g_F.

An interference scan taken at 10.8 kV/cm (±6.5 kV) is shown in fig. 4.3. It can

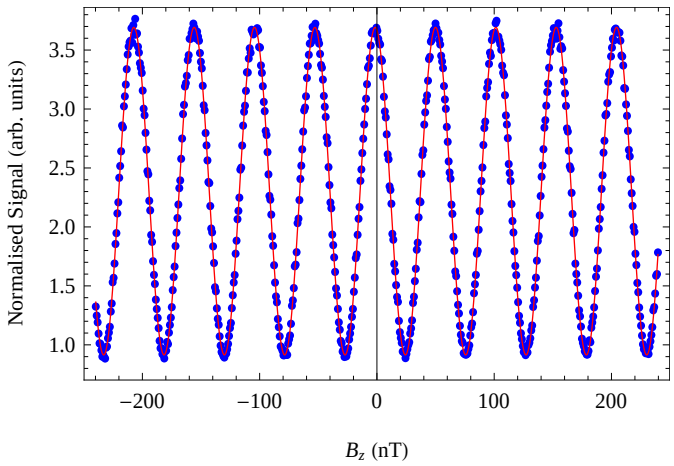

Figure 4.3: *A scan of the interference lineshape at an applied E field of 10.8 kV/cm made by incrementing B_z between shots. Blue data points correspond to the LIF signal seen at the probe and the red line to a* $\cos^2$ *fit.*

be seen that the fit (in red) agrees very well with the data points (in blue) over the whole scan of ±200 nT. Scans were also taken at E-field settings of, 3.3, 11.7 and 14.2 kV/cm. The corresponding pitches (inverse of the periods) are plotted in fig. 4.4. The individual error bar on each data point is much smaller than the scatter of the four points. This is because each data point and corresponding uncertainty is derived from multiple scans that were taken within minutes of each other. Between the acquisition of data at different E fields there was a longer period of time. Hence, the error bars are not representative of any slow drifts or changes in the B coil current supply, whereas the scatter of points is.

There does not appear to be any obvious relationship between g_F and the value of E. Nonetheless, we can still take the biggest gradient we see between the data points to put an upper bound on any potential dependence.

The sharpest step occurs between fields of 10.8 and 11.7 kV/cm, where the pitches are 0.01944 nT^{-1} and 0.01939 nT^{-1} respectively. The fractional change in g_F with

[6] The Stark shift is mainly a result of the mixing of different rotational levels.

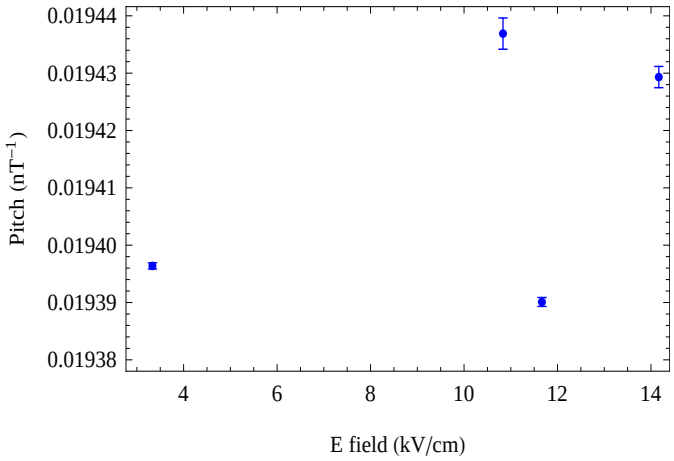

Figure 4.4: *The pitch of the measured interference lineshape with respect to the applied E field. Indicates there is no strong correlation between g_F and the magnitude of E.*

respect to a change in E of 1 V/cm is:

$$\begin{aligned} \Delta_{g_F} &= \frac{1}{11700 - 10800}\left(\frac{0.01939 - 0.01944}{(0.01939 + 0.01944)/2}\right)\,(\mathrm{V/cm})^{-1} \\ &= -2.86 \times 10^{-6}\,(\mathrm{V/cm})^{-1}. \end{aligned} \tag{4.4}$$

So, if there is an asymmetry in the E reversal then we could expect g_F to change when it is switched. When coupled with a background magnetic field that is not correctly cancelled out by B_{bias} this can produce a fake EDM.

Let us take the uncancelled field to be δB (in nT), and the E asymmetry to be δE (in V/cm), such that in one state $E_z = +E_0$ (E_0 is taken to be positive) and in the other, after the reversal, $E_z = -(E_0 + \delta E)$. The non-zero δB combined with the change in g_F, due to the E asymmetry, results in a shift of the interference curve when E is switched by an amount proportional to $\Delta_{g_F} \cdot g_F \cdot \delta E \cdot \gamma_B$. This shift can not be distinguished from the one that a real EDM would produce, because of the limited way in which we sample the lineshape when taking data. The size of the fake EDM, derived in a similar way to that of eq. 3.11, is then,

$$\begin{aligned} d_{\mathrm{e}}^{g_F} &= \frac{\Delta_{g_F}\, g_F\, \delta E\, \delta B}{DB} \cdot \frac{\mu_B\, DB}{\eta\, E_{eff}} \\ &= \frac{2.86 \times 10^{-6} \cdot 1.001 \cdot \delta E\, \delta B}{1.67\,\mathrm{nT}} \cdot \frac{\mu_B \cdot 1.67\,nT}{0.58 \cdot 25\,\mathrm{GV/cm}} \\ &= 1.15 \times 10^{-29}\,\mathrm{e.cm}\,(\mathrm{V/cm})^{-1}\,(\mathrm{nT})^{-1} \end{aligned} \tag{4.5}$$

where η was evaluated for a field of 11.7 kV/cm and positive/negative signs have been dropped. As a worst case we can assume that the B_{bias} lock keeps δB to within at least $DB/10 \approx 0.2\,nT$.[7] The E asymmetry can be evaluated with the ***E.RF1F*** and ***E.RF2F*** channels, since they tell us how much the rf detuning changes when E is reversed. Of course for the null dataset this was very small because the field was not actually switching, but in preliminary data we have taken with the E switch activated a δE of at most 100 mV/cm is measured. This gives a systematic EDM of,

$$\begin{aligned} d_e^{g_F} &= 0.2 \times 0.1 \times 1.15 \times 10^{-29}\, e.\text{cm} \\ &= 2.3 \times 10^{-31}\, e.\text{cm}. \end{aligned} \tag{4.6}$$

4.2.3 Ramsey component

As already discussed we can not set rf1 and rf2 to be perfect π - pulses. Therefore, their is small Ramsey component in our output signal. Here, I calculate the potential size of the systematic it can produce and then evaluate how well our rf phase flipping and scrambling techniques suppress it.

The contribution to our interferometer output from Ramsey interference, as was given in eq. 2.11, is,

$$\begin{aligned} RAMS = {} & 2\beta_1^2\beta_2^2 \cos(\omega_z t_e) \sin\left(\tfrac{\overline{\Omega}_1\tau_1}{2}\right) \sin\left(\tfrac{\overline{\Omega}_2\tau_2}{2}\right) \times \\ & \Big[\cos(\delta_e t_e + \phi)\left(-\cos\left(\tfrac{\overline{\Omega}_1\tau_1}{2}\right)\cos\left(\tfrac{\overline{\Omega}_2\tau_2}{2}\right) + \Delta_1^2\Delta_2^2 \sin\left(\tfrac{\overline{\Omega}_1\tau_1}{2}\right)\sin\left(\tfrac{\overline{\Omega}_2\tau_2}{2}\right)\right) \\ & + \sin(\delta_e t_e + \phi)\left(\Delta_1 \sin\left(\tfrac{\overline{\Omega}_1\tau_1}{2}\right)\cos\left(\tfrac{\overline{\Omega}_2\tau_2}{2}\right) + \Delta_2 \cos\left(\tfrac{\overline{\Omega}_1\tau_1}{2}\right)\sin\left(\tfrac{\overline{\Omega}_2\tau_2}{2}\right)\right)\Big]. \end{aligned} \tag{4.7}$$

In the EDM channel this component cancels out exactly if the E reversal is symmetric. However, if it is not δ_e[8] changes when E is switched, which in turn, causes a modulation in $RAMS$. The greatest change in $RAMS$ occurs when the asymmetry is such that $\delta_e t_e \rightarrow \delta_e t_e + \pi$. Under normal operation, where $t_e = 660\,\mu$s and

[7] Averaged over the whole null dataset δB was around $DB/100$.

[8] The detuning of the rf frequency with respect to the Stark shifted hyperfine splitting $|0,0\rangle \longleftrightarrow |1,\pm1\rangle$ during the evolution period

$E_z = \pm 11.7\,\mathrm{kV/cm}$, this corresponds to a field asymmetry of $3\,\mathrm{V/cm}$ such that $\delta_e \rightarrow \delta_e + 4760\,\mathrm{rad/s}$ upon reversing E. This asymmetry is much larger than the one we actually measure ($\sim$100 mV/cm), but in estimating the systematic the bigger value is used as a worst case scenario. The rf parameters are taken to be the same for both rf1 and rf2:

$$\begin{aligned} \tau_1 &= \tau_2 = 20\,\mu\mathrm{s} \\ \Delta_1 &= \Delta_2 = \frac{\pm 2380\,\mathrm{rad/s}}{\sqrt{(\pm 2380\,\mathrm{rad/s})^2 + \Omega^2}} \\ \beta_1 &= \beta_2 = \frac{\Omega}{\sqrt{(\pm 2380\mathrm{rad/s})^2 + \Omega^2}} \end{aligned} \tag{4.8}$$

where the $\pm$ represents the change in rf detuning when E is switched[9] and $\Omega = \frac{1.05\,\pi}{20\,\mu\mathrm{s}}$. The factor of 1.05 accounts for a moderate rf amplitude detuning, which makes the effect slightly bigger. The magnetic field step sizes (ω_z depends on these) are taken as $B_0 = 13.5\,\mathrm{nT}$ and $DB = 1.67\,\mathrm{nT}$ with an uncancelled background field of $\delta B = 0.2\,\mathrm{nT}$. Under these conditions the potential size of the Ramsey systematic is,

$$\begin{aligned} d_{\mathrm{e}}^{rams} &= 3.4 \times 10^{-26}\, e.\mathrm{cm}\,(\mathrm{nT})^{-1} \cdot \delta B \\ &= 6 \times 10^{-27}\, e.\mathrm{cm}. \end{aligned} \tag{4.9}$$

For this derivation the size of the ***EDM*** and ***DB*** channels were calculated using the expression given in eq. 2.11[10] and the their ratio was entered into eq. 3.11.

Changing ϕ in eq. 4.7 changes the value of d_{e}^{rams}. As already discussed, we vary ϕ during data acquisition to wash out the Ramsey component in our signal: 1) the π-flipper modulates the phase discretely between ϕ and $\phi + \pi$ — this switches the sign of d_{e}^{rams}, and 2) the phase scrambler introduces an additional random amount of phase anywhere between $0 - 14\,\pi$ — this randomises the amplitude of d_{e}^{rams}. The π-flipper and phase scrambler suppress the systematic by factors of 100 and $\sqrt{n_{\mathrm{blocks}}}$ respectively.[11] Taking these into account and assuming a $\delta B = 0.2\,\mathrm{nT}$ we get,

[9] This assumes the rf frequency locks work well enough so that the average detuning is very close to zero, which is the case when we run.

[10] The contribution of *INT* and *CONST* terms to the EDM channel was zero under the conditions mentioned above.

[11] The flipper switches the phase to within 1 % of π (giving the factor of 100) and the scrambler randomises the phase from block-to-block giving the dependence on n_{blocks}.

$$\begin{aligned} d_{\mathrm{e}}^{rams} &= \frac{1}{100}\frac{1}{\sqrt{7380}}\,6.8\times10^{-27}\,e.\mathrm{cm} \\ &= 8\times10^{-31}\,e.\mathrm{cm}. \end{aligned} \tag{4.10}$$

In an actual measurement the systematic will be even smaller, because δE is not as large as 3 V/cm, as has been assumed here.

4.2.4 Geometric phase

For the E and B fields typically present in our experiment, the Stark induced splitting, Δ_s, between the $|1,\pm1\rangle$ and $|1,0\rangle$ levels is much larger than the Zeeman splitting of $|1,\pm1\rangle$ (see sec. 4.2.5). This means that if E_z varies in orientation adiabatically (rate of rotation $\ll \Delta_s$) a molecule in an eigenstate of the Stark Hamiltonian, $\hat{H}_{Stark}(E_z)$, remains in an eigenstate of $\hat{H}_{Stark}$ at all times, irrespective of the B - field. Taking the particular case where E_z rotates through a closed path in space, C, returning to its original orientation after a time T, it may be expected that the phase difference accumulated between the $|1,\pm1\rangle$ states would be defined by the usual dynamical phase factor $\exp\left[-i\int_0^T \frac{(E_+-E_-)}{\hbar}dt'\right]$. However, M. V. Berry [57] demonstrated that an additional "geometric phase" or "Berry phase", $\gamma(C)$, that depends only on the Hamiltonian and the geometry of the circuit is also acquired. In the case of our molecule this causes a phase difference between the ±1 spin states, even in the absence of a B_z field.

To illustrate this I will consider a simple rotation of E_z in the fixed lab frame (x,y,z) and see what happens to the spin state. I begin with the molecule in the $\psi = (|{+1}\rangle + |{-1}\rangle)/\sqrt{2}$ superposition, as would be the case after an ideal rf1 pulse (the *split* phase of the experiment). This state corresponds to the spin vector pointing along the y - axis, perpendicular to the initial E_z direction, shown by the thick green and blue arrows respectively in fig. 4.5. In the B_z field this arrow precesses around z, where the angle it makes with y is the phase difference between the $|\pm1\rangle$ states. This precession will be ignored however, since we are interested in only the $\gamma(C)$ phase component. E_z is then rotated through the circuit that traces out the dashed red line in the figure: the field is first tipped into the x - axis about y, then rotated into y about x and then finally back to the original direction along z. The spin vector follows E_z and in doing so it has rotated by $\pi/2$ about z, which is equivalent to having acquired a phase difference of the same angle. This is a geometric phase. It should be noted that because $\hat{H}_{Stark}(E_z) \equiv \hat{H}_{Stark}(-E_z)$ the initial direction of the applied field does not matter, only how it rotates from its original orientation is of significance.

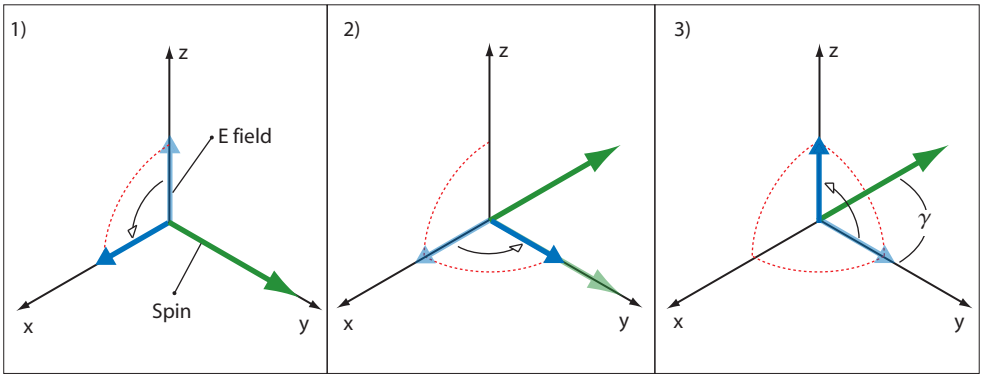

Figure 4.5: *The geometric phase, γ, gained by the spin state (green arrow) when the E - field (dark blue arrow) is adiabatically rotated through a closed loop (red dashed line). The light blue arrow represents the original direction of E at each of the three steps.*

Of course in practice the circuit C will almost certainly be more complicated than the one used in the example and as a result, $\gamma(C)$ will not be able to be found diagrammatically. The derivation of $\gamma(C)$ for an arbitrary circuit is carried out in [58], where the Schrödinger equation is solved for a slowly rotating $\hat{H}_{Stark}(E_z)$. It shows that in the adiabatic limit $\gamma(C)$ is simply given by the solid angle Ω subtended by the circuit,

$$\begin{aligned} \gamma(C) &= \int_S \sin\theta \, d\phi \, d\theta \\ &= \Omega(C) \end{aligned} \tag{4.11}$$

where S is the surface enclosed by C. As explained in [58] and others dealing with geometric phase (e.g. [59]) this result is equivalent to the well known concept of *holonomy* in differential geometry: a vector that undergoes parallel - transport over a closed path on a curved surface[12] will return to its original position pointing in a different direction, even though it was never actively rotated at any point. This change in direction is termed the holonomy angle. The equivalence between $\Gamma(C)$ and the holonomy angle indicates that in the adiabatic limit the spin vector undergoes parallel - transport, i.e., when E_z changes by an infinitesimal amount the new direction of the spin vector is the one that is most parallel to the old one. Although it was not mentioned earlier, it is for this reason that I was able to simply keep the orientation of the spin fixed relative to E_z when demonstrating the phenomenon of geometric phase in fig. 4.5.

[12] Where in our case the curved surface is a sphere.

A systematic geometric phase

In our experiment we know the plates are slightly bowed (see fig. 2.10) — a change in their separation as a function of y — if they are also wedged — a change in separation as a function of x — then it is feasible that the molecules experience a rotating E_z as they travel through them and consequently, pick up a geometric phase. However, this will not produce a fake eEDM because after the field is reversed the rotation will be exactly the same.[13] As a result, $\Gamma(C)$ will remain unchanged.

Next consider patch potentials[14] on the surface of the plates. We have no direct way of measuring the presence of these in our machine, but as a reasonable estimate we could expect one to hold $+1\,\mathrm{V}$ of potential and be circular with a radius of a few cm. By modelling the field from a disc, we find the steepest gradients in potential occur directly above the boundary between the disc and the surrounding surface. Assuming the YbF beam is very narrow, has negligible divergence and lies on a path that is halfway between the plates, the closest the molecules will ever be to the patch is about 6 mm (half the plate separation). At this distance the gradients correspond to radial (perpendicular to z) fields of $E_\mathrm{r} \approx 10\,\mathrm{V/cm}$. The z component can be ignored since it is negligible compared to the applied field of $11.7\,\mathrm{kV/cm}$. When the plate the patch is on is positively charged, the E - field lines will be more concentrated in the volume directly above the patch. Consequently, as the molecules approach it the E - field they see tips up towards the patch in the yz - plane. In addition, if the patch is closer to one edge of the plates as shown in fig. 4.6 there is also a tipping in the xy - plane, with the tilt of E in each plane being approximately $\dfrac{10\,\mathrm{V/cm}}{11700\,\mathrm{V/cm}} \approx 1\,\mathrm{mrad}$. As the molecules move away from the patch E returns to its original orientation having rotated through a solid angle of up to $\approx 1\,\mu\mathrm{rad}$. Looking at the schematic in the figure it is evident the rotation will be anti - clockwise about z. When E_z is reversed the field lines become less dense near the patch so as the molecules approach it E tips away in both planes. But, using the schematic in the figure once again, it can be seen that the sense of rotation will still be anti - clockwise. Therefore, the geometric phase gained is the same in both E states and no fake eEDM is produced.

However, if the effect of the bowed plates is combined with a patch potential, as shown in fig. 4.7 a fake eEDM is produced. Here we assume the bowing and patch are responsible for the tipping of E in the yz and xz - planes respectively. The bowing, represented by the E map data, gives rise to a tilt of about 1 mrad over a length of 200 mm. Coupled with a 1 V patch of dimensions 10 mm and l_p (in mm)

[13] Remember the geometric phase does not care about the direction of the E field only the sense in which it rotates.

[14] An area where the voltage is different by $\mathrm{V_p}$ in comparison to the surrounding region.

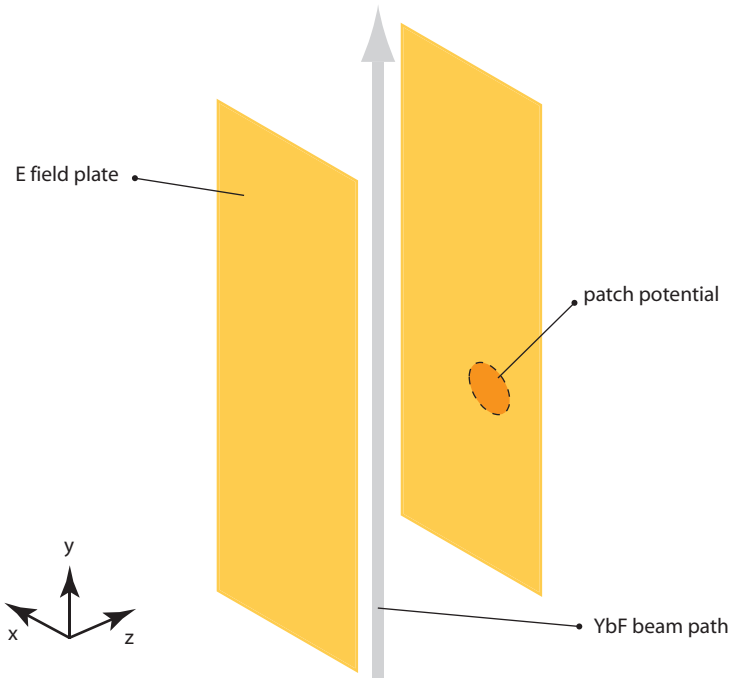

Figure 4.6: *A patch potential positioned closer to one edge of the plates so that as the molecule travels past it the E - field rotates in and out of both the yz and xy - planes. This results in a non - zero $\Gamma(C)$, but not a false eEDM because the direction of the rotation remains the same after an E reversal.*

in the x and y - axes respectively (see fig. 4.7), this gives a geometric phase of,

$$\Gamma = 10^{-3} \left(l_p \frac{10^{-3}}{200\, mm} \right) \text{ rad.} \tag{4.12}$$

The E - field tilt in yz remains the same when E_z is switched, whereas in the xz - plane it reverses. Hence, the phase in eq. 4.12 reverses with E_z, resulting in a fake eEDM. In the worst case we could expect l_p to be 100 mm, which gives a $\Gamma = 0.5\,\mu$rad. This corresponds to an eEDM of $3 \times 10^{-29}\, e$.cm.

So far it has been assumed that the YbF beam is infinitely narrow in the xy - plane. When a more realistic estimate is made by integrating the geometric phase effect over the actual beam volume a smaller fake eEDM results. Here part of the beam gains a positive geometric phase, whereas the other gains a negative one and upon averaging the overall impact of the systematic is reduced to

$$d_e^{geo} = 3 \times 10^{-30}\, e\text{.cm.} \tag{4.13}$$

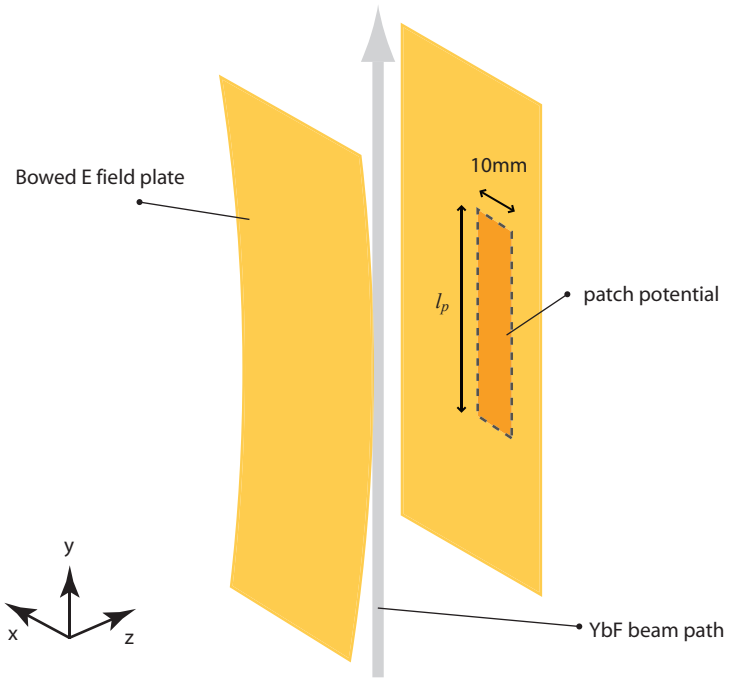

Figure 4.7: *A long, narrow patch potential (with dimensions of $l_p \times 10\,mm$) and bowed plate tips the E - field in the xz and yz - planes.*

In conclusion we see that even when we take an improbably long patch potential of 100 mm the expected geometric phase is small. Nonetheless, we can still put an empirical upper bound on d_e^{geo} by taking data at different E fields. This is because the phase from an actual eEDM and one produced by a patch potential have a different dependence on E: the real eEDM phase is $\propto \eta(E)d_e$ (the dependence of η on the applied field was shown in fig. 1.5) and $\Gamma \propto \frac{1}{E_z}$. This data is yet to be acquired, but it will be more beneficial to take data at a lower E to emphasize the effect of any patch potential. The part of the null data which was taken at 2 kV/cm did not have a switching E - field and as a result can not be used to put an empirical limit on the geometric phase.

4.2.5 Magnetic fields that switch with E

The following produce magnetic fields that are correlated with the direction of E_z:

- leakage currents between the E - field plates
- polarisation of the magnetic shield due to large charging currents
- motion of the molecules in the E - field.

There are other additional sources of such correlated fields, (e.g. the magnetic field from the HV relay box), but these are either cancelled out by the manual E reversal

or can be trivially shown to have a negligible impact. I will evaluate the false EDMs that could be expected from the three listed above.

Leakage currents

The electric field plates, held at high voltage, are susceptible to leakage current flowing between them. This current changes sign when the direction of E_z is switched, making the magnetic field it produces potentially very dangerous.

The relationship between the current (in nA) and the resulting field was estimated in [29] to be,

$$B_{leakage} = 10\, I_{leakage}\, \mathrm{fT}. \tag{4.14}$$

In this case it was assumed *all* the current flowed in the xy - plane, so that $B_{leakage}$ pointed along the z - axis. Though the geometry of the plates and their support structure means it is more likely leakage currents would flow between them in the xz - plane (producing a field along y), this was taken as a worst case scenario; YbF is not particularly sensitive to B - fields perpendicular to E_z as will be explained later.

The fake eEDM per nA of current is then given by[15],

$$d_e^{leakage} = \Delta I_{leakage} \cdot 4 \times 10^{-29}\, e.\mathrm{cm/nA}, \tag{4.15}$$

where $\Delta I_{leakage}$ is the change in the leakage current after E is switched. For the null dataset this is extremely tiny since we were not switching E. With the E switch activated currents of 2 - 4 nA are recorded which according to the above equation results in a systematic effect of $< 1.6 \times 10^{-28}\, e.\mathrm{cm}$. It must be remembered that the estimate in eq. 4.15 was made assuming a fairly improbable current path and *all* the leakage current was taken to flow within the machine (a fraction of the leakage occurs to ground/earth in the HV rack and connecting cables).

Magnetic shield polarisation

The cables that connect the HV supplies to the electric field plates pass through apertures in the side of the inner magnetic shield. There are currents of up to 1 μA flowing in these cables during an E_z reversal. Though we do not take data while the currents are flowing, the B - fields they produce could polarise the shield resulting in a B - field correlated with the switching of the E - field.

To estimate the potential size of this effect we carried out an experiment using a replica inner shield with a loop of copper wire fed through its apertures to represent the HV connections to the plates. Large currents of $\pm 350\, \mu$A were repeatedly pulsed

[15] At 11.7 kV/cm, 10 fT gives the same shift as a d_e of $4 \times 10^{-29}\, e.\mathrm{cm}$

on and off through the loop whilst a fluxgate magnetometer placed inside the shield recorded the field. By correlating the sign of the current pulse with the measured magnetic field we found the magnetisation of the shields to be $60 \pm 90\,\mathrm{fT}$. Taking the upper limit of the potential field, this results in an eEDM of,

$$d_e^{polarisation} = I_{switching} \cdot 1.7 \times 10^{-30}\, e.\mathrm{cm}/\mu\mathrm{A}. \tag{4.16}$$

where $I_{switching}$ is the current during an E switch in μA. For our maximum current of $1\,\mu$A this is well below the sensitivity that we wish to measure at.

Relativistic motional magnetic field

The molecules, which are moving at $\sim 590\,\mathrm{m/s}$ experience a relativistic magnetic field $\vec{B}_{rel} = \dfrac{\vec{E}_z \wedge \vec{v}}{c^2} = \dfrac{E_z\, v}{c^2}\hat{x}$ in their rest frame. For a E_z of $11.7\,\mathrm{kV/cm}$ this equals $\pm 7\,\mathrm{nT}\hat{x}$ depending on the direction of E_z. Fortunately, the relatively large Stark shift, Δ_s ($\sim$9 MHz), of the $|1, \pm 1\rangle$ levels from the $|1, 0\rangle$ state makes YbF very insensitive to B-fields that are transverse to E_z. This was explained in detail in [29] so I only give a brief summary here.

The interaction Hamiltonian for the $F = 1$ state sublevels, $|1, 0\rangle$, $|1, \pm 1\rangle$, is:

$$\hat{H}_T = \hat{H}_{Stark} + \mu_B B_z \hat{\sigma}_z + \mu_B B_\perp \hat{\sigma}_\perp \tag{4.17}$$

where $B_\perp$ and $\hat{\sigma}_\perp$ are the magnetic field and Pauli matrix respectively for a field perpendicular to the z-axis (defined by the direction of E_z). For our experiment $\mu_B B_\perp < \mu_B B_z \ll \Delta_s$. Hence, the third term in H_T can be treated with perturbation theory.

The interferometer output is sensitive to the difference $\Delta E_\pm$ between the $|1, \pm 1\rangle$ energies, which to the zeroth order (and ignoring the eEDM interaction) are $E_\pm^{(0)} = \Delta_s \pm \mu_B B_z$, where $E_0^{(0)} = 0$. To the second-order the perturbation is (there is no first order contribution from $\mu_B B_\perp \hat{\sigma}_\perp$),

$$\begin{aligned} E_\pm^{(2)} &= \frac{|\langle 1, \pm 1|\mu_B B_\perp \hat{\sigma}_\perp|1, 0\rangle|^2}{E_\pm^{(0)} - E_0^{(0)}} \\ &= \frac{(\mu_B B_\perp)^2}{2(\Delta_s \pm \mu_B B_z)} \end{aligned} \tag{4.18}$$

so that,

$$\begin{aligned}\Delta E_{\pm} &= 2\mu_B B_z + \frac{(\mu_B B_\perp)^2}{2}\left(\frac{1}{\Delta_s + \mu_B B_z} - \frac{1}{\Delta_s - \mu_B B_z}\right) \\ &\approx 2\mu_B B_z + \frac{(\mu_B B_\perp)^2 \mu_B B_z}{\Delta_s^2}.\end{aligned} \tag{4.19}$$

The Δ_s^2 in the denominator shows that the effect of $B_\perp$ is hugely suppressed by the presence of the large Stark splitting for the molecule. It can also be seen that the perturbed energy depends on the magnitude of $B_\perp$. Therefore, B_{rel} can only produce a systematic error if it is accompanied by a non - zero, non - switching residual field, B_{res}, along the x - axis, so that upon reversing the E - field $B_\perp = B_{res} + B_{rel} \longrightarrow B_{res} - B_{rel}$.

Assuming a fairly large residual field of $B_{res} = 5\,\mathrm{nT}$ the systematic error from the motional magnetic field turns out to be very small,

$$d_e^{motional} = 1.9 \times 10^{-32}\, e.\mathrm{cm}. \tag{4.20}$$

This takes into account the presence of a perpendicular field only during the free evolution of the molecule. An analytical expression, like the one in eq. 4.19, that describes the impact of $B_\perp$ on the rf interaction regions is difficult to derive. Nonetheless, numerical calculations are simple to perform. They show the presence of an rf field does nothing of note to the size of the systematic.

4.2.6 Driving rf transitions in a magnetic field

To simplify the theory of the rf transitions in sec. 2.6.1 I assumed that the Zeeman splitting of the spin states due to the applied B_z was negligible. However, if we wish to make an accurate measurement of the eEDM the impact of this field in the rf regions must be examined.

Though they are too long to write out explicitly here, appendix B gives the method of finding analytical expressions for the amplitudes of the $|0,0\rangle$ and $|1,\pm1\rangle$ states in the presence of an rf field polarised along the x - axis and a B - field directed along the z - axis.[16] With these expressions we can model the effect on the interference curve and in turn the eEDM measurement. Assuming stray B - fields are zero and considering only the applied B_z in the rf regions the result is as you would expect: 1) a larger phase is acquired for a given B_z, because the model accounts for the fact that the molecules are experiencing the field not only during the evolution

[16] As mentioned in sec. 4.2.5 numerical calculations show the rf transition is insensitive to static B - fields that are perpendicular to E_z.

period but also for the duration of rf1 and rf2, and 2) the fringe contrast decreases as the magnitude of B_z becomes larger, because the Zeeman splitting causes an increasing rf detuning. When coupled with an asymmetric E reversal and considerable rf detunings fake eEDMs are produced. However, these are many orders of magnitude smaller than $10^{-28}\,e.\text{cm}$.

Much larger false EDMs are produced if there is an inhomogeneous stray magnetic field, B_{stray}, present. This is shown in fig. 4.8 where B_{stray} has been taken to be 40 nT in the rf1 region (zero elsewhere)[17] and the false eEDMs produced for various E-field asymmetries over a range of rf1 detunings are plotted. These are defined so that, for example, a change in the Stark shifted hyperfine splitting from $173.000 + 0.001$ MHz to $173.000 - 0.001$ MHz when E is reversed and a rf1 frequency of 173.005 MHz translates to a 1 kHz asymmetry and a 5 kHz rf detuning.

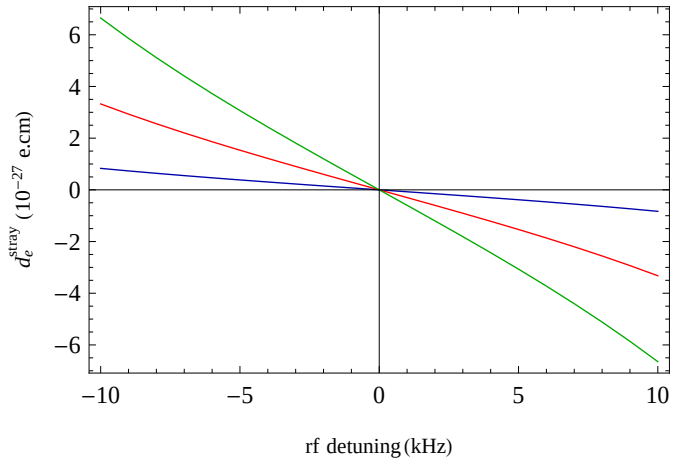

Figure 4.8: *The theoretical fake eEDM caused by a static stray magnetic field of 40 nT in the rf1 region with respect to rf1 detuning. The blue, red and green lines correspond to E asymmetries of 25, 50 and 100 Hz (∼ 200 mV/cm,∼ 400 mV/cm,∼ 800 mV/cm) respectively. The rf pulse length was set to 20 μs and the amplitude such that at zero detuning a π-pulse would be administered.*

The systematic effect is approximately linearly proportional to the rf detuning, δ_{rf1} (in kHz), E asymmetry, ν_{asym} (in kHz) and a B_{stray} in the rf1 region so that,

$$d_e^{stray} = 8 \times 10^{-29}\,\delta_{rf1}\,\nu_{\text{asym}}\,B_{\text{stray}}\,e.\text{cm}\,\text{kHz}^{-2}\,\text{nT}^{-1} \tag{4.21}$$

where B_{stray} is present in only the rf1 region. A stray field in the rf2 region is easily accounted for by adding a term of exactly the same form as in eq. 4.21 but where

[17] This is comparable to the ambient B-field map data (see fig. 2.12) where the rf1 region corresponds to 0.6 m.

δ_{rf1} is replaced with δ_{rf2}.

Taking $B_{\text{stray}} = 40\,\text{nT}$ in the rf1 region, our reversal asymmetry of 100 mV/cm ($\equiv \nu_{\text{asym}} = 0.0125\,\text{kHz}$) and a rf1 detuning of 1 kHz the fake EDM is,

$$d_e^{stray} = 4 \times 10^{-29}\, e.\text{cm}. \tag{4.22}$$

4.2.7 E asymmetry data

As has been shown there are various systematic effects that depend on δE, the asymmetry of the E reversal (defined in sec. 4.2.3). Therefore, the relationship between δE and the measured EDM was tested empirically by taking data with various applied asymmetries. To introduce a given δE the program voltage sent to one of the HV supplies was changed when E was switched, resulting in an E magnitude that changed with the state of E.

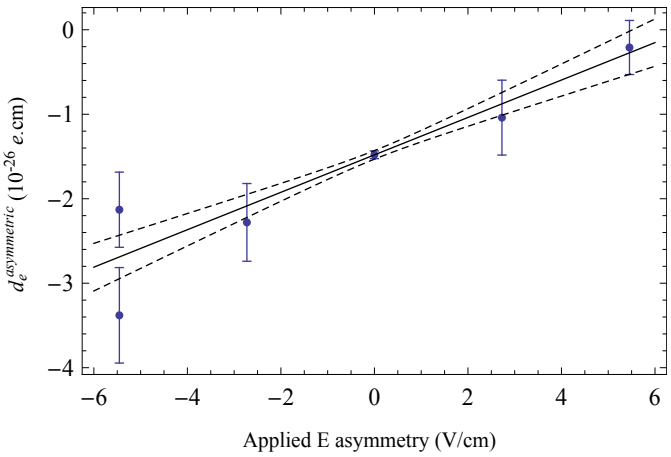

Figure 4.9: *Measured fake EDM (with blind) caused by an applied E asymmetry. The dashed lines represent the 68 % confidence band.*

From fig. 4.9 it can be seen that there is a large fake EDM that is proportional to δE. The gradient of the line is $2.2 \pm 0.4 \times 10^{-27}\, e.\text{cm}/(\text{V/cm})$. The fake signal switches with the manual state of B but not the rf direction, just like a real EDM. Its relationship with the manual E reversal, which is carried out at the output of the HV relay, is slightly more complicated. This is because the systematic depends only on magnitude changes of E, but not its direction. Hence, a voltage asymmetry that originates before the outputs of the HV relay (e.g. an asymmetry caused by contact potentials on the relay connections) would be cancelled out by the manual E reversal, whereas one that occurs after (e.g. due to patch potentials on the E plates) would not and, as a result, we would not be able to differentiate the fake EDM it produced from a real one.

As already mentioned, preliminary data with the E - field switching indicates that there is a field asymmetry of around 100 mV/cm occurring after the outputs of the relay. Taking the upper limit of the gradient in fig. 4.9 the resulting fake EDM we could expect is,

$$\begin{aligned} d_e^{asymmetric} &= 2.6 \times 10^{-27}\, e.\mathrm{cm}/(\mathrm{V/cm}) \times 0.1\,\mathrm{V/cm} \\ &= 2.6 \times 10^{-28}\, e.\mathrm{cm}. \end{aligned} \tag{4.23}$$

This is much larger than all the previously discussed δE dependent systematics,, combined. Therefore, there is some additional physical mechanism which we are not aware of that is producing this systematic. The effect is comparable to our statistical uncertainty of $\sim 5\times10^{-28}\, e.\mathrm{cm}$. With further investigation if the systematic is found to be caused by a change in the detuning of the rf transitions when E is switched the effect could be corrected for because the amount of asymmetry in the two rf regions can be evaluated with the ***E.RF1F*** and ***E.RF2F*** channel values.

4.2.8 Summary of systematic errors

In table. 4.4 the systematics that have been discussed in the this chapter are listed. Where relevant, it should be noted that in estimating their sizes δB (the uncancelled B - field) and δE (the E asymmetry) were taken to be 0.2 nT and 100 mV/cm respectively. It should be noted that the empirical limit on $d_{\mathrm{e}}^{asymmetric}$ includes not only the effect of the unknown mechanism discussed in sec. 4.2.7 but also the systematics entered below the dashed line in table. 4.4, $d_{\mathrm{e}}^{g_F}$, d_{e}^{rams} and d_{e}^{stray}.

Table 4.4: *List of systematic effects and their respective sizes. Those below the dashed line are included in the estimate of* $d_e^{asymmetric}$.

Systematic effect	Size of fake EDM (e.cm)
$d_{\mathrm{e}}^{F=1}$	1.5×10^{-29}
d_e^{geo}	3×10^{-30}
$d_e^{leakage}$	1.6×10^{-28}
$d_e^{polarisation}$	1.7×10^{-30}
$d_e^{motional}$	1.9×10^{-32}
$d_{\mathrm{e}}^{asymmetric}$	2.6×10^{-28}
$d_{\mathrm{e}}^{g_F}$	2.3×10^{-31}
d_{e}^{rams}	8×10^{-31}
d_{e}^{stray}	4×10^{-29}

Looking at the table we can see that only $d_e^{leakage}$ and $d_e^{asymmetric}$ will be of significance to a real EDM measurement aiming to measure at the $10^{-28}\,e$.cm level.

4.3 The null result (blind removed)

The EDM blind was unveiled to be $26.4 \times 10^{-28}\,e$.cm, resulting in an unblinded final null EDM result,

$$d_e^{null}(\text{at } 68\,\%\text{ CI}) = 6.1 \pm 4.7 \times 10^{-28}\,e.\text{cm}. \tag{4.24}$$

That the mean value lies just outside the region defined by the error bar is not statistically significant at this confidence interval. At the larger 95 % interval,

$$d_e^{null}(\text{at } 95\,\%\text{ confidence level}) = 6.4 \pm 9.1 \times 10^{-28}\,e.\text{cm}. \tag{4.25}$$

So we find from a null dataset containing 7380 blocks an EDM consistent with zero at an uncertainty better than the current world limit. Next, I briefly discuss the characteristics of the random noise in our dataset.

4.4 Sources of noise

As has already been mentioned the main sources of random noise in our EDM measurement are: photon shot noise, molecular source noise, and fluctuations in the ambient B-field.[18]

The EDM uncertainty we would expect in the shot noise limit, $\sigma_{d_e}^{SN}$, is simple to evaluate. The probe PMT has a calibration factor of 0.104 V/MHz, i.e., an output of 0.104 V would be recorded if detecting 10^6 photons per second. In the null dataset the average probe PMT signal per shot in the center gate was 89 Vμs, or $89/0.104 = 858$ counts per shot and $858 \times 4096 \times 7380 = 2.6 \times 10^{10}$ counts for the whole dataset. So, in the shot noise limit we would be able to resolve a signal change of,

$$\begin{aligned} \Delta S &= \frac{89\,\text{V}\mu\text{s}}{\sqrt{2.6 \times 10^{10}}} \\ &\approx 6 \times 10^{-4}\,\text{V}\mu\text{s}. \end{aligned} \tag{4.26}$$

Using ***DB***, which has a channel value of ≈10 Vμs in the unnormalised probe PMT

[18] Other noise sources include, E field drifts, laser drop outs/fluctuations and electrical noise.

data, as a means of calibration we find ΔS is equivalent to a phase change of 5 μrad and in turn a $\sigma_{d_e}^{SN}$ of 3.3×10^{-28} e.cm. Here, I have used the fact that ***DB*** corresponds to a phase of 0.1 rad and a d_e of 10^{-28} e.cm produces a 1.64 μrad phase change under our operating conditions. However, we know from table 4.2 that there is a fair amount of source noise, since after normalisation the uncertainty is markedly reduced from 5.9 to 4.7×10^{-28} e.cm, a 25 % improvement. Accounting for the additional photon shot noise the pump PMT[19] introduces, $\sigma_{d_e}^{SN}$ inflates slightly to 3.6×10^{-28} e.cm for the normalised signal. Nonetheless, this is still smaller than the measured uncertainty. There is some evidence that magnetic field noise could be the cause of this discrepancy.

The measured EDM is most sensitive to stray B-fields that drift on the same time-scale as the E switching period (10 – 30 s). To test the impact of these on our dataset the ***EDM*** from each block was plotted against the corresponding ***E*** channel in the magnetometer signal. This data is shown in fig. 4.10. There is a

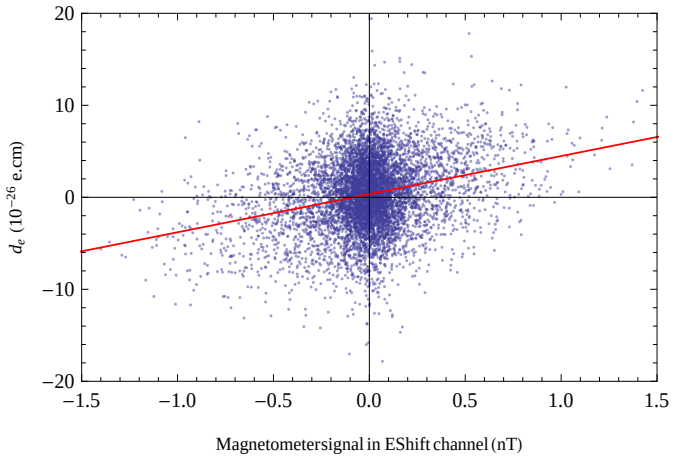

Figure 4.10: *The EDM from each block plotted against the* ***E*** *channel measured in the magnetometer signal. A line of best fit is shown in red to guide the eye.*

clear dependence of measured stray B-field and ***EDM***. This is more apparent at the extremes of the distribution where the large magnetic fields dominate over other sources of noise.

Using the gradient of the best-fit line shown in red in the figure the dependence was corrected for and data analysed like normal. Though the large outlying EDMs were pulled in by the correction, it was found that the final bootstrapped uncertainty on the measurement did not decrease. This is because for most of the data the stray field is very small and applying the correction actually introduces more noise (from the magnetometer signal) than it removes. There is also the issue that the

[19] This has a calibration of 0.021 V/MHz and average signal 70 Vμs.

magnetometer sits outside the inner shield and therefore does not sample the same region as the molecules.

Either by reducing the magnetic field noise or measuring the noise in a more reliable and sensitive fashion than we do now we should be able to work closer to the shot noise limit. This is particularly important, because even if we completely eliminated the shot and source noise the uncertainty on the measurement from purely magnetic field fluctuations (for a dataset of similar length to our null test) would still be approximately $\sqrt{4.7^2 - 3.3^2} \times 10^{-28}\, e.\text{cm} = 3.35 \times 10^{-28}\, e.\text{cm}$.

Chapter 5

Conclusions and outlook

Though an EDM measurement has not been made during my thesis a null dataset with a statistical sensitivity of $4.65 \times 10^{-28}\, e$.cm has been acquired. With this dataset and additional diagnostic experiments we have demonstrated that potential systematic effects are in the worst-case scenario $3.1 \times 10^{-28}\, e$.cm. However, with further investigation of the $d_e^{asymmetry}$ systematic and relatively simple empirical tests this estimate could be reduced. We have also shown that the advances in reliability and automation mean the experiment can be run around the clock with very little manpower, letting us take 220 blocks per day, which corresponds to a statistical sensitivity of $2.7 \times 10^{-27}\, e.\text{cm}/\sqrt{day}$. The next step should be to replace the dye laser with the solid state fibre laser system, leaving the rest of the experimental setup as it is, and make a world-beating measurement of d_e.

After making this measurement there will still be much upside to using YbF, since there is a lot of scope for improving the statistical sensitivity and reducing the size of systematic effects. It is likely the most efficient path will be to build a new experiment, rather than modify the current one.

5.1 Outlook

Here I discuss the possible features of a next generation YbF EDM experiment.

Buffer gas source

The statistical sensitivity of the measurement would be improved if the flux of molecules from the supersonic source was increased and their velocity decreased. At present there is a flux of 10^5 molecules moving so quickly that they only interact with the applied E and B-fields for less than a ms. One promising alternative to the supersonic source is to use a pulsed buffer gas source. The YbF is created in a cell containing cryogenically cooled, to a few K, He atoms (the buffer gas), the YbF

thermalises with the He and cooled molecules emerge through a small aperture in the cell. Such a source is already being developed at Imperial College. At present each pulse has a speed of between 150 - 200 m/s, a temperature of 4 K and contains 10^{10} molecules. The speed of the molecules can be tuned with the buffer gas pressure, giving us a useful tool for investigating systematic effects. It may be worth trying to run this new source at 50 Hz to give, in effect, a further factor of 2 more molecules. A Stark decelerator could even be added to the buffer gas source with the aim of slowing down the molecules to the point that a YbF fountain could be implemented. To get the full potential out of the fountain, however, the molecules would need to be cooler than a few K to prevent the cloud density becoming extremely sparse.

Increased magnetic shielding

As was discussed in sec. 4.4 magnetic field noise has a significant impact on the sensitivity of the measurement; it is of the same order as the photon shot noise. By adding an additional layer of shielding the amount of noise would be reduced. We can see from the B - field map data (see fig. 2.11) that the ambient field is large at the extremes of the interaction region. Though this is not a critical problem it could be removed with longer shields or with small Helmholtz coils to cancel out the ambient field.

Since the magnetic noise field is known to drift slowly, increasing the frequency of the E switch would also help. It may be possible to do this, whilst maintaining a reasonable duty cycle, by reducing the size and length of the E field plates. This would reduce the interaction time and hence, the statistical sensitivity, but more may actually be gained in terms of overall sensitivity.

Improved magnetometry

Currently we use a single fluxgate magnetometer to detect magnetic fields near the YbF beam path. One major problem with this technique is that it does not allows us to sample the same region as the molecular beam. A possible solution could be to use CaF as a comagnetometer, since it is insensitive to the eEDM, but sensitive to magnetic fields. It would have the advantage that we would be able to use it to cancel out the geometric phase effect in addition to systematics originating from B - fields that switch with E. Using CaF would complicate the experimental technique, however. We would need an additional laser for the pump and probe phases of the experiment and the rf pulses would have to be modified to also drive transitions between the CaF hyperfine states. A more immediate solution to the issue of magnetometry would be to simply use more fluxgates positioned in such a way that stray B - fields and their gradients could be inferred. Optical Rb cell

magnetometers, which are more sensitive than fluxgates, are also an option, but like the CaF comagnetometer would provide numerous extra technical challenges.

Flatter electric field plates

The E - field map shows that the electric field plates bow under the pressure from the electrical feedthroughs. Currently the inhomogeneous field means that a π - pulse can not be administered to all the molecules in a given molecular cloud. By replacing the plates with flatter ones that provide a uniform E - field, the split and recombine phases of the experiment will become more efficient, resulting in an improved signal at the interferometer output. Also any potential systematics that are caused by E - field gradients, such as geometric phase, will be reduced.

Enhanced rf pulse control

Another limit on the efficiency of the split and recombine phases is the fact that we drive the rf transitions in a B - field which splits the $|1,+1\rangle$ and $|1,-1\rangle$ states by around 200 Hz. This means the rf frequency can not be simultaneously on resonance for both the $|0,0\rangle \rightleftharpoons |1,-1\rangle$ and $|0,0\rangle \rightleftharpoons |1,+1\rangle$ transitions. By reducing the duration of the rf pulses their linewidth (currently 50 kHz) would be increased and the effect of the Zeeman splitting would be reduced. At present the rf amplifier does not have enough gain to provide the amplitude needed to meet the π - pulse condition for durations much less than 20 μs. A newer amplifier, the *CPC MRI plus*, will let us reduce the length of rf1 and rf2 down to 1 μs, increasing the linewidth of the pulses by a factor of 20 to 1 MHz. This will also suppress systematics that depend on the rf detuning (see sec. 4.2).

Even better than shortened pulses might be to use the adiabatic rapid passage (ARP) technique [60]. Here the amplitude or frequency is chirped during the pulse. By properly choosing the chirp characteristics the rf transition can be made more robust to detunings of the rf parameters and more state selective than a standard transform limited pulse. The increased flexibility ARP provides will also be very useful in investigating systematic effects. Of course, to implement ARP the current rf source will have to replaced. The plan is to use a fast programmable abritary waveform generator, for example the *NI PXIe - 5442*, and then frequency quadruple its output.

Improved rf coupling

The rf - field contains a relatively large circularly polarised component near the E - field plate ends as shown in fig. 2.13. To avoid the added complications the circular

polarisation brings to the evaluation of systematic effects we administer rf1 and rf2 when the rf - field is linear, limiting the potential interaction time. Preliminary measurements have been made on a mock - up of the plates and they show that by simply adjusting the position at which the rf cables are connected to the bottom and top edges of the plates the circular component can be reduced. At present the connections are made on the corners of the plates which turns out to be the worst configuration. With this improvement we could see the useable length of the plates increase by 20 - 30 %.

It is hoped the next generation EDM experiment will be able to probe an eEDM to at least the $10^{-30}\,e$.cm level. Depending on how the further systematic investigations go it may then be necessary to move to another polar molecule that has stable (or at least metastable) states with opposite parity, such as ThO.

Appendix A

Bow-tie cavity

A.1 ABCD matrices and efficiency calculations

This appendix contains the details needed to calculate ABCD matrix for a round trip of a bow - tie cavity as shown in 2.17 containing a Brewster cut crystal of length l, refractive index n and a $M4$ to $M3$ (via $M1$ and $M2$) distance of c_l. The matrix for each optical component is given, and the origin O is taken to be at the centre of the crystal which coincides with the primary focus. It has been kept as general as possible so it can be used as a reference for people in the group wishing to design and build a doubling cavity. The parameter $t = l \sin[\arctan n]$.

The $ABCD$ matrix (there is one for each plane) for the cavity is given by:

$$M_{s,t} = M_{CO} \cdot M_{M3C} \cdot M_{M3} \cdot M_{M4M3} \cdot M_{M4} \cdot M_{CM4} \cdot M_{OC} \tag{A.1}$$

The method described in sec. 2.9.3is used to chose and find c_l, f, ϕ and v. Then values for the expected waist sizes at the primary focus w_s and w_t can be calculated. The ξ term is:

$$\xi = \frac{l}{\frac{2\pi n}{\lambda} w_s w_t} \tag{A.2}$$

Assuming perfect phase matching and zero walk - off h is only a function of ξ see [49],

$$h[\xi] = \frac{2.084^{1.91}\xi}{|\xi - 2.084|^{1.91} + \frac{2.084^{1.91}}{1.068}} \tag{A.3}$$

With these two equations you can find how close the cavity design is to optimising h.

Table A.1: *Transfer matrices for a bow-tie cavity*

Optical Element	tangential plane	sagittal plane
M_{OC}: ray travelling from crystal centre to it's first surface towards $M4$.	$\begin{pmatrix} \frac{1}{n} & 0 \\ 0 & n \end{pmatrix} \begin{pmatrix} 1 & t\frac{\sqrt{1+n^2}}{2n^2} \\ 0 & n \end{pmatrix}$	$\begin{pmatrix} 1 & t\frac{\sqrt{1+n^2}}{2n^2} \\ 0 & n \end{pmatrix}$
M_{CM4}: crystal surface to $M4$.	$\begin{pmatrix} 1 & v \\ 0 & 1 \end{pmatrix}$	$\begin{pmatrix} 1 & v \\ 0 & 1 \end{pmatrix}$
M_{M4}	$\begin{pmatrix} 1 & 0 \\ \frac{-1}{f\cos(\phi/2)} & 1 \end{pmatrix}$	$\begin{pmatrix} 1 & 0 \\ \frac{-1}{f}\cos(\phi/2) & 1 \end{pmatrix}$
M_{M4M3}: $M4$ to $M3$	$\begin{pmatrix} 1 & c_l \\ 0 & 1 \end{pmatrix}$	$\begin{pmatrix} 1 & c_l \\ 0 & 1 \end{pmatrix}$
M_{M3}	$\begin{pmatrix} 1 & 0 \\ \frac{-1}{f\cos(\phi/2)} & 1 \end{pmatrix}$	$\begin{pmatrix} 1 & 0 \\ \frac{-1}{f}\cos(\phi/2) & 1 \end{pmatrix}$
M_{M3C}: $M3$ to crystal surface.	$\begin{pmatrix} 1 & v \\ 0 & 1 \end{pmatrix}$	$\begin{pmatrix} 1 & v \\ 0 & 1 \end{pmatrix}$
M_{CO}: surface of crystal to it's centre.	$\begin{pmatrix} 1 & t\frac{\sqrt{1+n^2}}{2n^2} \\ 0 & n \end{pmatrix} \begin{pmatrix} n & 0 \\ 0 & \frac{1}{n} \end{pmatrix}$	$\begin{pmatrix} 1 & t\frac{\sqrt{1+n^2}}{2n^2} \\ 0 & n \end{pmatrix}$

A.2 Cavity alignment

When setting up $L1$ and $L2$ it should be noted that the waist size and position produced is very sensitive to small errors in distance between the fiber and the short collimating lens ($8mm$ in our case). Therefore, it is best to use the optimum positions for $L1$ and $L2$ predicted by theory as a first guess, and then to iteratively move the distance between them and the centre of the cavity using a CCD camera to profile the beam. After mode matching the cavity needs to be aligned.
Cavity alignment procedure (requires an IR viewing card with a $1-2$ mm aperture):

- Set the input polarisation to be horizontal with the $\lambda/2$ plate.
- At minimum laser power, walk the beam onto the centres of $M1$ and $M2$ with $C1$ and $C2$.
- Centre the beam $M3$ using $M2$.
- Centre beam on $M4$ with $M3$.

- Maximise laser power, place a white piece of card between the crystal and $M4$ and you should see a faint green spot. If not tweak $M3$ until you do. If you still don't check the crystal temperature and make sure the beam is passing through unhindered. The crystal position may need adjusting.
- Try and make the spot as bright as possible by tweaking $M3$ whilst ensuring the spot is still approximately at the centre of $M4$.
- Start the PZT scanning full range at a rate of $10 - 100\,\mathrm{Hz}$.
- Remove the white card, place it behind $M4$ outside the cavity and adjust $M4$ so the beam lands on the centre of $M1$.
- Place the IR viewing card between $M1$ and $M2$ but nearer $M1$. Let the beam pass through the aperture, the beam making its second trip/pass should appear on the card.
- Tweak $M4$ such that the second beam passes through the aperture. If you see an intense green spot on the white card skip the next two steps.
- Move the card nearer to $M2$ and let the beam pass through. Adjust $M1$ so that the second pass goes through the aperture.
- Repeat the last two steps until you see green on the output. If you don't then start the alignment procedure again.
- Walk $M1$ and $M4$ until the green is as bright as possible. Measure the output with a fast photodiode, keeping the PZT scan on. You should see a few peaks of different sizes in one full scan range.
- Repeatedly walk $M1$ vs $M4$ and $M2$ vs $M3$ to maximise the green spikes. As you do this one of the peaks will dominate and get larger and the others will die out.
- Now walk $C1$ and $C2$ to further improve signal size and repeat the previous step.
- If the cavity is well aligned there will only be large peaks and they will not be accompanied by smaller peaks. See fig:2.18.

Once the cavity is aligned the locking optics need to be set up.
Locking optics:

- Ensure the beam is landing on both $PD1$ and $PD2$ with the IR card.

- Adjust the $\lambda/4$ and variable attenuator so that the powers landing on the photodiodes are balanced.
- The error signal should be fairly symmetric and centred around 0 V as shown in 2.18.
- If not, continue to adjust $\lambda/4$ and the variable attenuator.
- If the error signal is too small or too large the $\lambda/2$ plate can be adjusted. For our cavity an error signal of peak-peak size between $100-200$ mV is required.
- Try locking the cavity. If it doesn't work the error signal is probably the incorrect sign. Rotate the $\lambda/4$ to flip the signal.
- Once locked tweak the $\lambda/4$ and attenuator to reduce the noise on green output.
- Adjust the crystal oven set point temperature to maximise the output.

Appendix B

RF transition theory

In sec. 2.6 the rf1 and rf2 interactions were modelled for the simplified case where $\omega_z = 0$. Here I give a method of solving the interaction Hamiltonian where $\omega_z \neq= 0$. I begin with the previously derived coupled differentials of the population amplitudes,

$$i\dot{a}_0 = \frac{\Omega}{2} e^{i(\omega_{\rm rf} t+\phi)} a_p \tag{B.1a}$$

$$i\dot{a}_p = \frac{\Omega}{2} e^{-i(\omega_{\rm rf} t+\phi)} a_0 + \omega_z a_m + \omega_0 a_p \tag{B.1b}$$

$$i\dot{a}_m = \omega_z a_p + \omega_0 a_m, \tag{B.1c}$$

where $\Omega = \frac{\mu_B B_x}{\hbar}$ (the Rabi frequency). By using the substitutions $F_p = a_p e^{i(\omega_{\rm rf} t+\phi)}$ and $F_m = a_m e^{i(\omega_{\rm rf} t+\phi)}$, and then taking successive derivatives w.r.t. time these can be re-written as a set of third-order uncoupled equations:

$$\dddot{a}_0 - 2i\delta\ddot{a}_0 + \left(\omega_z^2 - \delta^2 + \frac{\Omega^2}{4}\right)\dot{a}_0 - i\frac{\delta\Omega^2}{4} a_0 = 0 \tag{B.2a}$$

$$\dddot{F}_p - 2i\delta\ddot{F}_p + \left(\omega_z^2 - \delta^2 + \frac{\Omega^2}{4}\right)\dot{F}_p - i\frac{\delta\Omega^2}{4} F_p = 0 \tag{B.2b}$$

$$\dddot{F}_m - 2i\delta\ddot{F}_m + \left(\omega_z^2 - \delta^2 + \frac{\Omega^2}{4}\right)\dot{F}_m - i\frac{\delta\Omega^2}{4} F_m = 0, \tag{B.2c}$$

where $\delta = \omega_{\rm rf} - \omega_0$. These have general solutions of the form,

$$a_0(t) = A_1 e^{i\omega_1 t} + A_2 e^{i\omega_2 t} + A_3 e^{i\omega_3 t} \tag{B.3a}$$

$$F_p(t) = B_1 e^{i\omega_1 t} + B_2 e^{i\omega_2 t} + B_3 e^{i\omega_3 t} \tag{B.3b}$$

$$F_m(t) = C_1 e^{i\omega_1 t} + C_2 e^{i\omega_2 t} + C_3 e^{i\omega_3 t}, \tag{B.3c}$$

where t represents the time since the rf field was turned on, and ω_1, ω_2 and ω_3 are given by the roots of the cubic equation,

$$\omega^3 - 2\delta\omega^2 - \left(\omega_z^2 - \delta^2 + \frac{\Omega^2}{4}\right)\omega + \delta\frac{\Omega^2}{4} = 0. \tag{B.4}$$

The roots of eq. B.4, which are real for real δ, ω_z and Ω, can be found using the cubic formula. Once these are known the nine coefficients can be evaluated by satisfying the simultaneous equations:

$$\begin{aligned} A_1 + A_2 + A_3 &= a_0(0) \\ \omega_1 A_1 + \omega_2 A_2 + \omega_3 A_3 &= -\frac{\Omega}{2} F_p(0) \\ -\omega_1^2 A_1 - \omega_2^2 A_2 - \omega_3^2 A_3 &= \frac{\Omega}{2}\left[-\frac{\Omega}{2} a_0(0) - \delta F_p(0) - \omega_z F_m(0)\right] \end{aligned} \tag{B.5a}$$

$$\begin{aligned} B_1 + B_2 + B_3 &= F_p(0) \\ \omega_1 B_1 + \omega_2 B_2 + \omega_3 B_3 &= -\frac{\Omega}{2} a_0(0) + \delta F_p(0) - \omega_z F_m(0) \\ -\omega_1^2 B_1 - \omega_2^2 B_2 - \omega_3^2 B_3 &= \delta\frac{\Omega}{2} a_0(0) - \left(\omega_z^2 + \delta^2 + \frac{\Omega^2}{4}\right) F_p(0) + 2\delta\omega_z F_m(0) \end{aligned} \tag{B.5b}$$

$$\begin{aligned} C_1 + C_2 + C_3 &= F_m(0) \\ \omega_1 C_1 + \omega_2 C_2 + \omega_3 C_3 &= -\omega_z F_p(0) + \delta F_m(0) \\ -\omega_1^2 C_1 - \omega_2^2 C_2 - \omega_3^2 C_3 &= -\omega_z\frac{\Omega}{2} a_0(0) - 2\delta\omega_z F_p(0) - (\delta^2 + \omega_z^2) F_m(0) \end{aligned} \tag{B.5c}$$

Bibliography

[1] M. Pospelov and A. Ritz. *Electric dipole moments as probes of new physics.* Annals of Physics **318**, 119 (2005).

[2] J. M. Pendlebury, E. A. Hinds. *Particle electric dipole moments.* Nuclear Instruments and Methods in Physics Research A **440**, 471-478 (2000).

[3] C. Orzel. *Measuring (almost) zero.* Physics World, December (2009).

[4] B. C. Regan et al. *New Limit on the Electron Electric Dipole Moment.* Phys. Rev. Lett. **88**, 071805 (2002).

[5] G. L. Kane. *Supersymmetry: what? why? when?.* Contemporary Physics **41**, 359 (2000).

[6] A. D. Sakharov *Violation of CP invariance, C asymmetry, and baryon asymmetry of the universe.* Sov. Phys. JETP Lett. **5**, 24 (1967).

[7] E. M. Purcell and N. F. Ramsey. *On the Possibility of Electric Dipole Moments for Elementary Particles and Nuclei.* Phys. Rev. **78**, 807 (1950).

[8] N. F. Ramsey. *Time Reversal, Charge Conjugation, Magnetic Pole Conjugation, and Parity.* Phys. Rev. **109**, 225 (1958).

[9] C. S. Wu, E. Ambler et al. *Experimental Test of Parity Conservation in Beta Decay.* Phys. Rev. **105**, 1413 (1957).

[10] R. L. Garwin, L. M. Lederman, and M. Weinrich. *Observations of the Failure of Conservation of Parity and Charge Conjugation in Meson Decays: the Magnetic Moment of the Free Muon.* Phys. Rev. **109**, 1415 (1957).

[11] J. H. Christensen et al. *Evidence for the* 2π *Decay of the* K_2^0 *Meson.* Phys. Rev. Lett. **13**, 138 (1964).

[12] B. Aubert et al. (BABAR Collaboration), *Observation of CP Violation in the* B^0 *Meson System.* Phys. Rev. Lett. **87**, 91801 (2001).

[13] N. F. Ramsey. *Electric - dipole moments of elementary particles.* Reports on Progress in Physics **45**, 90 (1982).

[14] F. J. M. Farley et al., *New Method of Measuring Electric Dipole Moments in Storage Rings* Phys. Rev. Lett. **93**, 052001 (2004).

[15] J. H. Smith, E. M. Purcell and N. F. Ramsey, *Experimental Limit of the Electric Dipole Moment of the Neutron.* Phys. Rev. **108**, 120 (1957).

[16] C. A. Baker et al., *Improved Experimental Limit on the Electric Dipole Moment of the Neutron.* Phys. Rev. Lett. **97**, 131801 (2006)

[17] Norman F. Ramsey, *Molecular Beams.* The Clarendon Press, (1956).

[18] J. M. Pendlebury et al., *Geometric - phase - induced false electric dipole moment signals for particles in traps.* Phys. Rev. A **70**, 032102 (2004).

[19] L. I. Schiff, *Measurability of Nuclear Electric Dipole Moments.* Phys. Rev. **132**, 2194 (1963).

[20] P. G. H. Sandars, *Electric dipole moments of charged particles.* Contemporary Physics **(**42), 97 (2001).

[21] J. S. M. Ginges and V. V. Flambaum, *Violations of fundamental symmetries in atoms and tests of unification theories of elementary particles.* Physics Reports **397**, 63 (2004).

[22] W. C. Griffith et al., *Improved Limit on the Permanent Electric Dipole Moment of* ^{199}*Hg.* **102**, 101601 (2009).

[23] V. F. Dmitriev and R. A. Senkov, *Schiff Moment of the Mercury Nucleus and the Proton Dipole Moment.* Phys. Rev. Lett. **91**, 212303 (2003).

[24] M. V. Romalis et al., *New Limit on the Permanent Electric Dipole Moment of* ^{199}*Hg.* **86**, 2505 (2001).

[25] M. V. Romalis and M. P. Ledbetter, *Transverse Spin Relaxation in Liquid* ^{129}*Xe in the Presence of Large Dipolar Fields.* **87**, 067601 (2001).

[26] Z. W. Liu and H. P. Kelly, *Analysis of atomic electric dipole moment in thallium by all-order calculations in many-body perturbation theory.* Phys. Rev. A **45**, R4210 (1992).

[27] K. Abdullah et al., *New experimental limit on the electron electric-dipole moment.* Phys. Rev. Lett. **65**, 2347 (1990).

[28] E. D. Commins et al., *Improved experimental limit on the electric dipole moment of the electron.* Phys. Rev. A **50**, 2960 (1994).

[29] J. J. Hudson. *Measuring the electric dipole moment of the electron with YbF molecules.* Ph.D. thesis, University of Sussex, (2001).

[30] D. Cho, K. Sangster and E. A. Hinds. *Search for time - reversal - symmetry violation in thallium fluoride using a jet source.* Phys. Rev. A **44**, 2783 (1991).

[31] E. A. Hinds *Testing time reversal symmetry using molecules.* Physica Scripta. **T70**, 34 - 41, (1997).

[32] E. D. Commins, J. D Jackson and D. DeMille, *The electric dipole moment of the electron: An intuitive explanation for the evasion of Schiff's theorem.* Am. J. Phys. **75**, 532 - 536 (2007).

[33] P. G. H. Sandars, *The electric - dipole moments of an atom: I and II.* J. Phys. B: At. Mol. Phys. **1**, 499 - 520, (1968).

[34] N. S. Mosyagin, M. G. Kozlov and A. V. Titov. *Electric dipole moment of the electron in the YbF molecule.* **31**, L763 - L767 (1998).

[35] D. Kawall and F. Bay et al. *Precision Zeeman-Stark Spectroscopy of the Metastable* $a(1)[^3\Sigma^+$ *] State of PbO.* Phys. Rev. Lett. **92**, 133007 (2004).

[36] E. R. Meyer and J. L. Bohn. *Prospects for an electron electric-dipole moment search in metastable ThO and* ThF^+. Phys. Rev. A **78**, 010502(R) (2008).

[37] B. E. Sauer, Jun Wang, and E. A. Hinds. *Laser-rf double resonance spectroscopy of* ^{1}*74YbF in the* $X\,^2\Sigma^+$ *state: Spin-rotation, hyperfine interactions, and the electric dipole moment.* J. Chem. Phys. **105**, 7412 (1996).

[38] S. Bickman and P. Hamilton et al. *Preparation and detection of states with simultaneous spin alignment and selectable molecular orientation in PbO.* Phys. Rev. A **80**, 023418 (2009).

[39] J. Lee and A.E. Leanhardt et al. *An Electron Electric Dipole Moment Search in the* $X^3\Delta_1$ *Ground State of Tungsten Carbide Molecules.* J. Mod. Opt. **56**, 2005 (2009).

[40] A. C. Vutha, W. C. Campbell and D. DeMille et al. *Search for the electric dipole moment of the electron with thorium monoxide.* arXiv:0908.2412v1, (2009).

[41] Henry Ashworth. *Towards an improved measurement of the electron electric dipole moment.* Ph.D. thesis, Imperial College London (University of London), (2008).

[42] Paul Constantine Condylis. *Measuring the electron electric dipole moment using supersonic YbF.* Ph.D. thesis, Imperial College London (University of London), (2006).

[43] B. E. Sauer, D. M. Kara, J. J. Hudson et al. *A robust floating nanoammeter.* Rev. Sci. Instrum. **79**, 126102 - 126102 (2008).

[44] J. J. Hudson, H. T. Ashworth et al. *Pulsed beams as field probes for precision measurement.* Phys. Rev. A. Sci. Instrum. **76**, 033410 (2007).

[45] A. Yariv. *Optical Electronics in Modern Communications.* Oxford University Press, (1997).

[46] B. Wyncke and F. Brehat. *Calculation of the effective second-order non-linear coefficients along the phase matching directions in acentric orthorhombic biaxial crystals.* J. Phys. B. **22** 363 - 376 (1989).

[47] G. D. Boyd and D. A. Kleinmann. *Parametric Interaction of Focused Gaussian Light Beams.* J. Appl. Phys. **39**, 3596 3639 (1968).

[48] V. G. Dmitriev, G. G Gurzadyan and D. N. Nikogosyan. *Handbook of Nonlinear Optical Crystals.* Springer - Verlag, (1991).

[49] Y. F. Chen and Y. C. Chen. *Analytical functions for the optimization of second - harmonic generation and parametric generation by focused Gaussian beams.* Appl. Phys. B. **76**, 645 (2003).

[50] T. Freegarde and C. Zimmermann. *On the Design of Enhancement Cavities for Second Harmonic Generation.* Opt. Comm. **199**, 435 (2002).

[51] T. W. Hansch and B. Couillaud. *Laser frequency stabilization by polarization spectroscopy of a reflecting reference cavity.* Opt. Comms. **35**, 441 - 444 (1980).

[52] F. G. Dunnington. *A Determination of e/m for an Electron by a New Deflection Method.* Phys. Rev. **43**, 404 416 (1933).

[53] B. Aubert et al. (BABAR Collaboration). *Study of time - dependent CP - violating asymmetries and flavor oscillations in neutral B decays at the Y(4S).* Phys. Rev. D **66**, 032003 (2002).

[54] A. Alavi - Harati et al. (KTeV Collaboration). *Observation of Direct CP Violation in $K_{S,L} \to \pi\pi$ Decays.* Phys. Rev. Lett. **83**, 22 27 (1999).

[55] P. F. Harrison. *Blind analysis* J. Phys. G: Nucl. Part. Phys. **28** 2679 2691 (2002).

[56] J. R. Klein and A. Roodman. *Blind Analysis in Nuclear and Particle Physics.* Annu. Rev. Nucl. Part. Sci. **55**, 141 63 (2005).

[57] M. V. Berry. *Quantal phase factors accompanying adiabatic changes.* Proc. R. Soc. Lon. A **392**, 45 - 47 (1984).

[58] M. R. Tarbutt, J. J. Hudson, B. E. Sauer and E. A. Hinds. *Prospects for measuring the electric dipole moment of the electron using electrically trapped polar molecules.* Faraday Discussions **142**, 37 - 56 (2009).

[59] B. Simon, *Holonomy, the Quantum Adiabatic Theorem, and Berry's Phase.* Phys. Rev. Lett. **51**, 2167 2170 (1983).

[60] Nikolay V Vitanov1 et al. *Laser - induced population transfer by adiabatic passage techniques.* Annu. Rev. Phys. Chem. **52**, 763 809 (2001).